UNIVERSITY OF CALIFORNIA SAN DIEGO

Metallic Nanoislands on Two-Dimensional Supports as Mechanical Biosensors

A Dissertation submitted in partial satisfaction of the requirements for the degree

Doctor of Philosophy

in

Chemical Engineering

by

Julian Ramirez

Committee in charge:

Professor Darren J. Lipomi, Chair
Professor Kenneth Loh
Professor Michael Tolley
Professor Joseph Wang
Professor Sheng Xu

2020

The Dissertation of Julian Ramirez is approved, and it is acceptable in quality and form for publication on microfilm and electronically:

Chair

University of California San Diego

2020

DEDICATION

Dedicado a mi familia, amigos, y sobre todo a Berta

EPIGRAPH

“Un hombre sin paciencia es una lámpara sin aceite”

-Andrés Segovia

"Puedes tener todas las virtudes del mundo en la piel, pero si no tienes ni suerte, ni gente que te ayude en el camino, no te sirven de nada esos dones"

-Zinedine Zidane

TABLE OF CONTENTS

LIST OF FIGURES

LIST OF TABLES

ACKNOWLEDGEMENTS

In the nine years that I've been at UC San Diego, I was fortunate enough to cross paths with people that shifted my life's trajectory towards a direction I couldn't have imagined had I thought I could achieve it all by myself. While I have learned and gained so much throughout the course of my undergraduate work and doctoral thesis, it is the people that surrounded me that I am the most grateful for.

Prof. Wang's Lab. My undergraduate experience laid the foundation for what would ultimately become my journey into the Ph.D. When looking for a lab to volunteer in, not knowing what I was looking for in life, Prof. Joseph Wang was generous enough to give me the opportunity to work in his group. I am incredibly grateful for his generosity and the three years I worked in his lab, as I learned what it really meant to be a scientist working there. I was also introduced to eye-opening technology, that has inspired me to keep pursuing projects that excite me as much as I progress further in my career. Working with Dr. Amay Bandodkar, Dr. Wenzhao Jia, and Dr. Gabriela Valdés-Ramírez were really rewarding experiences and made undergraduate work a pleasurable experience. Although I didn't have the pleasure of working with them in Prof. Wang's lab, I want to thank Prof. Jahir Orozco and Prof. Stefano Cinti for being great sources of motivation as I began thinking of pursuing a doctoral degree. They are members of my scientific family.

Undergrad. I was also incredibly fortunate to meet classmates that would become great lifelong friends during this time. Ashley Pourazary was the first friend I met at UC San Diego when I joined the Wang lab. It didn't take us long to get along, and she quickly became a person I could ask for help and advice in any aspect of my life. Ashley introduced me to Benjamin

Sarno, one of the closest friends I made at this university. To me, Ben is the definition of the word partner-in-crime, almost to a fault. I will always remember with laughter the time I was going to meet Prof. Lipomi for the first time and Ben ended up joining what was essentially my interview with my future Ph.D. advisor, as he assumed the meeting would be a general chat on research. Ben and I would end up pursuing our doctorates in the same department while being roommates for the first two years of our graduate school. Having him as a companion throughout my undergraduate and graduate school has truly been a blessing. While befriending Ashley and Ben we also met Aadil Hussaini, Mio Rudnicki, Kenneth Cante, and Ameer Bajwa people who I know I can always count on. I will always cherish the moments and laughs we all shared throughout the years. I am grateful for their friendship and their moral support.

Prof. Lipomi's Lab. During my time in the Lipomi Lab, I was fortunate to develop many professional relationships and friendships. Drs. Adam Printz, Suchol Savagatrup, Aliaksandr Zaretksi, and Timothy O'Connor were the first people to introduce me to the lab and helped me adjust as I began my doctoral work. They were always incredibly helpful, even with the most trivial questions I had. Dr. Brandon Marin was the best TA during my undergraduate years and being able to collaborate together in the lab was a rewarding experience. Dr. Samuel Root was an incredibly friendly lab mate whose easy-going personality was refreshing in lab. Dr. Cody Carpenter was a great presence in lab, especially because we shared similar views on research and academia in general. It was a pleasure going on coffee runs, and I look forward to playing soccer with him again one day. The one word I would use to describe Mohammad Alkhadra is brilliant, as I consider his discipline, work ethic, and overall character to be a source of inspiration. I consider him a great friend of mine and I look forward to the day you become a doctor (magna cum laude shouldn't be nothing to a boss, right coach?). I am grateful for sitting

next to Dr. Daniel Rodriquez for the majority of my Ph.D. The ability to talk about any number of topics throughout the day as we toiled away on our work was really helpful. The trip we took to Houston to work on my first publication is one of the highlights of this experience and it came at a seminal point in my doctoral work. He's been a great friend through all this, and I am deeply grateful for his scientific and moral support. To the undergraduates I had the pleasure of working with (Jasmine R., Andrew C., Liban J., Eden A., Armando U., Anne C., Madeleine R., and Patrick C.), I thank you all for doing the work that seldom gets acknowledged and I hope you learned as much from me as I learned from you.

I'd like to thank Andrew T. Kleinschmidt for putting up with my necessity to banter after lunch and for his help with Python for my last project. I look forward to the day he defends his thesis, though I won't have a clue what he's talking about. I admire Mickey Finn III for his multitasking abilities, and I thank him for keeping the Orion in good shape throughout my thesis. I'd like to thank Rory Sebastian Runser for performing his running impersonation of Timon from the Lion King and Sheldon from The Big Bang Theory for three years running, it's spot-on. All kidding aside, I wish him the best of luck on his doctoral work. I admire Alexander Chen's scientific curiosity and I wish him the best in his future endeavors. I thank Guillermo Esparza for his contributions to my last project and I aspire to be as candid as you one day. I'd like to thank my most recent office mates for putting up with me this last year and a half. Beril Polat has been a great addition to the lab and I thank her for adopting the work I began. I hope she's successful in taking it to new highs. Even though I've only known Laura Becerra for a short amount of time, she's shown to be a person with tons of resolve and dedication. She's been a great collaborator with Beril and I know they'll be really successful at whatever they set their mind to.

Steven and Rachel have been great office mates and they provided great conversation about life outside of work. I wish them the best of luck synthesizing all the conductive polymer they need.

I want to thank my advisor, Darren J. Lipomi, for everything he has done for me. Five years ago, he gave me the chance to pursue a doctoral degree when no one else gave me the chance, and I'll never forget that. The amount of knowledge I have acquired in these last five years blows everything else out of the water, and that is due to the dedication he has towards every single one of the members that comes into his lab. I am thankful for his patience when forming me into the scientist and engineer I am now, and I can only hope to continue to make him proud as I continue through my career. He has cultivated an amazing work environment that is unique, and I don't regret the decision to become a part of it.

NanoEngineering. I'd like to thank the following people who were not in my lab for their moral support throughout my thesis. Doris Ramirez, Rodolfo Mundaca, Miguel Ramirez, Cristian López, Víctor Ruiz, and Eva Vargas were great sources of support and I greatly enjoyed the daily lunch breaks we shared. Emil Kharsalev has been a great friend of mine in the department and the best defensive midfielder in the department, soccer on Sundays have been a blast so far and I look forward to dominating any team that dares to challenge us. Shout out goes to Daniel Davies for the stimulating conversations we had over our daily mental warm-ups, they were a real pick-me-up. I'd also like to thank Dana Jimenez for being one of the most helpful people in the department. I speak on the behalf of the student body when I say that your dedication to the department is definitely appreciated.

Friends & Family. I'd like to thank my childhood friends for all their moral support throughout the years. Michael Schenk is my oldest friend, so he gets first dibs. I only have vague

memory of when I first came to elementary school In the U.S. and he sat next to me and welcomed me into the new school. From that day until now, you have been a genuine friend, and for that I'm grateful. Christian Vivas was a great source of support during our first years at UC San Diego. He had already proved to be a great friend during middle school and high school, and those years further solidified that. I always look forward to the day the three of us can reunite for one more trip to Coachella. I met Roberto Ortiz in high school, and I'm glad I did. Since day one we've always been able to talk about our wide array of shared interests (watches, music, sartorial taste, etc.). Though we currently live in different cities, which makes it hard to reunite, I look forward to when can reunite next. We always pick up right where we left off last and that is a testament of our friendship.

I'd like to thank my entire family (both from the Ramirez and the Olvera side) for supporting me through my studies. I am truly fortunate to have you all as family and I am forever grateful for the support you've showed me throughout the years. To my brothers Omar and Braulio, thank you both for always providing unwavering support for my endeavors. I always enjoy our spontaneous debates on any topic (music, culture, soccer) and I'm fortunate to have the honor to call you guys my brothers. I can definitely say my life would be miserable if you guys weren't in it. To my cousin Arturo Hoyos, I enjoyed destressing from the weekday grind and bonding over playing soccer on Sundays at the water tower (back to back champs fam!). Even though you're a culé for life I'm glad to have you on my team, both on and off the field. Hanging out with you three this last year got me through the toughest part of my thesis, and for that I'm grateful.

A mi padre Julian, Susana, y por supuesto Lucas, les agradezco todo el apoyo que me han dado estos últimos años y por inculcarme el fruto de la perseverancia. Yendo a Tijuana para

verles siempre me ha traído una tranquilidad que me ha ayudado muchísimo para lograr lo que he logrado. Siempre agradeceré las risas que me han dado con su manera de ver la vida y el cariño que me han dado cuando lo he necesitado. Gracias por los sacrificios que han tomado para asegurar de que tuviera todo lo necesario para triunfar.

A mi madre Patricia, gracias por todo lo que has hecho por mi y mis hermanos hasta ahora. Siempre estaré agradecido por todos los sacrificios que hiciste para darnos la mejor oportunidad de salir adelante. Para mi has sido un ejemplo en como trabajar duro por lo que uno quiere, y como uno puede tener esperanza en los momentos difíciles. Nuestras platicas sobre la vida y como encontrar la felicidad son unas de las muchas cosas que tendré en mi corazón para siempre y estoy ilusionado por compartir contigo la felicidad que viene.

A mi comprometida Berta. Me acuerdo estar en el laboratorio un día en agosto, con la ilusión de pronto aplicar a posiciones de doctorado lejos de San Diego, en la búsqueda de una aventura que me diera la identidad que tanto buscaba. De repente apareciste y al verte escuché una voz en mi cabeza diciéndome “olvida tu idea de aventura, que estas en problemas.” En ese momento supe que la aventura que buscaba había llegado a mi sin tener que haberla buscado, y el resto es historia. Estos últimos cinco años han sido exactamente eso, una aventura llena de todo tipo de emociones e ilusiones. Te doy las gracias por no solo ser esa aventura, pero por también ser mi mayor apoyo. Siempre estaré agradecido por cada sacrificio que hiciste mientras me dedicaba a mi trabajo. También estoy agradecido por toda tu familia, que me recibió con los brazos abiertos al conocerme y me apoyaron igual que tu en mi logro. Estoy muy feliz de llamarles mi familia muy pronto. Sobre todo, quiero que sepas que estoy mas ilusionado que nunca porque, aunque acabe mi aventura que tanto busqué, la aventura que sigue será a tu lado. Este doctorado es igual tuyo que mío.

I also include the following acknowledgements below as required by the University of California, San Diego.

Chapter 1, in part, has been submitted for publication of the material as it may appear in ACS Omega. Julian Ramírez, Beril Polat, and Darren J. Lipomi. American Chemical Society, 2020. The dissertation author was the primary investigator and author of this paper.

Chapter 2 and Appendix A, in full, is a reprint of the material as it appears in ACS Nano, 2018, 12 (6), 3902-3911. Julian Ramírez, Daniel Rodriquez, Fang Qiao, Julian Warchall, Jasmine Rye, Eden Aklile, Andrew S.-C. Chiang, Brandon C. Marin, Patrick P. Mercier, CK Cheng, Katherine A. Hutcheson, Eileen H. Shinn, and Darren J. Lipomi. American Chemical Society, 2018. The dissertation author was the primary investigator and author of this paper.

Chapter 3 and Appendix B, in full, is a reprint of the material as it appears in ACS Applied Nano Materials, 2019, 2(4), 2222-2229. Julian Ramírez, Daniel Rodriquez, Armando D. Urbina, Anne Cardenas and Darren J. Lipomi. American Chemical Society, 2019. The dissertation author was the primary investigator and author of this paper.

Chapter 4 and Appendix C, in part, has been submitted for publication of the material as it may appear in Nanoscale, 2020. Julian Ramírez, Armando D. Urbina, Andrew T. Kleinschmidt, Mickey Finn III, Samuel J. Edmunds, Guillermo L. Esparza, and Darren J. Lipomi. Royal Society of Chemistry, 2020. The dissertation author was the primary investigator and author of this paper.

VITA

2015	Bachelor of Science in Chemical Engineering
	University of California, San Diego
2017	Master of Science in Chemical Engineering
	University of California San Diego
2020	Doctor of Philosophy in Chemical Engineering
	University of California San Diego

PUBLICATIONS

Ramírez, J.; Polat, B.; Lipomi, D. J. Metallic Nanoislands on Graphene for Biomechanical Sensing. *Submitted.* 2020.

Ramírez, J.; Urbina, A. D.; Kleinschmidt, A. T.; Finn III, M.; Edmunds, S. J.; Esparza, G. L.; Lipomi, D. J. Exploring the Limits of Sensitivity for Strain Gauges of Graphene and Hexagonal Boron Nitride Decorated with Metallic Nanoislands. *Submitted*. **2020**.

Ramírez, J.; Rodriquez, D.; Urbina, A. D.; Cardenas, A. M.; Lipomi, D. J. Combining High Sensitivity and Dynamic Range: Wearable Thin-Film Composite Strain Sensors of Graphene, Ultrathin Palladium, and PEDOT:PSS. *ACS Appl. Nano Mater.* **2019**.

Carpenter, C. W.; Tan, S. T. M.; Keef, C.; Skelil, K.; Malinao, M.; Rodriquez, D.; Alkhadra, M. A.; **Ramírez, J.**; Lipomi, D. J. Healable Thermoplastic for Kinesthetic Feedback in Wearable Haptic Devices. *Sensors Actuators, A Phys.* **2019**.

Sugiyama, F.; Kleinschmidt, A. T.; Kayser, L. V.; Rodriquez, D.; Finn, M.; Alkhadra, M. A.; Wan, J. M.-H.; **Ramírez, J.**; Chiang, A. S.-C.; Root, S. E.; Savagatrup, S.; Lipomi, D. J. Effects of Flexibility and Branching of Side Chains on the Mechanical Properties of Low-Bandgap Conjugated Polymers. *Polym. Chem.* **2018**.

Carpenter, C. W.; Dhong, C.; Root, N. B.; Rodriquez, D.; Abdo, E. E.; Skelil, K.; Alkhadra, M. A.; **Ramírez, J.**; Ramachandran, V. S.; Lipomi, D. J. Human Ability to Discriminate Surface Chemistry by Touch. *Mater. Horizons* **2018**, *5* (1), 70–77.

Rodriquez, D.; Kohl, J. G.; Morel, P.; Burrows, K.; Favaro, G.; Root, S. E.; **Ramírez, J.**; Alkhadra, M. A.; Carpenter, C. W.; Fei, Z.; Boufflet, P.; Heeney, M.; Lipomi, D. J. Measurement of Cohesion and Adhesion of Semiconducting Polymers by Scratch Testing: Effect of Side-Chain Length and Degree of Polymerization. *ACS Macro Lett.* **2018**.

Ramírez, J.; Rodriquez, D.; Qiao, F.; Warchall, J.; Rye, J.; Aklile, E.; S.-C. Chiang, A.; Marin, B. C.; Mercier, P. P.; Cheng, C. K.; Hutcheson, K. A.; Shinn, E. H.; Lipomi, D. J. Metallic Nanoislands on Graphene for Monitoring Swallowing Activity in Head and Neck Cancer Patients. *ACS Nano* **2018**, *12* (6), 5913–5922.

Dhong, C.; Edmunds, S. J.; **Ramírez, J.**; Kayser, L. V.; Chen, F.; Jokerst, J. V.; Lipomi, D. J. Optics-Free, Non-Contact Measurements of Fluids, Bubbles, and Particles in Microchannels Using Metallic Nano-Islands on Graphene. *Nano Lett.* **2018**, *18* (8), 5306–5311.

Kayser, L. V; Russell, M. D.; Rodriquez, D.; Abuhamdieh, S. N.; Dhong, C.; Khan, S.; Stein, A. N.; **Ramírez, J.**; Lipomi, D. J. RAFT Polymerization of an Intrinsically Stretchable Water-Soluble Block Copolymer Scaffold for PEDOT. *Chem. Mater.* **2018**, acs.chemmater.8b02040.

Marin, B. C.; **Ramírez, J.**; Root, S. E.; Aklile, E.; Lipomi, D. J. Metallic Nanoislands on Graphene: A Metamaterial for Chemical, Mechanical, Optical, and Biological Applications. *Nanoscale Horizons*. 2017, pp 311–318.

Jibril, L.; **Ramírez, J.**; Zaretski, A. V.; Lipomi, D. J. Single-Nanowire Strain Sensors Fabricated by Nanoskiving. *Sensors Actuators, A Phys.* **2017**, *263*, 702–706.

Bandodkar, A. J.; Jia, W.; **Ramírez, J.**; Wang, J. Biocompatible Enzymatic Roller Pens for Direct Writing of Biocatalytic Materials: "Do-It-Yourself" Electrochemical Biosensors. *Adv. Healthc. Mater.* **2015**, *4* (8), 1215–1224.

Bandodkar, A. J.; Mohan, V.; López, C. S.; **Ramírez, J.**; Wang, J. Self-Healing Inks for Autonomous Repair of Printable Electrochemical Devices. *Adv. Electron. Mater.* **2015**, *1* (12).

Bandodkar, A. J.; Jia, W.; Yardimci, C.; Wang, X.; **Ramirez, J.**; Wang, J. Tattoo-Based Noninvasive Glucose Monitoring: A Proof-of-Concept Study. *Anal. Chem.* **2015**, *87* (1), 394–398.

Berchmans, S.; Bandodkar, A. J.; Jia, W.; **Ramírez, J.**; Meng, Y. S.; Wang, J. An Epidermal Alkaline Rechargeable Ag–Zn Printable Tattoo Battery for Wearable Electronics. *J. Mater. Chem. A* **2014**, *2* (38), 15788–15795.

Kim, J.; Valdés-Ramírez, G.; Bandodkar, A. J.; Jia, W.; Martinez, A. G.; **Ramírez, J.**; Mercier, P.; Wang, J. Non-Invasive Mouthguard Biosensor for Continuous Salivary Monitoring of Metabolites. *Analyst* **2014**, *139* (7), 1632–1636.

Jia, W.; Wang, X.; Imani, S.; Bandodkar, A. J.; **Ramírez, J.**; Mercier, P. P.; Wang, J. Wearable Textile Biofuel Cells for Powering Electronics. *J. Mater. Chem. A* **2014**, *2* (43), 18184–18189.

Jia, W.; Bandodkar, A. J.; Valdés-Ramírez, G.; Windmiller, J. R.; Yang, Z.; **Ramírez, J.**; Chan, G.; Wang, J. Electrochemical Tattoo Biosensors for Real-Time Noninvasive Lactate Monitoring in Human Perspiration. *Anal. Chem.* **2013**, *85* (14), 6553–6560.

Bandodkar, A. J.; O'Mahony, A. M.; **Ramírez, J.**; Samek, I. a; Anderson, S. M.; Windmiller, J. R.; Wang, J. Solid-State Forensic Finger Sensor for Integrated Sampling and Detection of Gunshot Residue and Explosives: Towards "Lab-on-a-Finger". *Analyst* **2013**, *138* (18), 5288–5295.

Bandodkar, A. J.; Hung, V. W. S.; Jia, W.; Valdés-Ramírez, G.; Windmiller, J. R.; Martinez, A. G.; **Ramírez, J.**; Chan, G.; Kerman, K.; Wang, J. Tattoo-Based Potentiometric Ion-Selective Sensors for Epidermal PH Monitoring. *Analyst* **2013**, *138* (1), 123–128.

ABSTRACT OF THE DISSERTATION

Metallic Nanoislands on Two-Dimensional Supports as Mechanical Biosensors

by

Julian Ramirez

Doctor of Philosophy in Chemical Engineering

University of California San Diego, 2020

Professor Darren J. Lipomi, Chair

The development of resistive-based strain sensors comprising nanomaterials has become of interest for the past decade. Some of the interest in these types of sensors are due to their notable sensitivity, enabled by sensing mechanisms stemming from size confinement not seen in the bulk form of these materials. Apart from their sensitivity, these nanomaterials capable of detecting mechanical strain are also capable of being transferred to various hard, flexible and stretchable substrates. The ability to be used in compliant substrates overcomes the limitations seen in MEMS strain sensors, which can expand the array of their potential utility to applications such as wearable sensors. By developing an ultra-sensitive nanomaterial capable of detecting a wide strain range, it is possible to develop devices capable of monitoring human mechanical strain activity (from the cellular level to human motion). The ability to detect mechanical activity of biological phenomenon can be relevant in the medical field by developing deployable devices capable of giving clinicians reliable and actionable data. This thesis investigates the performance of a material comprising a subcontiguous film of noble metal supported by single-layer graphene (referred throughout as nanoislands, or Gr/M where M is the metal used), when used in devices for the detection of biomechanical deformations originating from human physiological activity. Chapter 1 introduces the Gr/M material and gives an overview of the various sensing modalities Gr/M possesses, while discussing recently developed sensing devices using this material. Chapter 2 and Appendix B present an iteration of a device, comprising Gr/Pd on a flexible substrate, for use as a wearable device to monitor swallowing activity in head and neck cancer patients. This study involves a 14-patient cohort study of head and neck cancer patients after radiation or surgery and the development of a machine learning algorithm to analyze the data given by the wearable strain sensor. Chapter 3 and Appendix C incorporates a layer of poly(3,4-ethylenedioxythiophene) polystyrene sulfonate (PEDOT:PSS) on top of the Gr/Pd film, which

increases the dynamic range of strain detectable by the composite film while retaining its sensitivity. Chapter 4 and Appendix D presents an empirical study comparing the material properties of Gr/M and composites comprising subcontiguous metal films on hexagonal boron nitride (hBN). The goal of this study is to help elucidate the possible sensing mechanism(s) responsible for the material's sensitivity to strains as low as 0.0001% (1 ppm) strain.

Chapter 1 Metallic Nanoislands on Graphene for Biomechanical Sensing

Abstract

This chapter describes a nanomaterial-based multimodal sensor for performing biomechanical measurements. The sensor consists of ultrathin metallic films on single-layer graphene. This composite material exhibits physical properties that neither material possesses alone. For example, the metal—deposited by evaporation at low (≤10 nm) nominal thicknesses—renders the film highly sensitive to mechanical and thermal stimuli, which can be detected using electrical (i.e., resistance) and optical (i.e., plasmonic) modalities. The electrical modality, in particular, is capable of resolving deformations as small as 0.0001% engineering strain, or 1 ppm. The electrical and optical responses of the composite films can be tailored by controlling the morphology of the metallic film. This morphology (granular or island-like when deposited onto the graphene) can be tuned using the conditions of deposition, the identity of the substrate beneath the graphene, or even the replacement of the graphene for hexagonal boron nitride (hBN). This material responds to forces produced by a range of physiological structures, from the contractions of heart muscle cells, to the beating of the heart through the skin, to stretching of the skin due to the expansion of the lungs and movement of limbs. Here, we provide an update on recent applications of this material in fields ranging from cardiovascular medicine (by measuring the contractions of 2D monolayers of cardiomyocytes), regenerative medicine (optical measurements of the forces produced by myoblasts), speech pathology and physical therapy (measuring swallowing function in head-and-neck cancer survivors), lab-on-a-chip devices (using deformation of sidewalls of microfluidic channels to count transiting objects), and sleep medicine (measuring pulse and respiration with a wearable, unobtrusive device). We also discuss the mechanisms by which these films detect strain.

1.1 Introduction

Mechanical forces are ubiquitous in human physiology, and thus the detection of biomechanical deformation is critical in research and the clinic. To address this need, many groups have developed strain gauges composed of a variety of materials and which operate by a range of mechanisms.[1–3] In particular, nanomaterial-based strain sensors have become a topic of interest due to their superior sensitivity when compared to conventional strain gauges based on bulk metals and alloys.[4,5] For example, bulk metallic traces can be used to sense tensile strain through detection of changes in electrical resistance due to constriction of the cross-sectional dimensions upon stretching. In contrast, the sensitivity of nanomaterial-based strain gauges arises from piezoresistive effects, in which mechanical deformation actually produces a change in the intrinsic resistivity of the material. Along with the high sensitivity of nanomaterial-enabled strain gauges, their amenability to various substrates (from rigid to elastomeric) expands the possible utility of these materials for in vitro and wearable applications.[6–8] Recent progress in the field of highly sensitive strain gauges has been driven by the development of thin metallic films containing fine cracks. In these systems, the response to mechanical strain is mediated by the propagation, opening, and closing of these cracks upon mechanical deformation.[9–11] The high sensitivity and mechanical stability offered by this class of materials have enabled the development of devices for applications ranging from wearable sensors to human-machine interfaces, exemplified in **Figure 1.1**. For example (**Figure 1.1a**), Kwon and coworkers developed a device capable of estimating energy expenditure by measuring the bending of the knee during walking and running.[12] In **Figure 1.1b**, a piezoresistive tactile sensor device was developed by Moon et. al, where the device contained two sensors made from metallized nanofibril networks.[13] Kim and collaborators recently paired a cracked metal film strain sensor

with a deep neural network to decode the complex motion of five finger motions in real-time (**Figure 1.1c**).[14]

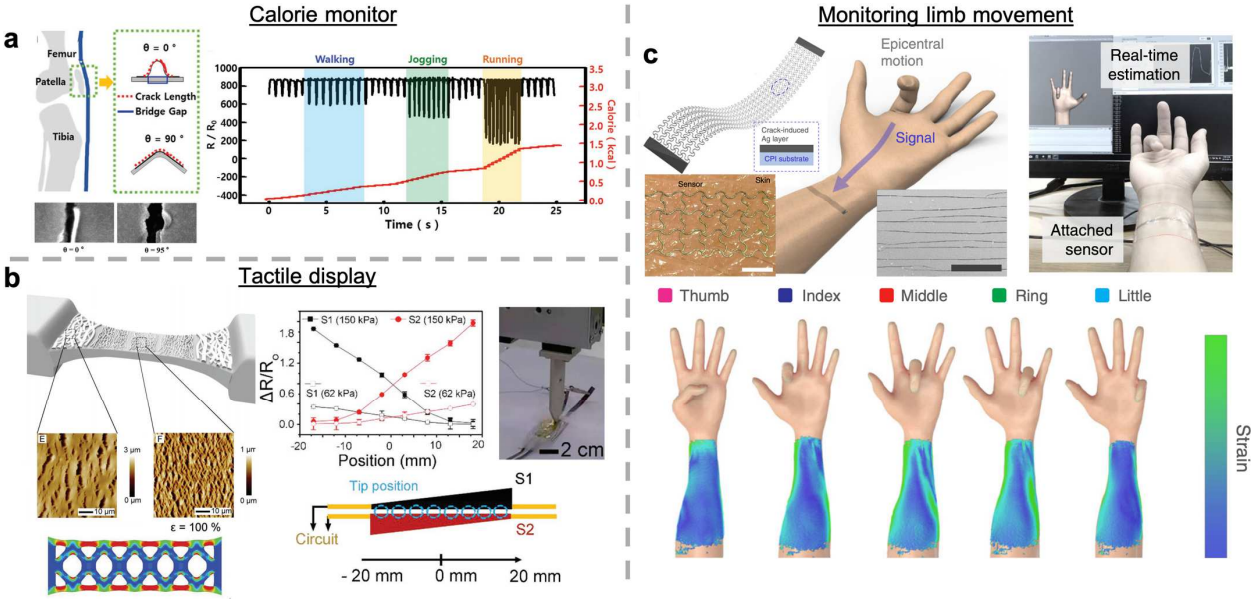

Figure 1.1. Overview of sensor devices comprising nanocracked metallic films. (a) Wearable sensors for measuring calorie expenditure during exercise. Reproduced (adapted) with permission from reference [12]. Copyright (2019) Wiley-VCH. (b) Tactile sensing device comprising metallized nanofibril networks for resistive strain sensing. Reproduced (adapted) with permission from reference [13]. Copyright (2018) Wiley-VCH. (c) Wearable sensor comprising a cracked metal network for the monitoring of finger movements, which were mapped to a virtual environment. Reproduced (adapted) with permission from reference [14]. Copyright (2020) Nature Publishing Group.

Over the last five years, our research group has been exploring a type of ultrasensitive strain gauge for measuring biomechanical deformation originating from both cells and physiological processes. These strain gauges are based on metallic nanoparticles supported by single-layer graphene.[15] When combined, these composite materials possess properties found in neither either bulk metal films nor single-layer graphene. For example, when used as piezoresistive strain gauges, a limit of detection of 0.0001% strain (resolution of 1 ppm or 1 microstrain) is possible. Applications for this material range from mechanical sensing of human biosignals (e.g. swallowing activity, respiration, and cardiac pulse rate) and elastohydrodynamic

deformation in microfluidic channels, to optical monitoring of mechanical contractions of myoblast cells. In our experiments, we have used gold, silver, and palladium as the metallic film on graphene. Gold is unreactive and biocompatible, thus a useful metal to use when detecting mechanical activity piezoresistively. Palladium and silver, however, are cytotoxic but possess ultra-sensitive piezoresistive and "piezoplasmonic" sensitivity, respectively. By exploiting the biocompatibility of graphene and the use of encapsulation, these materials are capable of measuring biomechanical activity with a better response than gold while mitigating possible toxicity. A summary of the biomechanical forces measured using this material is shown in **Figure 1.2**.

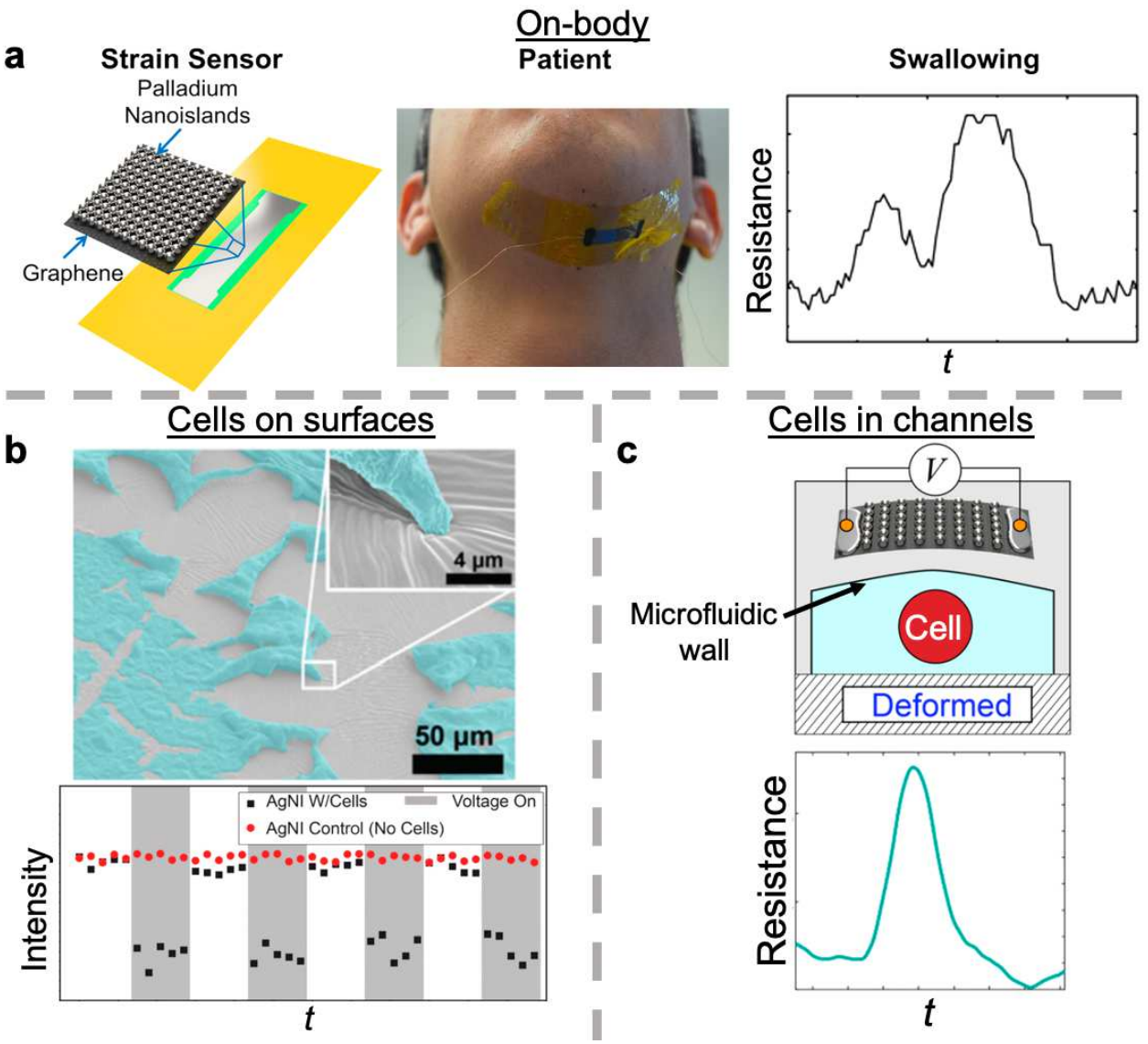

Figure 1.2. Overview of metallic films on 2D substrates for biomechanical measurements. (a) Wearable sensors for the detection of mechanical biosignals on the skin. Reproduced (adapted) with permission from reference11. Copyright (2018) American Chemical Society. (b) Optical detection of the contractions in musculoskeletal cells using changes in intensity of the surface-enhanced Raman scattering signal of a monolayer of reporter molecules adsorbed to the metallic films. Reproduced (adapted) with permission from ref.12 Copyright (2017) Royal Society of Chemistry. (c) Enumeration of particles and cells flowing through microfluidic channels. Reproduced (adapted) with permission from reference13. Copyright (2018) American Chemical Society.

1.2 Initial findings: metallic films on single-layer graphene

In a serendipitous discovery during an unrelated project,[19] we found that it was possible to control the morphologies of the metallic films evaporated onto graphene by changing the

identity of the substrate supporting the graphene.[20–24] This difference in morphologies depended on the lattice mismatch between the evaporated metal and the graphene, along with differences in surface energy between the substrate supporting the graphene and the evaporated metal.[24] As an example of this apparent partial "wetting transparency,"[25] changing the underlying substrate from copper to silver caused films of evaporated gold and silver to transition from a subcontiguous film with a high prevalence of isthmus-like connections between grains, to a film of discrete nanoislands. With the ability to generate granular metallic films with very small spacings between adjacent particles, we reasoned that the composite films might behave as ultrasensitive strain gauges. Some of these strain gauges—as described by others—operate by modulation of the tunneling current between adjacent particles by mechanical strain.[26] While we would later determine that tunneling is not likely to play a dominant role in the strain response in the films that we were making, we nevertheless found that the change in electrical resistance of strain gauges made from these films exhibited extraordinarily high sensitivity and resolution.

The sensitivity of a strain gauge is quantified by the gauge factor, defined as the ratio of the normalized change in electrical resistance to the applied strain. Commercial strain gauges that detect strain through geometrical changes in the metallic film have gauge factors of ~2 for modest strains (~ 1-5%).[27,28] For comparison, we found that graphene/metal films had gauge factors over 10 in the ultralow strain regime (~ 0.001%), and could thus enable detection of minute biomechanical signals.[24] For example, gold islands on single-layer graphene were capable of detecting the contractions of rat cardiomyocytes by a change in the electrical resistance of the gold-graphene composite.[24] The sensor had a response time of 0.8 ± 0.2 ms. Critically, since gold is a noble metal that is not cytotoxic, we saw no adverse effects in the cells due to exposure to the metal. In the first on-body application, it was possible to measure the

pulse waveform of the radial artery on the surface of the wrist of a human subject. For palladium on graphene, the smallest detectable strain—i.e., resolution starting in an unstrained state—was, at the time, measured to be 0.001% (later found to be an order of magnitude lower than this). Moreover, the sensors exhibited a useful degree of dynamic range. When placed on a silicone elastomer, these sensors could be cyclically stretched up to 9% (the largest strain tested before the supporting substrate ruptured) while returning to the baseline resistance at mechanical equilibrium.[24]

1.2.1 Near-zero temperature coefficient of resistance.

One disadvantage of strain sensors that use a change in electrical resistance as the output is that the resistance tends to have an unwanted dependence on temperature. In conventional strain gauges, the problem of non-zero temperature coefficient of resistance (TCR) of pure metals is circumvented by the use of alloys such as constantan, an alloy of copper and nickel, whose resistance exhibits only a small dependence on temperature. We were thus interested in how we might tune the composition of the metal-graphene composite films to achieve a similar effect.[29] In their pristine form, single-layer graphene has a negative TCR while bulk metal has a positive TCR and hence the rates of change in resistance with respect to increasing temperature have the opposite sign.[30,31] By measuring the TCR of the films as a function of the nominal thickness of metal, we could generate films that were insensitive to temperature but not to strain.[32,33] Analysis of the morphology of the metallic film as a function of increasing nominal thickness (and surface coverage) led to a simple model to correlate the thermoresistive behavior of the composite material as a function of surface coverage. The model shows that the TCR of the composite becomes increasingly positive with increasing coverage of the metal. Thus, the resistance of the composite material can be tuned to have a near-zero dependence on temperature because the

positive TCR of the metal counterbalances the negative TCR of graphene. As a proof of concept, wearable sensors with near-zero TCR were fabricated to demonstrate the stability of the electrical signal when detecting the pulse waveform on the wrist, while suppressing variations in surface temperature produced by simulated sunlight.

1.3 Developments in Wearable Applications

1.3.1 Wearable sensor for monitoring swallowing activity.

We then sought to develop devices capable of exploiting the exceptional piezoresistance of this material in real-world scenarios. The monitoring of swallowing activity is of particular interest in populations who suffer from head and neck cancer. While this condition is curable with radiation therapy, up to 40% of patients develop radiation-associated fibrosis of the swallowing muscles and subsequent dysphagia, which severely reduces swallowing function.[34–37] Dysphagia is devastating to the quality of life, with some patients needing to be fed percutaneously, by tube.[38] The current gold-standard method to monitor the onset of dysphagia is videofluoroscopy, where an X-ray video of a patient is obtained during the swallowing of a barium-containing paste. While videofluoroscopy provides a complete assessment of a patient's swallowing function, this exam requires visits to the clinic. Because of the episodic nature of this exam, fibrosis is often not detected until it is too late, and thus there is a need for continuous monitoring, possibly using an at-home device.

To address this need, we developed a flexible device comprising strain-sensitive palladium nanoislands on single-layer graphene to be placed on the skin underneath the chin to detect mechanical deformation due to swallowing (**Figure 1.3a**). To complement the strain measurements, surface electromyography (sEMG) measurements of the muscle activity were obtained using conventional metallic electrodes. The utility of our device was tested by

measuring the swallowing activity in a cohort of 14 head and neck cancer patients, 7 of whom exhibited signs of dysphagia, and 7 of whom had normal swallowing function. Assisted by a machine-learning algorithm, measurements of strain could be used to detect differences in swallowing activity based on the consistency of the swallowed food (i.e., water, yogurt, cracker). "The algorithm was also able to distinguish dysphagic from non-dysphagic swallowing (**Figure 1.3b** and **1.3c**). The algorithm was trained by asking the user or patient to swallow the same bolus several times (red curves) to develop the classifier models for each signal (blue curve). After developing the models, a new swallowing signal (green curve) was then placed into a category. The accuracy of the classifier models was tested through cross-validation techniques. An efficient classification model based on the L1-distance of the per-class average (i.e., the distance between the model signal and the new signal at every time point) was found to be the most accurate model. In a separate experiment (not shown), visual comparison of the strain data with sEMG data made it possible to distinguish swallowing from motion artifacts (e.g., head turning and coughing)." Comparison of the strain data with sEMG data made it possible to distinguish swallowing from motion artifacts (e.g., head turning and coughing). For one patient, the data from the sensor were compared to the results obtained from a videofluoroscopy examination. It was thus possible to attribute changes in electrical resistance with time to different phases in the swallowing process.[39–41] This study thus represents an example of a nanomaterial-enabled device in a patient cohort study, and further establishes wearable devices as potential complements to clinically accepted practices in patient care.

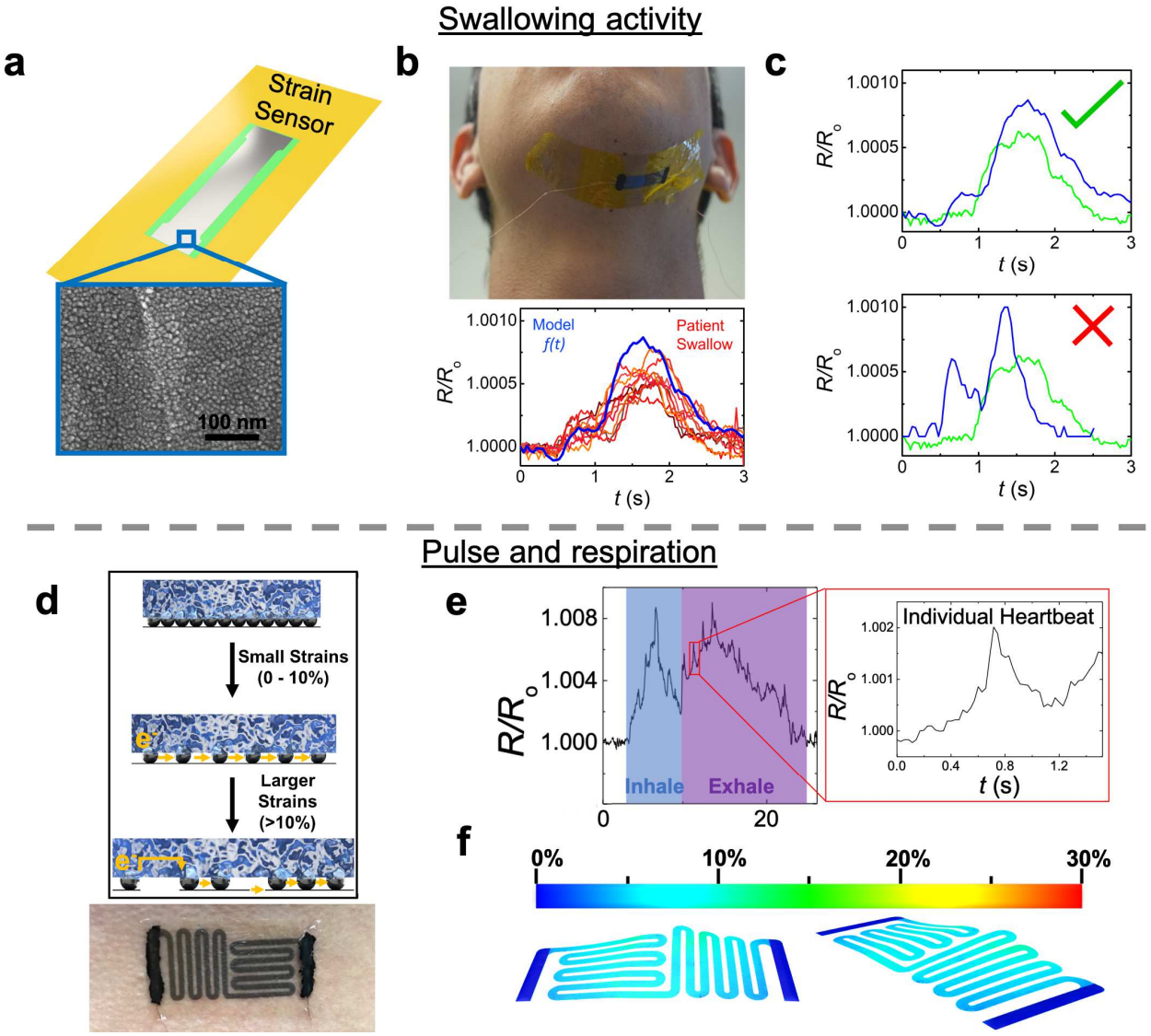

Figure 1.3. Piezoresistive biomechanical sensing with wearable devices comprising graphene/metal composites. Graphene/palladium (Gr/Pd) devices have been used for (a) the piezoresistive detection of swallowing activity in head and neck cancer patients, for the monitoring of the onset of swallowing dysfunction due to radiation. The swallowing data acquired by the sensor was used to (b) develop machine learning algorithms designed to (c) distinguish swallows for the same food type between a healthy human (bottom plot, blue) and a dysphagic patient (top plot). Reproduced (adapted) with permission from reference11. Copyright (2018) American Chemical Society. By combining d) Gr/Pd with PEDOT:PSS, stretchable devices could be used for the simultaneous measurement of human pulse pressure and respiration waveforms by placing the device on the torso of a human participant (e). (f) The deformation in the structure was modeled using finite element analysis. Reproduced (adapted) with permission from reference37. Copyright (2019) American Chemical Society.

1.3.2 Wearable sensor for monitoring interpolated biomechanical signals.

A constant challenge in the development of strain gauges is the ability to combine sensitivity and dynamic range. This challenge is especially salient for strain gauges based on graphene, which fractures at only a few percent strain, whereas skin is significantly more stretchable (i.e., up to 50%). To develop stretchable sensors capable of withstanding greater strains while retaining piezoresistive sensitivity, we combined the graphene/metal film with a formulation of plasticized PEDOT:PSS, by depositing the conductive polymer directly on top of the nanomaterial composite, seen in **Figure 1.3d**.[42,43] The role of the conductive polymer was to introduce an alternative pathway for electrical conduction upon cracking of the graphene film. Hence, the electrons would travel through the graphene/metal film at low strains (~ 0.001%), as it is the path of lowest electrical resistance, but would travel through a contiguous path comprising all three materials at larger strains. We found that this strategy was largely successful, as our "structured composite" consisting of graphene/metal/PEDOT:PSS provided high resolution at low strains (strains of 0.001% produced a change in resistance well above the noise) while the highly plasticized nature of the PEDOT:PSS formulation allowed for the retention of conductivity up to 86% strain. In order to develop a wearable device using this material, we encapsulated the graphene/metal film between two PDMS layers. The encapsulation of the film between elastomeric layers resulted in a reduction of the piezoresistive sensitivity but an increase in the working range of the material. The piezoresistive response of the material demonstrated some hysteresis at strains above 10% but was able to withstand up to 250 cycles (the maximum number of cycles tested). Moreover, experiments in which the material was cyclically stretched suggested that the conductive pathways involving the graphene reformed upon return to mechanical equilibrium (i.e. physical contact after the material fractures). The utility of the

improved material was demonstrated by attaching a stretchable device, comprising graphene/metal/PEDOT:PSS, on the torso of a human subject simulating sleep and detecting interpolated signals stemming from respiration and pulse, seen in **Figure 1.3e** and **Figure 1.3f**. This proof-of-concept experiment—using the diagnosis of sleep apnea using polysomnography as inspiration—highlights the potential of wearable nanomaterial devices to reduce the complexity and costs of devices for distributed healthcare.[44–46]

1.4 Assaying cellular biomechanics

1.4.1 Optical measurements of myocyte activity.

All cells produce mechanical forces; in the case of myocytes, mechanical activity is central to their function. Assays of mechanical activity of cells in vitro has thus stimulated the development of sensing platforms.[47,48] In particular, platforms amenable to high-throughput measurements are desirable to determine the effect of environmental stresses (e.g., in evaluating the cardiotoxicity of drug candidates).[49] Sensors based on metallic nanoparticles supported by graphene have significant potential for use in this field, as they are both piezoresistive and plasmonically active. In particular, the morphology of island-like metallic films on graphene enables the detection of mechanical activity using an optical modality.[50,51] These composite materials are thus in principle capable of detecting mechanical activity through more than one sensing modality. For example, by reacting a film of silver nanoislands on graphene with a solution of benzene thiol, it was possible to use the resulting self-assembled monolayer of benzene thiolate as a reporter. That is, we reasoned that the small gaps between adjacent nanoislands would produce an intense electric field, which would substantially amplify the characteristic surface-enhanced Raman scattering (SERS) spectrum of benzene thiolate.[52] A schematic diagram illustrating our hypothesis can be seen in **Figure 1.4a**. Given that the spacing

between nanoislands could be modulated by strain, we hypothesized that the composite film would be an effective optical strain sensor. That is, since the intensity of the electric field between adjected nanoparticles is nonlinearly dependent on the spacing between particles, and the SERS intensity is nonlinearly dependent on the intensity of the electric field, the compounded nonlinear effects would lead to exceptional sensitivity to strain. Moreover, the electrical conductivity of the graphene would permit electrical stimulation of or measurement from structures (i.e., cells) with which it was in contact.

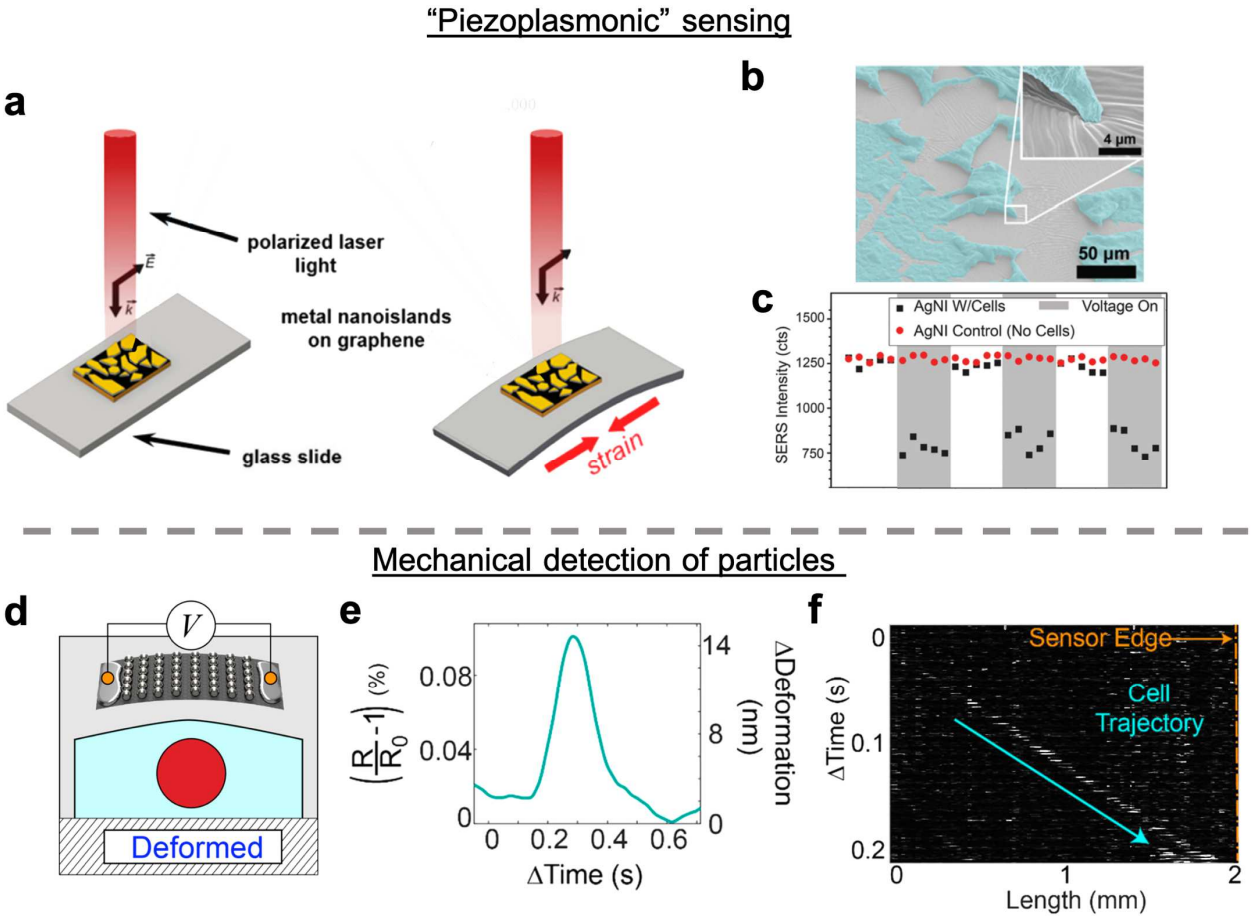

Figure 1.4. Use of metal-graphene composite strain gauges for cellular biomechanics. a) Metallic nanoislands supported by graphene undergo a change in plasmonic resonance under strain. This change is reflected in a modulation of the surface-enhanced Raman scattering (SERS) intensity of a self-assembled monolayer of benzene thiolate bonded to the metal. (b) A device comprising a film of graphene/silver is used to stimulate contractions of musculoskeletal cells (C2C12 myoblast) electrically, while (c) attenuation of the SERS signal corresponds to the contractions. Reproduced (adapted) with permission from ref.[17] Copyright (2017) Royal Society of Chemistry. (d) Particles passing through microfluidic channels produce small deflections of the sidewalls of the channels that can be detected by bending of sensors embedded in the sidewalls. (e) A change in resistance caused by the channel deformation due to flowing human mesenchymal stem cells is monitored. (f) The image shows cells as they pass through the fluidic channel. Reproduced (adapted) with permission from reference[18]. Copyright (2018) American Chemical Society.

To investigate the possibility of simultaneous electrical stimulation with optical detection, we deposited a 2D monolayer of myoblast cells on a nanoisland/graphene film (**Figure 1.4b**). Although silver has the potential for cytotoxicity, the biocompatibility of the composite was assured by placing the silver on the bottom, with the cells adhered to the graphene. We

applied a pulsed voltage to the cells through the graphene/silver film, which caused them to contract and thus pull the silver nanoislands apart around the periphery of the cells. Increased separation between individual silver nanoislands led to a decrease in plasmonic coupling and hence to a decreased signal, as seen in **Figure 1.4c**. This plasmonic behavior was not observed in electrically pulsed silver nanoisland substrates without cells. This control experiment confirmed that the effect was not based on an inherent piezoelectric effect in metal nanoislands that causes them to contract. The complimentary modalities of electrical stimulation and optical sensing for cellular media could be useful in monitoring actuatable cells, especially in a future high-throughput format.

1.4.2 Detecting particles and cells in microfluidic channels by deflection of the sidewalls.

The high sensitivity of the graphene-metal composite films led us to investigate whether it would be possible to perform mechanically based analyses of nonadherent cells as they flowed through microfluidic channels. That is, our calculations suggested that the transit of particles through microchannels in elastomeric slabs would deform the sidewalls, even if the diameter of the particle was smaller than the diameter of the channel. At the very least, the technique could permit the enumeration of flowing objects. Such a capability is useful for blood-based detection of cells of different sizes and possibly also for rapid screening of mechanical properties, e.g., circulating tumor cells. With this motivation, we embedded our graphene-based sensors in the sidewalls of microfluidic channels (**Figure 1.4d**).[53] In our initial experiments, our device was able to detect the transit of bubbles, solid particles, and individual human-derived mesenchymal stem cells through a microfluidic channel by measuring the changes in electrical resistance that corresponded to the deflection of the sidewalls of the channel (**Figure 1.4e and 1.4f**). We note that lag due to the viscoelasticity of the channel walls could decrease the maximum frequency

with which transiting particles could be counted. While at present, the device is only able to differentiate objects based on size, it might be possible to use theory to reconstruct the stiffness of the particles (or cells) as they transit based on the time-dependent deformation profile of the sidewalls.

1.4.5 Understanding the mechanism of strain detection.

We then sought to understand the piezoresistive mechanism(s) of these films. Our analysis was confounded at the outset by the fact that both metallic films and graphene exhibit a change in resistance under strain when used alone. For bulk metallic foils, the change in resistance is geometrical in origin, while piezoresistance in disconnected metallic particles has been shown to arise from tunneling in systems where the spacing between particles is especially small.[50,54] Theoretical calculations on the electronic properties of single-layer graphene indicate that the increase in electrical resistance due to mechanical strain is due to scattering effects, stemming from random strain fluctuations in the film.[55,56] Other simulation-based studies have also observed an opening in the band gap of graphene due to the break in sublattice symmetry when C-C bonds are elongated.[57,58] Such calculations, however, assume pristine, single-crystal, and defect-free graphene, which is difficult to obtain on scales larger than hundreds of microns.[55,59] Throughout our studies with graphene/metal films, we determined that the piezoresistive effect of single-layer graphene is amplified through the addition of metal adatoms on its surface.

The central feature of our investigation was the replacement of graphene with hexagonal boron nitride (hBN). A visual schematic of our approach can be seen in **Figure 1.5**. While graphene is a conductor and exhibits piezoresistance, hBN is an insulator and has no electrical response to strain.[60,61] Thus, it would be possible to separate contributions of metal to the

piezoresistance of the composite film from those of the graphene.[62] We first compared the morphologies of these metal films on single-layer graphene and hexagonal boron nitride to gain insight into the influence of the 2D substrates on the morphology of the metal film being deposited. Through analysis of scanning and transmission electron microscopy (SEM and TEM) images, we were able to calculate the fractional coverage, extent of connectivity, and percolation thresholds as a function of nominal thickness of the metallic film on each of the 2D substrates.

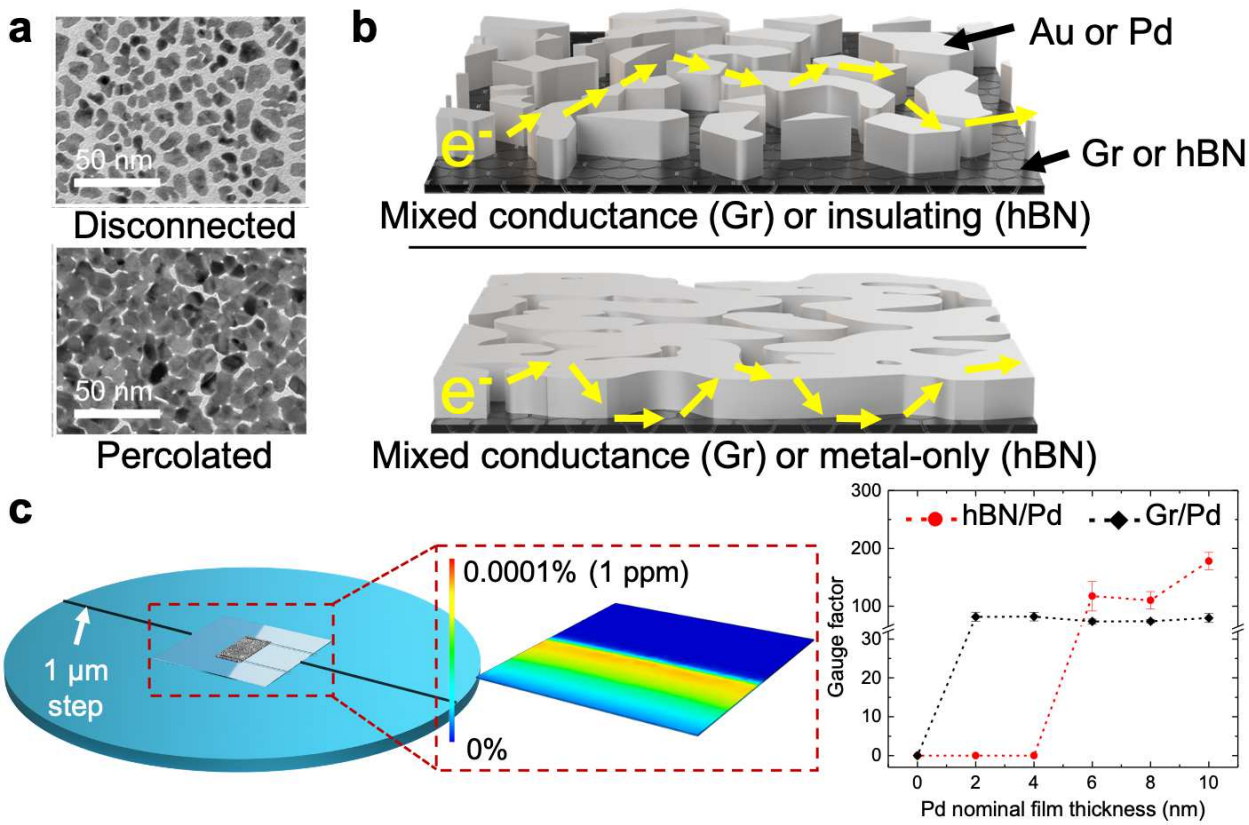

Figure 1.5. Elucidating mechanism of piezoresistive strain detection. (a) Transmission electron micrographs of disconnected and percolated films of palladium on single-layer graphene, with nominal thicknesses of 2 nm and 8 nm, respectively. (b) Schematic diagrams showing the electron path across the films of graphene/metal and hBN/metal films. (c) Cantilever apparatus for measuring the piezoresistive response of graphene/metal and hBN/metal films as they undergo step bending strains of 1 ppm (0.0001%). The magnitude of sensitivity is determined by calculating the gauge factor of the films at a chosen bending strain. Reproduced from reference[56].

After analyzing the morphology of the granular metallic films (**Figure 1.5a**), we measured the piezoresistive response of these films at ultralow strains for the different 2D substrates (**Figure 1.5c**). For the regime of small strains tested, our experiments demonstrated that films on hBN in which the metal was unpercolated produced open circuits and thus did not produce a response to strain. Thus, physical continuity of the metallic film on hBN was required. Films comprising metal on graphene, on the other hand, were capable of resolving strains ≥ 0.0001%, regardless of the degree of percolation in the metal film. While films in which the metal was unpercolated were both conductive and piezoresistive, we were not able to resolve these small mechanical strains with pristine single-layer graphene. While the reason for this transition is not clear, several changes in the graphene occur at the initial stages of metallization and could possibly affect the evolution in piezoresistive response with strain. As palladium is deposited onto graphene, the metal adatoms form palladium carbide bonds and etch pristine graphene, which degrades the conductivity of the film in the process.[42,63,64] Additionally, the effect of mechanical deformation on the electronic structure of graphene is not clear. However, the addition of metal islands to graphene could produce an inhomogeneous strain field in the composite film, whose effect on the electromechanical behavior would be difficult to predict.

After characterizing the strain response, we measured the response of the films to temperature, as piezoresistive films that operate under a tunneling mechanism should exhibit a negative TCR. Instead, we observed a positive TCR in all the metal films on hBN (at least those that exhibited any conductivity), while the TCR of graphene/metal systems depended heavily on the degree of percolation of the metal. The reason for this dependence is that metals have a positive TCR and graphene has a negative one, and the TCR of the composite is thus determined by the relative amounts of the two materials. The results of these experiments point to the

absence of tunneling as a dominant mechanism of either conductivity or piezoresistance in the films.

Our work in elucidating the mechanism of piezoresitance, however, does not explicitly consider electronic interactions between the metal and the 2D substrates or quantization of charge transport in the metallic films due to their extremely small thicknesses. Even with these recent advances, further work must be done to gain better insight into the fundamentals behind the optical, electronic, and mechanical properties that result from interactions between metal films and 2D substrates. Computational methods using first-principle mechanical and electronic simulations of graphene/metal composites could provide deeper fundamental understanding as to which physiochemical interactions enable the sensing capabilities of these materials.

1.5 Conclusions

This chapter summarized our recent work in developing strain gauges based on metallic nanoislands supported by single-layer graphene. The sensitivity and resolution of these devices have permitted us to explore applications in biomechanics and mechanobiology. We have shown that these films, which exhibit piezoresistive effects to strains as low as 0.0001%, are among the most sensitive and highest-resolution strain gauges reported. Moreover, in concert with stretchable conductive polymers, layered composites can be shown to combine high dynamic range to the already high sensitivity and resolution. In the context of biomechanical sensors, we have shown that machine learning has the potential to transform the raw output into actionable data. Our work to elucidate the mechanism of piezoresistance in the composite materials suggests that neither the graphene nor the metal alone is responsible for the performance of the devices, and that both materials are required. We believe that the development of a deeper

understanding of the operational mechanisms of these interesting composite materials will lead to the development of more effective nanomaterial-enabled strain gauges in the future.

Acknowledgements

This work was supported by the National Institutes of Health Director's New Innovator Award, Grant 1DP2EB022358. J.R. acknowledges support provided by the National Science Foundation Graduate Research Fellowship Program under Grant DGE-1144086, and the UC President's Dissertation Year Fellowship. Additional support was provided by the Center for Wearable Sensors in the Jacobs School of Engineering at the University of California, San Diego, and member companies Qualcomm, Sabic, Cubic, Dexcom, Corning, Honda, Samsung, and Sony. This work was performed in part at the San Diego Nanotechnology Infrastructure (SDNI), a member of the National Nanotechnology Coordinated Infrastructure, which is supported by the National Science Foundation (Grant ECCS-1542148). Thanks to Rory Runser for helpful comments.

Chapter 1, in full, is a reprint of material that has been submitted for publication. Julian Ramírez, Beril Polat, and Darren J. Lipomi. The dissertation author was the primary investigator and author of this paper.

References

(1) Ji, X.; Yang, L.; Wei, Z.; Wang, L.; Xi, J.; Li, Z. A Monolithically Integrated Platform for High Throughput Cell Characterization and Drug Screening. In *TRANSDUCERS 2009 - 2009 International Solid-State Sensors, Actuators and Microsystems Conference*; IEEE, 2009; pp 1786–1789.

(2) Pruitt, B. L. MEMS for Cell Mechanobiology. In *2014 IEEE International Electron Devices Meeting*; IEEE, 2014; pp 31.3.1-31.3.4.

(3) Trung, T. Q.; Lee, N. E. Flexible and Stretchable Physical Sensor Integrated Platforms for Wearable Human-Activity Monitoringand Personal Healthcare. *Adv. Mater.* **2016**, *28* (22),

4338–4372.

(4) Jibril, L.; Ramírez, J.; Zaretski, A. V.; Lipomi, D. J. Single-Nanowire Strain Sensors Fabricated by Nanoskiving. *Sensors Actuators, A Phys.* **2017**, *263*, 702–706.

(5) Meiksin, Z. H.; Hudzinski, R. A. A Theoretical Study of the Effect of Elastic Strain on the Electrical Resistance of Thin Metal Films. *J. Appl. Phys.* **1967**, *38* (11), 4490–4494.

(6) Wang, Y.; Wang, L.; Yang, T.; Li, X.; Zang, X.; Zhu, M.; Wang, K.; Wu, D.; Zhu, H. Wearable and Highly Sensitive Graphene Strain Sensors for Human Motion Monitoring. *Adv. Funct. Mater.* **2014**, *24* (29), 4666–4670.

(7) Yamada, T.; Hayamizu, Y.; Yamamoto, Y.; Yomogida, Y.; Izadi-Najafabadi, A.; Futaba, D. N.; Hata, K. A Stretchable Carbon Nanotube Strain Sensor for Human-Motion Detection. *Nat. Nanotechnol.* **2011**, *6* (5), 296–301.

(8) Liu, Q.; Chen, J.; Li, Y.; Shi, G. High-Performance Strain Sensors with Fish-Scale-Like Graphene-Sensing Layers for Full-Range Detection of Human Motions. *ACS Nano* **2016**, *10* (8), 7901–7906.

(9) Kang, D.; Pikhitsa, P. V.; Choi, Y. W.; Lee, C.; Shin, S. S.; Piao, L.; Park, B.; Suh, K. Y.; Kim, T. Il; Choi, M. Ultrasensitive Mechanical Crack-Based Sensor Inspired by the Spider Sensory System. *Nature* **2014**, *516* (7530), 222–226.

(10) Yang, T.; Li, X.; Jiang, X.; Lin, S.; Lao, J.; Shi, J.; Zhen, Z.; Li, Z.; Zhu, H. Structural Engineering of Gold Thin Films with Channel Cracks for Ultrasensitive Strain Sensing. *Mater. Horizons* **2016**, *3* (3), 248–255.

(11) Park, B.; Kim, J.; Kang, D.; Jeong, C.; Kim, K. S.; Kim, J. U.; Yoo, P. J.; Kim, T. Dramatically Enhanced Mechanosensitivity and Signal-to-Noise Ratio of Nanoscale Crack-Based Sensors: Effect of Crack Depth. *Adv. Mater.* **2016**, *28* (37), 8130–8137.

(12) Kwon, K. Y.; Shin, Y. J.; Shin, J. H.; Jeong, C.; Jung, Y. H.; Park, B.; Kim, T. Stretchable, Patch□Type Calorie□Expenditure Measurement Device Based on Pop□Up Shaped Nanoscale Crack□Based Sensor. *Adv. Healthc. Mater.* **2019**, *8* (19), 1801593.

(13) Moon, S.; Park, H. K.; Song, J. H.; Cho, S.; Kim, J. C.; Kim, J.; Hwang, H.; Kim, H. S.; Jeong, U. Metal Deposition on a Self-Generated Microfibril Network to Fabricate Stretchable Tactile Sensors Providing Analog Position Information. *Adv. Mater.* **2018**, *30* (32), 1801408.

(14) Kim, K. K.; Ha, I. H.; Kim, M.; Choi, J.; Won, P.; Jo, S.; Ko, S. H. A Deep-Learned Skin Sensor Decoding the Epicentral Human Motions. *Nat. Commun.* **2020**, *11* (1), 1–8.

(15) Marin, B. C.; Ramírez, J.; Root, S. E.; Aklile, E.; Lipomi, D. J. Metallic Nanoislands on Graphene: A Metamaterial for Chemical, Mechanical, Optical, and Biological

Applications. *Nanoscale Horiz.* **2017**, *2* (6), 311–318.

(16) Ramírez, J.; Rodriquez, D.; Qiao, F.; Warchall, J.; Rye, J.; Aklile, E.; S.-C. Chiang, A.; Marin, B. C.; Mercier, P. P.; Cheng, C. K.; Hutcheson, K. A.; Shinn, E. H.; Lipomi, D. J. Metallic Nanoislands on Graphene for Monitoring Swallowing Activity in Head and Neck Cancer Patients. *ACS Nano* **2018**, *12* (6), 5913–5922.

(17) Marin, B. C.; Liu, J.; Aklile, E.; Urbina, A. D.; Chiang, A. S. C.; Lawrence, N.; Chen, S.; Lipomi, D. J. SERS-Enhanced Piezoplasmonic Graphene Composite for Biological and Structural Strain Mapping. *Nanoscale* **2017**, *9* (3), 1292–1298.

(18) Dhong, C.; Edmunds, S. J.; Ramirez, J.; Kayser, L.; Chen, F.; Jokerst, J.; Lipomi, D. J. Optics-Free, Non-Contact Measurements of Fluids, Bubbles and Particles in Microchannels Using Metallic Nanoislands on Graphene. *Nano Lett.* **2018**, acs.nanolett.8b02292.

(19) Zaretski, A. V.; Marin, B. C.; Moetazedi, H.; Dill, T. J.; Jibril, L.; Kong, C.; Tao, A. R.; Lipomi, D. J. Using the Thickness of Graphene to Template Lateral Subnanometer Gaps between Gold Nanostructures. *Nano Lett.* **2015**, *15* (1), 635–640.

(20) Rafiee, J.; Mi, X.; Gullapalli, H.; Thomas, A. V.; Yavari, F.; Shi, Y.; Ajayan, P. M.; Koratkar, N. A. Wetting Transparency of Graphene. *Nat. Mater.* **2012**, *11* (3), 217–222.

(21) Li, H.; Zeng, X. C. Wetting and Interfacial Properties of Water Nanodroplets in Contact with Graphene and Monolayer Boron-Nitride Sheets. *ACS Nano* **2012**, *6* (3), 2401–2409.

(22) Yazyev, O. V.; Pasquarello, A. Metal Adatoms on Graphene and Hexagonal Boron Nitride: Towards Rational Design of Self-Assembly Templates. *Phys. Rev. B - Condens. Matter Mater. Phys.* **2010**, *82* (4), 1–5.

(23) Pandey, P. A.; Bell, G. R.; Rourke, J. P.; Sanchez, A. M.; Elkin, M. D.; Hickey, B. J.; Wilson, N. R. Physical Vapor Deposition of Metal Nanoparticles on Chemically Modifi Ed Graphene : Observations on Metal – Graphene Interactions. **2011**, No. 22, 3202–3210.

(24) Zaretski, A. V; Root, S. E.; Savchenko, A.; Molokanova, E.; Printz, A. D.; Jibril, L.; Arya, G.; Mercola, M.; Lipomi, D. J. Metallic Nanoislands on Graphene as Highly Sensitive Transducers of Mechanical, Biological, and Optical Signals. *Nano Lett.* **2016**, *16* (2), 1375–1380.

(25) Kong, W.; Li, H.; Qiao, K.; Kim, Y.; Lee, K.; Nie, Y.; Lee, D.; Osadchy, T.; Molnar, R. J.; Gaskill, D. K.; Myers-Ward, R. L.; Daniels, K. M.; Zhang, Y.; Sundram, S.; Yu, Y.; hoon Bae, S.; Rajan, S.; Shao-Horn, Y.; Cho, K.; Ougazzaden, A.; Grossman, J. C.; Kim, J. Polarity Governs Atomic Interaction through Two-Dimensional Materials. *Nat. Mater.* **2018**, *17* (11), 999–1004.

(26) Segev-Bar, M.; Haick, H. Flexible Sensors Based on Nanoparticles. *ACS Nano* **2013**, *7*

(10), 8366–8378.

(27) Li, T.; Huang, Z.; Suo, Z.; Lacour, S. P.; Wagner, S. Stretchability of Thin Metal Films on Elastomer Substrates. *Appl. Phys. Lett.* **2004**, *85* (16), 3435–3437.

(28) Kim, Y. S.; Lu, J.; Shih, B.; Gharibans, A.; Zou, Z.; Matsuno, K.; Aguilera, R.; Han, Y.; Meek, A.; Xiao, J.; Tolley, M. T.; Coleman, T. P. Scalable Manufacturing of Solderable and Stretchable Physiologic Sensing Systems. *Adv. Mater.* **2017**, *29* (39), 1–11.

(29) Marin, B. C.; Root, S. E.; Urbina, A. D.; Aklile, E.; Miller, R.; Zaretski, A. V.; Lipomi, D. J. Graphene–Metal Composite Sensors with Near-Zero Temperature Coefficient of Resistance. *ACS Omega* **2017**, *2* (2), 626–630.

(30) Shao, Q.; Liu, G.; Teweldebrhan, D.; Balandin, A. A. High-Temperature Quenching of Electrical Resistance in Graphene Interconnects. *Appl. Phys. Lett.* **2008**, *92* (20), 202108.

(31) Mott, N. F. The Resistance and Thermoelectric Properties of the Transition Metals. *Proc. R. Soc. London. Ser. A - Math. Phys. Sci.* **1936**, *156* (888), 368–382.

(32) Lee, S.-E.; Sohn, Y.; Chu, K.; Kim, D.; Park, S.-H.; Bae, M.; Kim, D.; Kim, Y.; Han, I.; Kim, H.-J. Suppression of Negative Temperature Coefficient of Resistance of Multiwalled Nanotube/Silicone Rubber Composite through Segregated Conductive Network and Its Application to Laser-Printing Fusing Element. *Org. Electron.* **2016**, *37*, 371–378.

(33) Sun, P.; Zhu, M.; Wang, K.; Zhong, M.; Wei, J.; Wu, D.; Zhu, H. Small Temperature Coefficient of Resistivity of Graphene/Graphene Oxide Hybrid Membranes. *ACS Appl. Mater. Interfaces* **2013**, *5* (19), 9563–9571.

(34) Rosenthal, D. I.; Lewin, J. S.; Eisbruch, A. Prevention and Treatment of Dysphagia and Aspiration after Chemoradiation for Head and Neck Cancer. *J. Clin. Oncol.* **2006**, *24* (17), 2636–2643.

(35) Bleier, B. S.; Levine, M. S.; Mick, R.; Rubesin, S. E.; Sack, S. Z.; McKinney, K.; Mirza, N. Dysphagia after Chemoradiation: Analysis by Modified Barium Swallow. *Ann. Otol. Rhinol. Laryngol.* **2007**, *116* (11), 837–841.

(36) Society, A. C. *Cancer Facts & Figures 2017*; Atlanta, GA, 2017.

(37) Ridner, S. H.; Dietrich, M. S.; Niermann, K.; Cmelak, A.; Mannion, K.; Murphy, B. A Prospective Study of the Lymphedema and Fibrosis Continuum in Patients with Head and Neck Cancer. *Lymphat. Res. Biol.* **2016**, *14* (4), 198–205.

(38) Høxbroe Michaelsen, S.; Grønhøj, C.; Høxbroe Michaelsen, J.; Friborg, J.; von Buchwald, C. Quality of Life in Survivors of Oropharyngeal Cancer: A Systematic Review and Meta-Analysis of 1366 Patients. *Eur. J. Cancer* **2017**, *78*, 91–102.

(39) Logemann, J. A. Role of the Modified Barium Swallow in Management of Patients with Dysphagia. *Otolaryngol. - Head Neck Surg.* **1997**, *116* (3), 335–338.

(40) Martin-Harris, B.; Logemann, J. a; McMahon, S.; Schleicher, M.; Sandidge, J. Clinical Utility of the Modified Barium Swallow. *Dysphagia* **2000**, *15* (3), 136–141.

(41) Hutcheson, K. A.; Barrow, M. P.; Barringer, D. A.; Knott, J. K.; Lin, H. Y.; Weber, R. S.; Fuller, C. D.; Lai, S. Y.; Alvarez, C. P.; Raut, J.; Lazarus, C. L.; May, A.; Patterson, J.; Roe, J. W. G.; Starmer, H. M.; Lewin, J. S. Dynamic Imaging Grade of Swallowing Toxicity (DIGEST): Scale Development and Validation. *Cancer* **2016**, 1–9.

(42) Ramírez, J.; Rodriquez, D.; Urbina, A. D.; Cardenas, A. M.; Lipomi, D. J. Combining High Sensitivity and Dynamic Range: Wearable Thin-Film Composite Strain Sensors of Graphene, Ultrathin Palladium, and PEDOT:PSS. *ACS Appl. Nano Mater.* **2019**.

(43) Oh, J. Y.; Kim, S.; Baik, H.-K.; Jeong, U. Conducting Polymer Dough for Deformable Electronics. *Adv. Mater.* **2016**, *28* (22), 4455–4461.

(44) Mendonça, F.; Mostafa, S. S.; Ravelo-García, A. G.; Morgado-Dias, F.; Penzel, T. Devices for Home Detection of Obstructive Sleep Apnea: A Review. *Sleep Med. Rev.* **2018**, *41*, 149–160.

(45) Oliver, N.; Flores-Mangas, F. HealthGear: Automatic Sleep Apnea Detection and Monitoring with a Mobile Phone. *J. Commun.* **2007**, *2* (2), 1–9.

(46) Franklin, K. A.; Lindberg, E. Obstructive Sleep Apnea Is a Common Disorder in the Population-A Review on the Epidemiology of Sleep Apnea. *J. Thorac. Dis.* **2015**, *7* (8), 1311–1322.

(47) Rajagopalan, J.; Saif, M. T. A. MEMS Sensors and Microsystems for Cell Mechanobiology. *J. Micromechanics Microengineering* **2011**, *21* (5), 054002.

(48) Kim, D.-H.; Wong, P. K.; Park, J.; Levchenko, A.; Sun, Y. Microengineered Platforms for Cell Mechanobiology. *Annu. Rev. Biomed. Eng.* **2009**, *11* (1), 203–233.

(49) del Álamo, J. C.; Lemons, D.; Serrano, R.; Savchenko, A.; Cerignoli, F.; Bodmer, R.; Mercola, M. High Throughput Physiological Screening of IPSC-Derived Cardiomyocytes for Drug Development. *Biochim. Biophys. Acta - Mol. Cell Res.* **2016**.

(50) Scholl, J. A.; García-Etxarri, A.; Koh, A. L.; Dionne, J. A. Observation of Quantum Tunneling between Two Plasmonic Nanoparticles. *Nano Lett.* **2013**, *13* (2), 564–569.

(51) Xiang, Q.; Zhu, X.; Chen, Y.; Duan, H. Surface Enhanced Raman Scattering of Gold Nanoparticles Supported on Copper Foil with Graphene as a Nanometer Gap. *Nanotechnology* **2016**, *27* (7), 75201.

(52) Marin, B. C.; Liu, J.; Aklile, E.; Urbina, A. D.; Chiang, A. S. C.; Lawrence, N.; Chen, S.; Lipomi, D. J. SERS-Enhanced Piezoplasmonic Graphene Composite for Biological and Structural Strain Mapping. *Nanoscale* **2017**, *9* (3), 1292–1298.

(53) Dhong, C.; Edmunds, S. J.; Ramírez, J.; Kayser, L. V.; Chen, F.; Jokerst, J. V.; Lipomi, D. J. Optics-Free, Non-Contact Measurements of Fluids, Bubbles, and Particles in Microchannels Using Metallic Nano-Islands on Graphene. *Nano Lett.* **2018**, *18* (8), 5306–5311.

(54) Tanner, J. L.; Mousadakos, D.; Giannakopoulos, K.; Skotadis, E.; Tsoukalas, D. High Strain Sensitivity Controlled by the Surface Density of Platinum Nanoparticles. *Nanotechnology* **2012**, *23* (28).

(55) Huang, M.; Pascal, T. A.; Kim, H.; Goddard, W. A.; Greer, J. R. Electronic−Mechanical Coupling in Graphene from in Situ Nanoindentation Experiments and Multiscale Atomistic Simulations. *Nano Lett.* **2011**, *11* (3), 1241–1246.

(56) Couto, N. J. G.; Costanzo, D.; Engels, S.; Ki, D.-K.; Watanabe, K.; Taniguchi, T.; Stampfer, C.; Guinea, F.; Morpurgo, A. F. Random Strain Fluctuations as Dominant Disorder Source for High-Quality On-Substrate Graphene Devices. *Phys. Rev. X* **2014**, *4* (4), 041019.

(57) Hicks, J.; Tejeda, A.; Taleb-Ibrahimi, A.; Nevius, M. S.; Wang, F.; Shepperd, K.; Palmer, J.; Bertran, F.; Le Fèvre, P.; Kunc, J.; De Heer, W. A.; Berger, C.; Conrad, E. H. A Wide-Bandgap Metal–Semiconductor–Metal Nanostructure Made Entirely from Graphene. *Nat. Phys.* **2013**, *9* (1), 49–54.

(58) Skomski, R.; Dowben, P. A.; Sky Driver, M.; Kelber, J. A. Sublattice-Induced Symmetry Breaking and Band-Gap Formation in Graphene. *Mater. Horiz.* **2014**, *1* (6), 563–571.

(59) Pereira, V. M.; Castro Neto, A. H.; Peres, N. M. R. Tight-Binding Approach to Uniaxial Strain in Graphene. *Phys. Rev. B - Condens. Matter Mater. Phys.* **2009**, *80* (4), 1–8.

(60) Watanabe, K.; Taniguchi, T.; Kanda, H. Direct-Bandgap Properties and Evidence for Ultraviolet Lasing of Hexagonal Boron Nitride Single Crystal. *Nat. Mater.* **2004**, *3* (6), 404–409.

(61) Giovannetti, G.; Khomyakov, P. A.; Brocks, G.; Kelly, P. J.; Van Den Brink, J. Substrate-Induced Band Gap in Graphene on Hexagonal Boron Nitride: Ab Initio Density Functional Calculations. *Phys. Rev. B - Condens. Matter Mater. Phys.* **2007**, *76* (7), 2–5.

(62) Ramírez, J.; Urbina, A. D.; Kleinschmidt, A. T.; Finn, M.; Edmunds, S. J.; Esparza, G. L.; Lipomi, D. J. Exploring the Limits of Sensitivity for Strain Gauges of Graphene and Hexagonal Boron Nitride Decorated with Metallic Nanoislands. *Nanoscale* **2020**, 12 (20), 11209-11221.

(63) Ramasse, Q. M.; Zan, R.; Bangert, U.; Boukhvalov, D. W.; Son, Y. W.; Novoselov, K. S. Direct Experimental Evidence of Metal-Mediated Etching of Suspended Graphene. *ACS Nano* **2012**, *6* (5), 4063–4071.

(64) Gong, C.; McDonnell, S.; Qin, X.; Azcatl, A.; Dong, H.; Chabal, Y. J.; Cho, K.; Wallace, R. M. Realistic Metal-Graphene Contact Structures. *ACS Nano* **2014**, *8* (1), 642–649.

Chapter 2 Metallic Nanoislands on Graphene for Monitoring Swallowing Activity in Head and Neck Cancer Patients

Abstract

There is a need to monitor patients with cancer of the head and neck post-radiation therapy, as diminished swallowing activity can result in disuse atrophy and fibrosis of the swallowing muscles. We describe a flexible strain sensor comprising palladium nanoislands on single-layer graphene. These piezoresistive sensors were tested on 14 disease-free head and neck cancer patients with various levels of swallowing function: from non-dysphagic to severely dysphagic. The patch-like devices detected differences in (1) the consistencies of food boluses when swallowed and (2) dysphagic and non-dysphagic swallows. When surface electromyography (sEMG) is obtained simultaneously with strain data, it is also possible to differentiate swallowing *vs.* non-swallowing events. The plots of resistance *vs.* time are correlated to specific events recorded by video X-ray fluoroscopy. Finally, we developed a machine learning algorithm to automate the identification of bolus type being swallowed by a healthy subject (86.4%. accuracy). The algorithm was also able to discriminate between swallows of the same bolus from either the healthy subject or a dysphagic patient (94.7% accuracy). Taken together, these results may lead to noninvasive and home-based systems for monitoring of swallowing function and improved quality of life.

2.1. Introduction

Multifunctional, wearable devices for health monitoring have the potential to reduce medical costs, increase patient comfort, and improve patient outcomes. These devices can do so by replacing or complementing invasive, painful, and costly diagnostic procedures with patch-like devices that can be applied by the patient at home. The consequences of sporadic,

incomplete monitoring are especially severe following radiation therapy in patients with cancer of the head and neck.[1,2] In these patients, diminished swallowing activity and treatment effects lead to fibrosis, edema, disuse atrophy, and reduced function in swallowing. We describe a highly sensitive and flexible patch-like strain sensor that comprises palladium nanoislands on single-layer graphene. When attached to the skin in the submental region, below the chin, this piezoresistive sensor produces signals that indicate flexion of the swallowing muscles and passing of a bolus from the mouth to the esophagus. The objective of this work was to examine the hypothesis that these signals, combined with simultaneous readings from surface electromyography (sEMG), will allow detection of swallowing dysfunction, differentiation between swallowing and non-swallowing events, and differentiation of boluses of different consistencies by a machine learning algorithm.

In 2017, 30,360 new cases of laryngeal or pharyngeal cancers, and 6,710 deaths from those diseases, are expected in the U.S.[3–6] Radiation therapy is commonly used for treatment, which can cause edema and eventually fibrosis (stiffening) of the swallowing musculature in up to 47% of head and neck cancer patients. These side effects of radiation contribute to the permanent development of moderate-to-severe dysphagia (abnormal or difficult swallowing) in up to 39% of head and neck cancer patients.[7] The ability to monitor the development of fibrotic tissue and deteriorating muscle function in cancer patients post-treatment is imperative to monitor the development of dysphagia. The most common method to monitor the development and severity of dysphagia is videofluoroscopy, commonly referred to as a modified barium swallow (MBS) exam. An MBS exam involves the video recording under continuous X-ray of a patient swallowing boluses of different consistencies.[8,9] Using videofluoroscopy, clinicians can grade the severity of dysphagia of a patient on a numerical scale (a grade of 1 corresponds to

mild dysphagia and a grade of 4 corresponds to profound dysphagia).[10] While the MBS provides clinically useful data, it requires that the boluses be impregnated with barium to be detected and exposes patients to radiation. Furthermore, equipment for videofluoroscopy is expensive, requires trained personnel, and is only available in the clinic. Due to the limited access of speech pathologists trained in the treatment of head and neck cancer and the cost of gold-standard modified barium swallow (MBS) tests, radiation-induced dysphagia is often diagnosed after there is little hope of restoring normal function.[11–15]

Techniques to measure physiological signals from the surface of the skin offer the potential for non-invasive monitoring without the need for visits to the clinic. sEMG monitors the electrical activity of a muscle when it is contracting. There are ongoing attempts to use sEMG to identify and monitor dysphagia in head and neck cancer patients, but such techniques have not been widely adopted because standard protocols were only recently established, and because of the limitations of the type of data available to sEMG.[16–20] When used alone, however, sEMG is limited in the types of activities it can monitor. For example, sEMG monitors the electrical activity of muscles when they are actively contracting, but the relaxation of the swallowing muscles cannot be monitored. Continuous sensing of mechanical strain on the surface of the skin can in principle follow the contractions and relaxations of the submental muscles as a bolus is taken into the mouth and swallowed. Wearable sensors that use a piezoresistive mechanism are ubiquitous.[21] Researchers have used devices that consist of carbon-based nanomaterials,[22–25] as well as composite materials,[26–28] to detect subtle motions of the throat, such as respiration, speaking, and swallowing. Multiple groups have used various sensing modalities to assay swallowing activity.[29–34] However, these studies did not monitor the mechanical activity of muscle groups in the submental region, which are particularly susceptible

to fibrosis following radiation therapy.[13] Here, we present a wearable piezoresistive sensor that comprises palladium nanoislands on single-layer graphene and its use in measuring the swallowing activity of head-and-neck cancer patients after radiotherapy. These palladium-graphene composites are used to detect swallowing activity by measuring the strain of the skin when a patient swallows a bolus. These sensors, when combined with conventional sEMG and a machine learning algorithm, can be used to monitor patients in real time, while differentiating between signals that arise due to coughing, turning of the head, and swallowing of boluses of different consistencies.

2.2. Results and Discussion

2.2.1. Characterization of strain sensor device

As shown in **Figure 2.1a**, palladium nanoislands were deposited onto single-layer graphene by thermal evaporation using a stainless-steel mask to pattern the nanoislands into a dog-bone shape. The composite film was then transferred to a polyimide tape by a water transfer method (described in the Experimental Methods). The nanoscale morphology of 8 nm palladium on single-layer graphene supported by copper foil is depicted in **Figure 2.1b**. Morphologically, this palladium film consists of small islands that are separated by nanoscale gaps. The electrical resistance of the film is mediated in part by tunneling across these gaps, and thus it is highly sensitive to mechanical strains.[35,36] Demonstrated in **Figure 2.1c**, the composite film had a piezoresistive response to a 0.02% bending strain, and was able to reversibly detect this strain up to 115 cyclic bends (see **Figure A.0.1**). A strain of 0.02% was chosen as it was similar to the strain the skin in the submental region experiences during swallowing. This approximation was determined by observing the change in the normalized resistance (R/R_0) to the bending strain and comparing it to the change in normalized resistance when a head and neck cancer patient (**Figure**

2.3) swallowed 10 mL of water as a reference. The similar piezoresistive response to a patient swallowing a bolus and the bending strain confirm that our sensor on polyimide tape can easily detect strains that are physiologically relevant during swallowing.

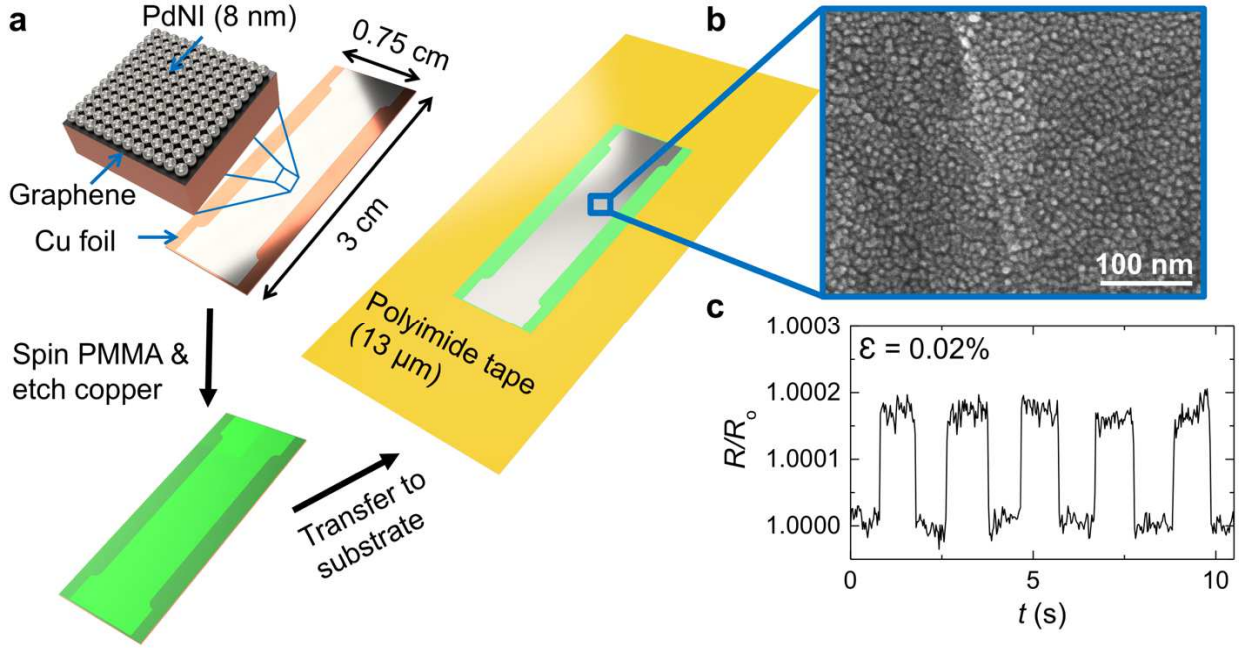

Figure 2.1. Schematic diagram depicting the fabrication of the palladium nanoisland (PdNI) strain sensor. (a) Fabrication process of the palladium nanoisland sensor on polyimide tape. (b) Scanning electron microscope (SEM) image of the morphology of palladium nanoislands on a single layer of graphene. (c) Piezoresistive response of the composite film under a 0.02% strain that was determined by a cantilever strain experiment.

2.2.2. On-body experiments: healthy subject

On-body experiments were performed with a healthy subject (age 24, male) prior to placing the sensors on head and neck cancer patients. As shown in **Figure 2.2**, swallows of different boluses resulted in distinctive and identifiable strain signals from the sensor. The signal from the patient performing a dry swallow can be seen in **Figure 2.2a**. The plot depicts multiple small events of tensile and compressive strain, followed by a brief instance of relaxation, and finished with a large tensile strain at the end of the swallow. On average, it took the healthy

subject approximately 4 s to complete one dry swallow. The signal from the patient swallowing 10 mL of water is shown in **Figure 2.2b**. The swallowing signals contain two distinct tensile strain events, with the second being greater in magnitude than the first. The total time to complete the swallow of 10 mL of water was approximately 2 s. For the strain signal from the subject swallowing a tablespoon (15 mL) of yogurt, seen in **Figure 2.2c**, the first incidence of tensile strain was almost twice as large and narrower as the second tensile strain, and the swallow was performed in approximately 2 s. The signal from the subject swallowing a bite of a cracker, seen in **Figure 2.2d**, was similar to the signal from swallowing a tablespoon of yogurt, as the first instance in tensile strain was larger and narrower than the subsequent tensile strains. However, the tensile strains arising from the subject swallowing a cracker are greater in magnitude when compared to the signals of the subject swallowing a tablespoon of yogurt. Additionally, the time to perform the swallow for a cracker was longer than the time to swallow the yogurt bolus, and the signal from the subject swallowing a cracker contains a minor strain event, around 1 s, not observed in the signal from swallowing the yogurt. Further investigation demonstrated that the piezoresistive response of the device to swallowing events is not affected by an elevated heart rate in the human subject but can possibly be affected by the placement of the sensor with respect to the submental region (see **Figure A.0.2** and **Figure A.0.3**). The differences in the strain signals, namely strain magnitude and duration, allow for the identification of each bolus by visual observation.

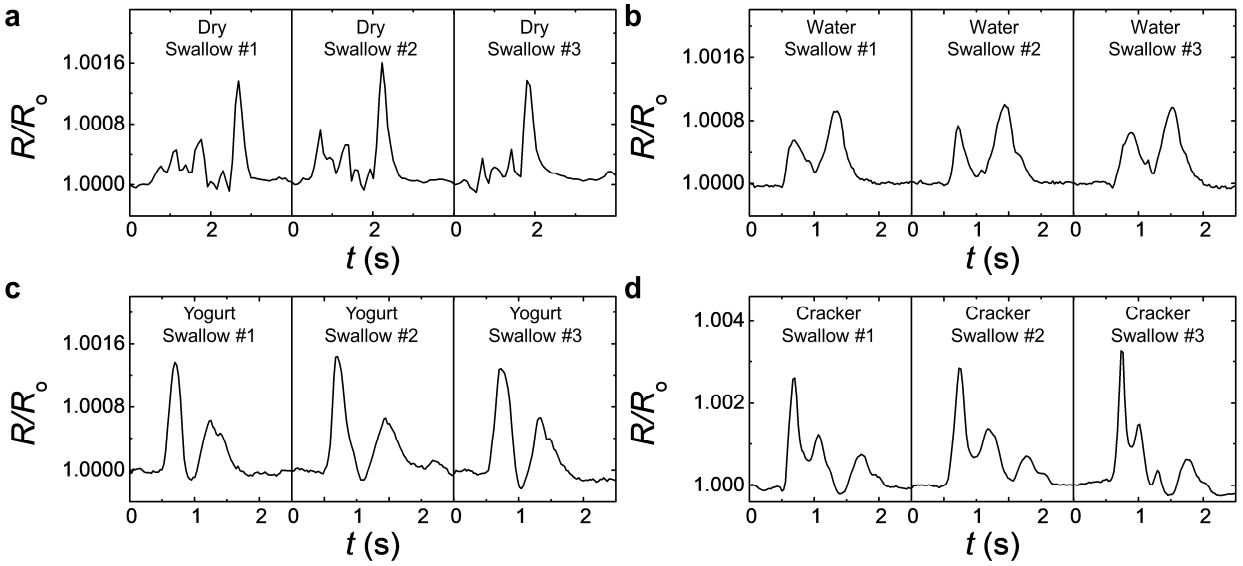

Figure 2.2. Signals (normalized resistance vs. time) generated by the strain sensor as a healthy subject swallowed different boluses. (a) Signal of healthy subject performing a dry swallow. (b) Signal of the healthy subject swallowing a thin sip of water (~10 mL). (c) Signal of the healthy subject swallowing a tablespoon of yogurt (15 mL). (d) Signal of the healthy subject swallowing a masticated bite from a cracker.

2.2.3. On-body experiments: head and neck cancer patients

We further evaluated the practical utility of the palladium nanoisland sensors by detecting the flexion on the submental region of head and neck cancer patients with varying degrees of dysphagia during the ingestion of different bolus types. The placement of the strain sensor on the submental region of a patient, and the signals from dysphagic and non-dysphagic patients as they swallowed 10 mL of water are shown in **Figure 2.3a** and **Figure 2.3b** respectively. The degree of normalcy in the swallowing function of a non-dysphagic patient can be evaluated by comparing the piezoresistive signal produced by the swallows of these patients to that produced by a healthy subject (age 24, male) (**Figure 2.2**). Two distinct increases in the resistance were observed due to the tensile strain experienced by the skin during a normal swallow. The first tensile strain event (**Figure 2.3b**, i) may reflect the contraction of submental muscles during the

first phase of swallowing. Subsequently, the skin relaxed slightly, which caused the resistance to decrease before the second increase in resistance (**Figure 2.3b**, ii). This second peak is greater in magnitude than the first and may represent the larger strain experienced by the skin as the muscles contract to elevate the larynx and hyoid bone during the pharyngeal transit phase of the swallow. Completion of the swallowing process took approximately 2 s, as detected by the strain sensor, which was consistent with the completion time for the normal healthy subject. However, in dysphagic patients, the sensor detected strain signal patterns that were substantially different from the two distinct increases in normalized resistance detected for the non-dysphagic patients. The sensor detected more than two events of tensile and compressive strain for dysphagic patients, that may reflect successive muscle contractions as they swallowed, as shown in the left column of **Figure 2.3b**. Additionally, the total time for the dysphagic patient to swallow the bolus was significantly longer than for the non-dysphagic patient. We observed a correlation between the amount of struggle and the severity of dysphagia a patient had when swallowing the bolus by examining the number of instances of tensile and compressive strain and the total time it took each patient to complete the swallow. Struggle manifests as unusually long times to swallow and many undulating features in the plots of resistance. We hypothesize that these characteristics may suggest the development of dysphagia.

The time and effort required to swallow a bolus also depends on bolus consistency, once chewed and mixed with saliva. The signals from the strain sensor for three different boluses (water, yogurt, and a cracker) from a single non-dysphagic patient are shown in **Figure 2.3c**. The signals arising from swallowing these boluses were differentiated by (1) the magnitudes of tensile and compressive strains and (2) the timing and duration of these strain events. For the most fluid boluses (water and yogurt), the general shape of the curve and the time needed to

complete the swallow were similar, but not identical. Small differences in the mechanical properties of these boluses (liquid *vs.* viscoelastic liquid) affected the magnitudes of the strains measured at the surface of the skin. The consistency of the chewed cracker, however, was that of a thick paste, and the time needed by the patient to swallow the bolus increased. These observations of the properties of the boluses (*i.e.*, liquid *vs.* paste) *versus* the time required to perform the swallow agree with previous studies for normal swallowing.[37]

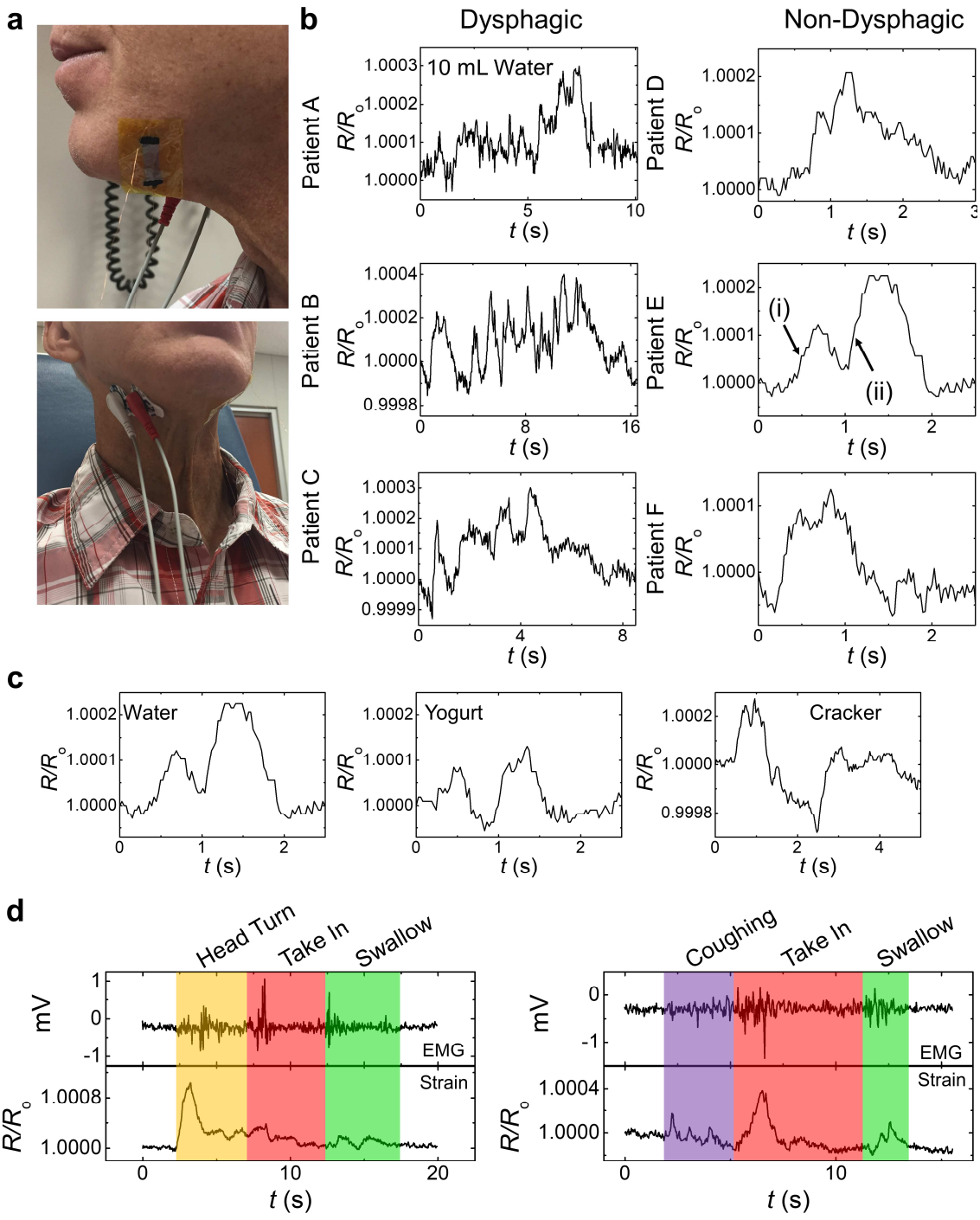

Figure 2.3. On-body experiments performed on dysphagic and non-dysphagic patients. (a) Photographs depicting the palladium nanoisland sensor on single-layer graphene and sEMG sensor applied to the submental region of a dysphagic patient. (b) Signals from three dysphagic (left) and non-dysphagic (right) patients while swallowing 10 mL of water. (c) Signals from a non-dysphagic patient swallowing 10 mL of water, 15 mL of yogurt, and 6 g from a cracker. (d) Signals from a non-dysphagic patient performing non-swallowing and swallowing activities.

Measurement of swallowing activity by strain alone can be confounded by motion artifacts (non-swallowing events). For example, coughs and head turns, which do not engage the swallowing muscles, may produce signals similar to those produced by swallowing. In order to detect a swallowing event unambiguously, we measured strain and electrical activity simultaneously. The signals observed in both sensing modalities can offer further insight into the electrical stimuli and mechanical actuation of the muscles in the submental region during swallowing. The strain and sEMG signals of a non-dysphagic patient as they turned their head from left to right (yellow) before facing forward and ingesting 10 mL of water (red & green) is shown in **Figure 2.3d**. By comparing the results from both the strain and sEMG sensors, we observed that the head turns from the non-dysphagic patient produced only a small signal in the sEMG, but a large signal in the strain plot. Additionally, the movements stemming from the non-dysphagic patient opening the mouth to take in the water, as well as swallowing the water, were clearly detectable by both the sEMG and the strain sensor. Another example of the identification of non-swallowing events using both sensing modalities can be seen in the adjacent plot, which depicts the signal of a strain sensor and sEMG sensor as the same non-dysphagic patient coughed three times, sipped and held 10 mL of water, and finally swallowed the water. Similar to the signals observed when the patient turned their head, the three coughs performed by the patient produced a negligible signal by the sEMG sensor that was difficult to distinguish, but produced three distinct strain signals detected by the strain sensor (**Figure 2.3d**, purple). While the coughs of the patient were not detected simultaneously by both the sEMG and strain sensing modalities, the activity in the submental region as the patient took in 10 mL of water (**Figure 2.3d**, red) and swallowed the bolus (**Figure 2.3d**, green) was detected by both modalities. Due to the fact that the strain sensor device detects larger strains for the non-swallowing events when compared to

the swallowing events, the use of both sensing modalities can be useful in order to differentiate these non-swallowing artefacts from the swallowing events that clinicians are interested in. The bimodal plots also offer insight into muscle behavior, as the time for the strain sensor to relax was longer than that for the sEMG sensor. The difference in relaxation time suggests that the time it took for the electrical stimulus to actuate the muscle contraction to perform the swallow was shorter than the time it took for the muscles to perform the muscle contraction mechanically. The fact that the signal detected from the sEMG sensor was shorter in duration than the signal from the strain sensor may also be attributed to the time it took for the submental region to fully relax (*i.e.*, skin and biological tissue is viscoelastic). The combination of the two sensing modalities can help speech pathologists gain more information about the swallowing function of a patient with respect to the electrical actuation of the muscles in the submental region and their mechanical performance. During the cohort study on head and neck cancer patients, we observed the quality of data acquired by these sensors may be reduced by the presence of loose skin and subcutaneous fat or edema. The elasticity of the skin in the submental region can be compromised due to many factors such as weight fluctuation, fibrosis, and the age of a patient. Furthermore, the formation of a dewlap on head and neck cancer patients, as a side effect, after radiation treatment can cause further separation of the skin surface from the swallowing muscles.[38] This separation can lessen the amount of strain and electrical signal detected on the surface of the skin due to the contraction of the muscles when swallowing.

2.2.4. Comparison of strain data to videofluoroscopy

A device meant for home use is only valuable to the extent that the data collected by it matches data produced by procedures used in the clinic. We thus sought to assign features in the data obtained from the sensors to actual events occurring in the mouth and pharynx. In order to

correlate the swallowing function recorded by the wearable sensors to actual swallowing activity, we compared the data to images of swallowing events obtained by videofluoroscopy performed after radiation therapy but not simultaneously acquired with sensor experiments due to the impracticality of obtaining these data concurrently. The strain signals of a dysphagic and non-dysphagic patient with snapshots of their respective videofluoroscopy data overlaid at the appropriate time points is shown in **Figure 2.4**. By monitoring the strain signal of the non-dysphagic patient and comparing it to the snapshots from the videofluoroscopy of the patient while swallowing a liquid barium solution of similar volume, we observed that the two distinct instances of tensile strain experienced on the skin may be attributed to the normal contractions of the muscles during a regular swallowing event (**Figure 2.4a**).[39,40] The first (smaller) strain event detected by the sensor appears attributed to the oral transit phase of the swallow, where the tongue propels the bolus to the back of the mouth and toward the pharynx. The second and larger tensile strain appears attributed to the pharyngeal phase of the swallow, which involves the contraction of the mylohyoid, digastric, and geniohyoid muscles as well as longitudinal pharyngeal muscles to protect the airway as the bolus moves toward the esophagus.[41–43] Conversely, the signal from the dysphagic patient, differs significantly from the signal of the non-dysphagic patient with respect to the duration of the swallow and number of events where the skin in the submental region undergoes tensile and compressive strain (**Figure 2.4b**). By observing the videofluoroscopy results for this patient for a similar bolus to the one used during the strain measurements, the multiple peaks during the swallow and the longer time to complete the swallow might be attributed to the multiple swallows performed by the patient to ingest the bolus completely. Similar studies made by previous groups have determined that the swallowing complications of dysphagic patients will require them to ingest a single bolus by multiple

successive swallows. The successive swallows arising from these complications will increase the duration to swallow a given bolus when compared to a non-dysphagic patient.

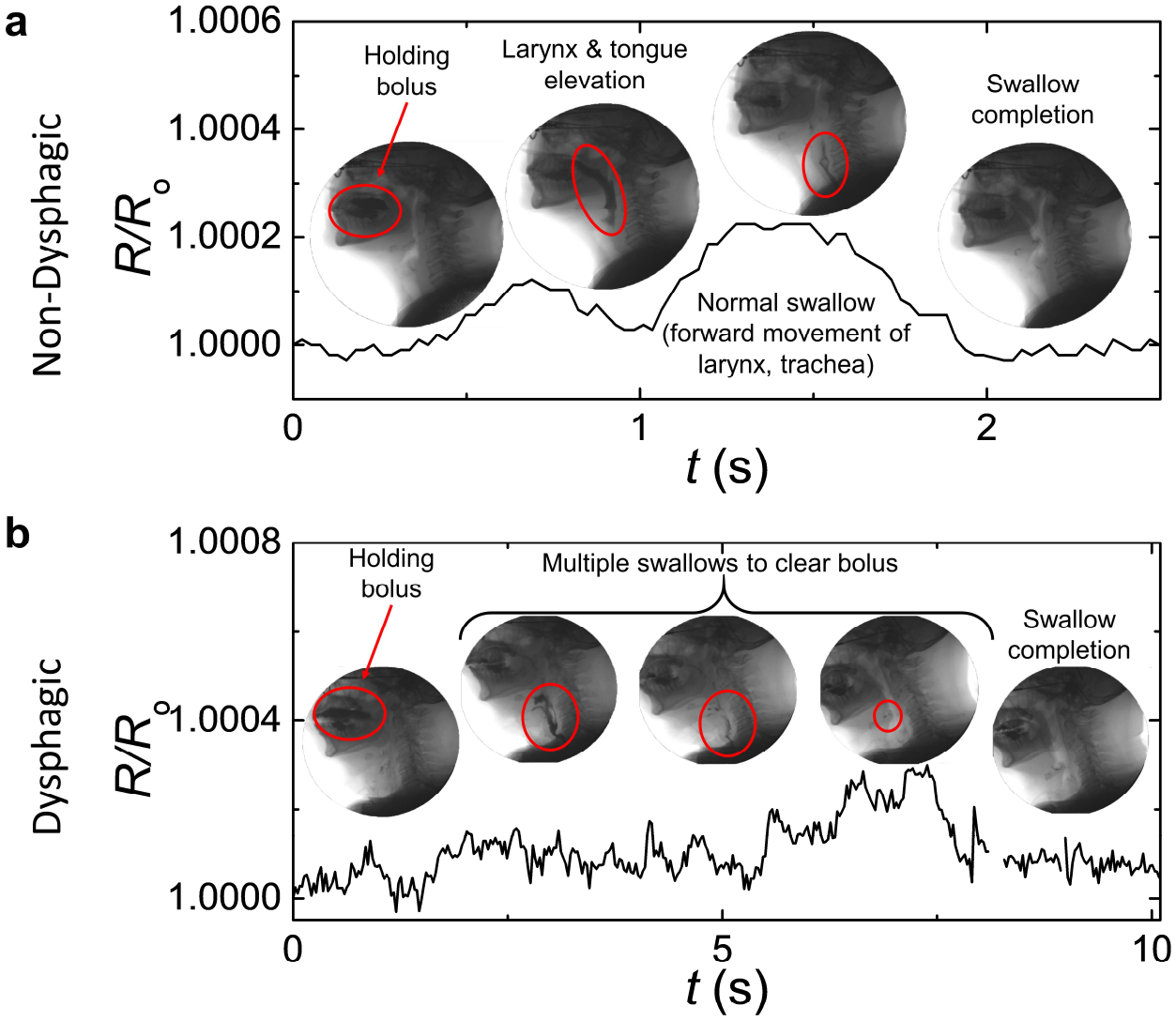

Figure 2.4. Correlation of strain data obtained from head and neck cancer patients with their corresponding videofluoroscopy experiments. The strain signals of (a) a non-dysphagic patient (Patient E) and (b) a dysphagic patient (Patient A) when swallowing 10 mL of water were compared to videofluoroscopy experiments done on the patients at a previous time. Analysis of the videofluoroscopy experiments combined with strain signals indicate differences in the strain events and time to complete a swallow between the two patients. These differences are caused appear related to the altered swallowing function of the dysphagic patient, which forces swallowing 10 mL of water in multiple swallows.

2.2.5. Development of machine learning algorithm

Building upon visual analysis of the swallowing signals from on-body trials, we developed a machine learning algorithm to perform preliminary tasks in order to differentiate swallowing signals as a proof-of-concept. The machine learning algorithm was developed to automate identification tasks for multiple swallowing signals, either from a healthy subject (age 24, male) or a dysphagic patient, to perform two classification tasks. The first task of the machine learning algorithm involved identifying a given swallowing signal from the healthy subject as the signal of the subject swallowing either 10 mL of water, 15 mL of yogurt, or 6 g of a cracker. The first task has relevance when considering that speech pathologists use food groups of different consistencies in order to make a more complete assessment of a patient's swallowing function. A schematic diagram of the development of the machine learning algorithm, with the task of identifying a bolus used as an example is shown in **Figure 2.5**. Shown in **Figure 2.5a**, the algorithm was trained with multiple swallows of the three boluses (red gradient) to develop the classifier models for each signal (blue). Before developing the classifier models, the signals were preprocessed by interpolating the data to have regular time intervals per resistance measurement and by fitting an approximate smooth curve to minimize the amount of noise among signals of the same bolus (see **Figure A.0.4**). The signals were then aligned with respect to time, and the features of the bolus signals were extracted by unsupervised learning (see **Figure A.0.5**). After the extraction of the features, the three classifier models were developed to perform the bolus classification task, where the accuracy of the bolus identification algorithm was tested through cross-validation techniques. **Figure 2.5b** depicts a scenario in which a new swallowing signal (green) is identified as the signal of one of three boluses using the three classifier models as scoring metrics for identification. An efficient classification model based on the L1-distance of

the per-class average (seen in **Equation A.0.1**) was the most accurate model, with an accuracy of 86.4% for the first task.

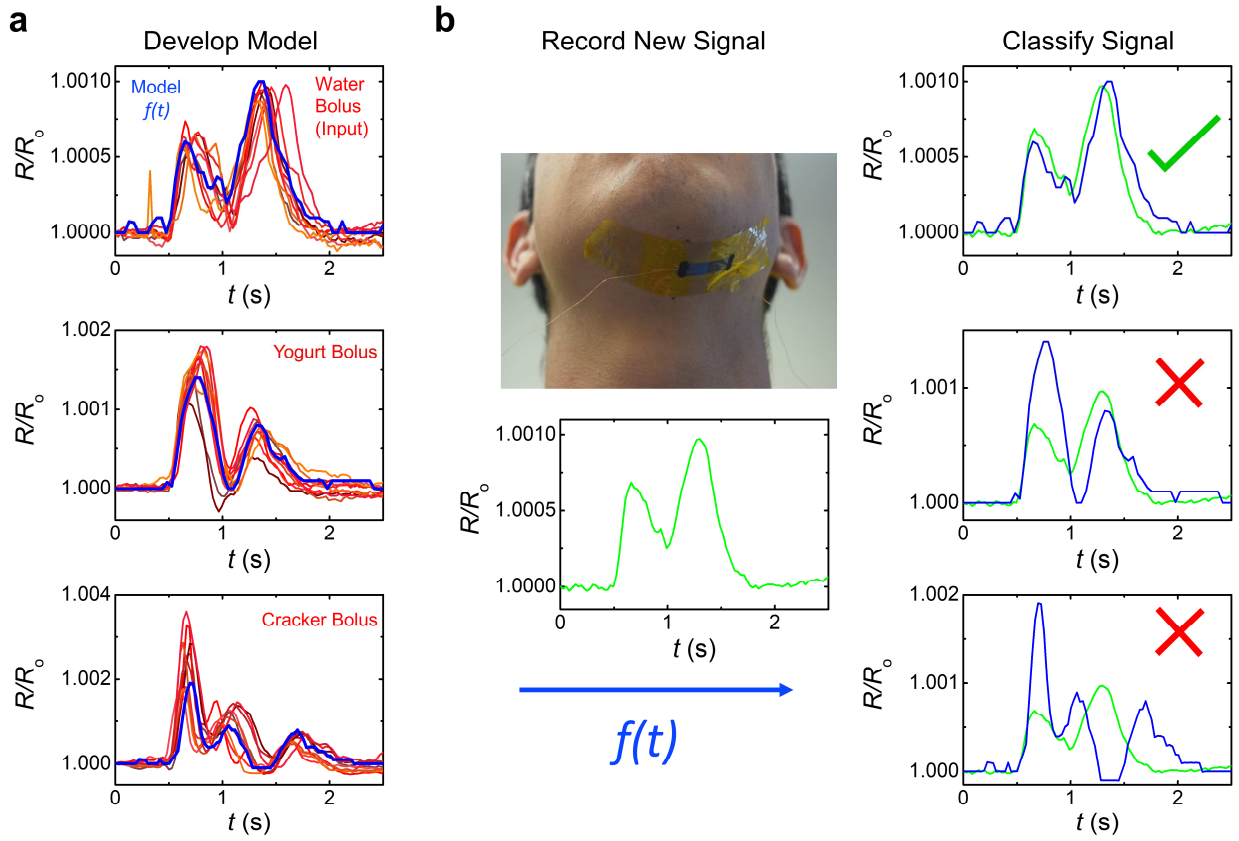

Figure 2.5. Schematic demonstrating the development and testing of the classification machine learning algorithm, using the bolus identification task as an example. The machine learning algorithm was (a) first trained on the strain data of three boluses (red). Once the main features of the training data are extracted, a classifier algorithm (blue) was developed to (b) classify new swallowing data (green) into one of the three bolus categories. The accuracy of the model was assessed to be 86.4% by cross-validation techniques (see Supporting Information). For details on model development and additional tasks performed, refer to the Supporting Information.

The second task involved identifying an unknown swallow (10 mL water) as either that of the healthy subject (age 24, male) or a patient exhibiting mild dysphagia (Patient H in **Table A.0.1**). The signals generated by the mildly dysphagic patient were similar to the signals generated by the healthy subject with respect to timescale and magnitude of strain, and thus we

presented an intentional challenge to the machine learning algorithm. This task was designed to demonstrate whether or not the algorithm could detect cases of gradual deterioration in swallowing function on the way to dysphagia. This task, which used the data of a patient with mild dysphagia, mimics the creeping development of dysphagia more so than would comparing a healthy subject and a severely dysphagic patient. Given the ideal application for this device as a daily complement to the MBS exam, which can only be administered periodically (1 exam every 3-6 months), the device paired with the machine-learning algorithm would have to detect the gradual evolution in swallowing activity over time. Shown in **Figure 2.6a**, the algorithm was trained with multiple swallows of either the healthy subject or the dysphagic patient (red gradients) to develop the classifier models for each situation (blue). After the extraction of the features, the two classifier models were developed to perform the subject classification task, where the accuracy of the algorithm was tested through cross-validation techniques. **Figure 2.6b** depicts a scenario in which a new swallowing signal (green) is identified as either the swallow of a healthy subject, or the swallow of a dysphagic patient, using the classifier models as scoring metrics for identification. Similar to the first task, the classification model based on the L1-distance of the per-class average was the most accurate model, with an accuracy of 94.7%. The tasks performed by the machine learning algorithm demonstrate the potential to combine algorithms with wearable sensors to monitor and potentially identify degradation in the swallowing function of head and neck cancer patients. Moreover, the use of machine learning algorithms which combine input from both strain and sEMG measurements could potentially be used to differentiate degradation in swallowing activity arising from radiation therapy from degradation arising from other diseases of the head and neck.

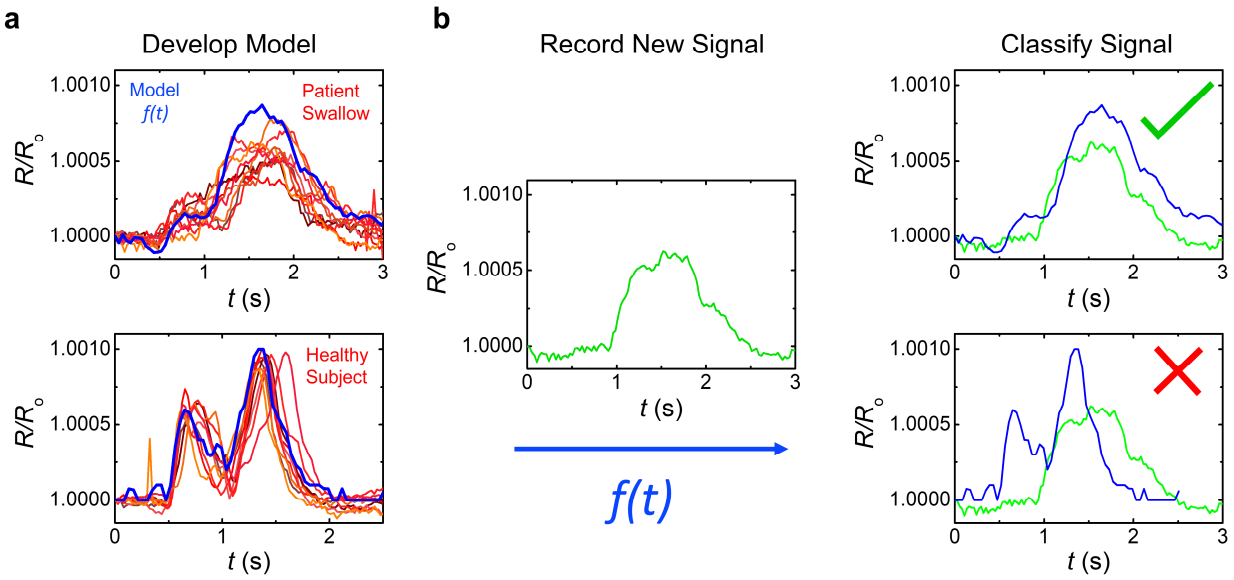

Figure 2.6. Schematic demonstrating the development and testing of the classification machine learning algorithm, using the bolus identification task as an example. The machine learning algorithm (a) was first trained on the strain data of both human subjects (red). Once the main features of the training data are extracted, a classifier algorithm (blue) was developed to (b) classify new swallowing data (green) as either the swallowing of 10 mL by a healthy subject or a dysphagic patient. The accuracy of the model was assessed to be 94.7% by cross-validation techniques (see Supporting Information). Details on the model development and additional tasks performed can be seen in Supporting Information.

2.3. Conclusions

The wearable and flexible strain sensor presented here demonstrates the potential for remote monitoring of patients outside of the clinic. Its distinctive morphology, resulting from the growth of palladium nanoparticles on graphene, produces a piezoresistive response sufficiently sensitive for detecting strains of physiological importance. By exploiting the exceptional piezoresistive properties, we fabricated a device capable of detecting swallowing activity for the remote monitoring of dysphagia. The real-world utility of this device was investigated by recording the swallowing activity of 14 head and neck cancer patients when placed on the submental region. The strain sensor was able to detect differences in swallowing activity based on (1) the type of boluses being ingested by a healthy non-cancer subject and a non-dysphagic patient and (2) functional *vs.* dysphagic swallow status in head and neck cancer patients who had

been treated with radiation to the throat. Combining the piezoresistive sensing modality with sEMG also provided further insight as to how the muscles in the submental region are actuated and how they relax after swallowing. Comparison of these non-invasive methods with videofluoroscopy—the current gold standard, in which a paste containing barium is swallowed under X-ray irradiation—suggests that our patch-like devices have the potential to produce data of sufficient clinical value to permit self-monitoring, and ultimately increase the quality of life of head and neck cancer survivors. A proof-of-concept machine learning algorithm was developed to identify the bolus being swallowed by a healthy subject and to distinguish between the signals of a healthy subject and a dysphagic patient swallowing the same bolus, highlighting further potential use of wearable devices by clinicians.

2.4. Methods

2.4.1. Wearable palladium nanoisland sensor

Single-layer graphene, supported on a copper foil substrate, was purchased from Graphenea. A nominal thickness of 8 nm of palladium nanoislands was deposited on top of the graphene on copper foil using thermal evaporation on an Orion System (AJA International) at a rate of 0.02 Å/s. A stainless steel stencil (Metal Etch Services, San Marcos, CA) was used to deposit the palladium nanoislands in a dog bone shape, as shown in **Figure 2.1**. 50 nm of aluminum was deposited at 1.5 Å/s on top of the palladium by sputtering. The aluminum layer served as a mask to selectively etch off the graphene around the dog bone pattern. The graphene surrounding the dog bone was then etched by oxygen plasma for 5 min. Afterward, the graphene on the back of the copper foil was etched off by oxygen plasma for 5 min. Similarly, the aluminum film was etched by submerging the sensor films into 0.025 M KOH in water (Fisher Scientific) for 1 min, leaving the dog bone shape that comprises palladium nanoislands on a

single layer of graphene. After etching the aluminum film, 4% PMMA (by mass) (Alfa Aesar) in anisole (Acros Organics) was deposited on top of the palladium nanoislands/graphene/copper by spin coating (4000 rpm, 4000 rpm/s, 60 s). The film was then heated to 150 °C for 10 min to remove residual solvent. The supporting copper foil was etched away in 0.05 g/mL ammonium persulfate (Acros Organics**) in water**. The film of PMMA/palladium nanoislands/graphene was transferred out of the ammonium persulfate by adhering the edge of the film to a glass slide, lifting out the film from the ammonium persulfate, and plunging the glass slide into a water bath, releasing the film on the surface of the water. The PMMA/palladium nanoislands/graphene film was then transferred onto the final receiving substrate (Caplinq, product number PIT0.5S UT/25.4) by adhering one edge of the film onto the polyimide tape, supported on a glass slide, and plunging the glass slide into the water bath. The transfer results in the PMMA film being adhered to the polyimide tape, with the graphene facing upward (graphene/palladium nanoislands/PMMA/polyimide tape). The substrate used to develop the strain sensor for this study—a polyimide tape that is 13 μm thick—offered mechanical robustness and flexibility sufficient to accommodate mechanical deformations of the submental region during swallowing. The sensor was then addressed with copper wire, with a carbon paint painted on the contact area (DAG-T-502, Ted Pella, Inc.) and left to dry.

2.4.2. Cantilever strain experiment

For the cantilever strain experiment. The device was adhered to a 1 ✕ 2 in willow glass substrate (Corning), as a cantilever substrate. The device on willow glass was then partially suspended, clamped at a 1 cm overlap, over a step edge of a 1.25 mm using Si wafers (University Wafer), with the strain sensor fully suspended in air. The tensile strain applied to the sensor device was calculated using a simple continuum mechanics model.[44] The axial strain is modeled

analytically by the equation $\varepsilon_{ZZ} = \frac{6bh}{4L^2 - 5aL + a^2}$, where b is the step edge height, h is the thickness of the substrate, a is the distance from the clamped end to the nanowire, and L is the total length between clamped end and displaced end. By the dimensions of our experimental setup on AutoCAD, we determined the strain experienced by the device during the cantilever experiment corresponds to a radius of curvature of approximately 58 cm.

2.4.3. Strain and sEMG sensor placement and data acquisition

Before placing the wearable strain sensor on the submental region of the human subject or head and neck cancer patients, the area of interest was wiped with isopropanol to remove oil and dirt from the skin. A makeup adhesive (Spirit Gum, Mehron) was brushed onto the adhesive side of the tape of the sensor substrate. The makeup adhesive was left to dry for approximately 5 min, before placing the sensor onto the skin. The sensor was placed on the surface of the skin in the submental region, where the mylohyoid and geniohyoid muscles are. Conventional sEMG electrodes were used in parallel with the strain sensor. In clinical practice using sEMG biofeedback for therapeutic applications with dysphagic populations, the most common placements are in the submental region and lateral to the larynx. For the sEMG sensing modality, the reference electrode was placed on the skin surface near the carpal bone of the left wrist. The working and counter electrodes were placed on the surface of the skin in the submental region, symmetrically across from the strain sensor and atop the same muscle groups next to where the strain sensor was placed. The sEMG circuit was configured to use a low-pass filter of 2 kHz and a high-pass filter of 30 Hz. The signal was amplified with a minimum gain of 550 and a max gain of 1600. sEMG Red Dot electrodes were purchased from 3M (Model 2560) and used as received. The strain sensor device was addressed to a Keithley 2601B SourceMeter to acquire

the strain sensor data and the sEMG data was acquired by a Keithley 2400 SourceMeter. Both the strain and sEMG data was sent to LabVIEW for recording and processing.

2.4.4. On-body experiments on head and neck cancer patients

On-body tests were first performed on a completely healthy subject (age 24, male) before being conducted on fourteen head and neck cancer patients who were previously treated with radiation therapy. This study consisted of twelve male and two female patients of ages ranging from 43-83 years. Seven out of these fourteen patients were diagnosed based on videofluoroscopy with at least moderate dysphagia (DIGEST grade ≥2). In 6 out of the 7 dysphagic cases, DIGEST scores (grade ≥2) were commensurate with self-reported status. In the 7^{th} case, a recent MBS was not available but patient's dysphagic status was verified with physician observation, based on long-term gastrostomy dependence with poor secretion management. All seven patients who suffered from dysphagia underwent radiation therapy to bilateral cervical fields. All on-body experiments on head and neck cancer patients were performed with approval from an Internal Review Board (protocol number 2016-0597) of MD Anderson Cancer Center. For the swallowing experiments, the boluses consisted of a small sip of water (10 mL), a tablespoon (15 mL) of yogurt, or a bite from a cracker (~6 g). The healthy subject and patients were asked to take in a bolus into their mouth, hold the bolus in their mouth until the signals from the strain sensor baselined, and then were asked to swallow the bolus.

2.4.5. Machine learning analysis

Machine learning algorithms have recently been implemented in applications that involve interpreting and analyzing sensor data.[45,46] We developed a machine learning algorithm around our strain sensor data to determine if statistical models could correctly classify new swallowing signals. First, we established whether or not swallowing signals for a given subject could be

classified based on the bolus being swallowed (liquid, yogurt, or cracker). Second, we determined if the swallowing signal of a healthy subject (age 24, male) could be distinguished from that of a dysphagic one (DIGEST grade 4). Performing tasks such as identifying boluses being swallowed by a patient and identifying abnormal swallowing could offer swallowing information, usually acquired in a clinic, to a speech pathologist remotely and without the need to limit the diet of a patient. Wearable systems that can obtain and analyze data could help clinicians monitor the development of dysphagia in head and neck cancer patients and potentially obtain a much earlier diagnosis than is possible using current methods.

Acknowledgements

This work was supported by the National Institutes of Health Director's New Innovator Award, grant 1DP2EB022358-01 to D.J.L., and by a Diversity Supplement (for B.C.M.) under award number 1DP2EB022358-01S1. E.A. received partial support from the CANASA/UCSD Space Grant Consortium. J.R. and D.R. acknowledge support provided by the National Science Foundation Graduate Research Fellowship Program under Grant No. DGE-1144086. This work was performed in part at the San Diego Nanotechnology Infrastructure (SDNI), a member of the National Nanotechnology Coordinated Infrastructure, which is supported by the National Science Foundation (grant ECCS-1542148). This work was performed in part at the University of Texas MD Anderson Cancer center, which is supported by the NCI Cancer Center Support Grant (P30CA016672). The authors would also like to thank Mohammad A. Alkhadra for his help in proofreading the manuscript.

Chapter 2, in full, is a reprint of the material as it appears in *ACS Nano* **2018**, *12* (6), 5913–5922. American Chemical Society, 2018. Julian Ramírez, Daniel Rodriquez, Fang Qiao, Julian Warchall, Jasmine Rye, Eden Aklile, Andrew S-C. Chiang, Brandon C. Marin, Patrick P.

Mercier, CK Cheng, Katherine A. Hutcheson, Eileen H. Shinn, and Darren J. Lipomi. The dissertation author was the primary investigator and author of this paper.

References

(1) Rosenthal, D. I.; Lewin, J. S.; Eisbruch, A. Prevention and Treatment of Dysphagia and Aspiration after Chemoradiation for Head and Neck Cancer. *J. Clin. Oncol.* **2006**, *24*, 2636–2643.

(2) Bleier, B. S.; Levine, M. S.; Mick, R.; Rubesin, S. E.; Sack, S. Z.; McKinney, K.; Mirza, N. Dysphagia after Chemoradiation: Analysis by Modified Barium Swallow. *Ann. Otol. Rhinol. Laryngol.* **2007**, *116*, 837–841.

(3) American Cancer Society. Cancer Facts & Figures 2017. *Cancer Facts Fig. 2017* **2017**, 1.

(4) Siegel, R. L.; Miller, K. D.; Jemal, A. Cancer Statistics, 2017. *CA. Cancer J. Clin.* **2017**, *67*, 7–30.

(5) Howlader, N.; Noone, A. M.; Krapcho, M.; Neyman, N.; Aminou, R.; Altekruse, S. F.; Kosary, C. L.; Ruhl, J.; Tatalovich, Z.; Cho, H.; Mariotto, A.; Eisner, M.P.; Leiws, D.R.; Chen, H.S.; Feuer, E.J.; Cronin, K.A. *SEER Cancer Statistics Review, 1975-2009 (Vintage 2009 Populations)*; 2011.

(6) Garden, A. S.; Kies, M. S.; Morrison, W. H.; Weber, R. S.; Frank, S. J.; Glisson, B. S.; Gunn, G. B.; Beadle, B. M.; Ang, K. K.; Rosenthal, D. I.; Sturgis, E.M. Outcomes and Patterns of Care of Patients with Locally Advanced Oropharyngeal Carcinoma Treated in the Early 21st Century. *Radiat. Oncol.* **2013**, *8*, 21.

(7) Ridner, S. H.; Dietrich, M. S.; Niermann, K.; Cmelak, A.; Mannion, K.; Murphy, B. A Prospective Study of the Lymphedema and Fibrosis Continuum in Patients with Head and Neck Cancer. *Lymphat. Res. Biol.* **2016**, *14*, 198–205.

(8) Logemann, J. A. Role of the Modified Barium Swallow in Management of Patients with Dysphagia. *Otolaryngol. - Head Neck Surg.* **1997**, *116*, 335–338.

(9) Martin-Harris, B.; Logemann, J. a; McMahon, S.; Schleicher, M.; Sandidge, J. Clinical Utility of the Modified Barium Swallow. *Dysphagia* **2000**, *15*, 136–141.

(10) Hutcheson, K. A.; Barrow, M. P.; Barringer, D. A.; Knott, J. K.; Lin, H. Y.; Weber, R. S.; Fuller, C. D.; Lai, S. Y.; Alvarez, C. P.; Raut, J.; Lazarus, C.L.; May, A.; Patterson, J.; Roe, J.W.; Starmer, H.M.; Lewin, J.S. Dynamic Imaging Grade of Swallowing Toxicity (DIGEST): Scale Development and Validation. *Cancer* **2016**, 1–9.

(11) Mortensen, H. R.; Jensen, K.; Aksglæde, K.; Behrens, M.; Grau, C. Late Dysphagia after IMRT for Head and Neck Cancer and Correlation with Dose-Volume Parameters. *Radiother. Oncol.* **2013**, *107*, 288–294.

(12) Caudell, J. J.; Schaner, P. E.; Meredith, R. F.; Locher, J. L.; Nabell, L. M.; Carroll, W. R.; Magnuson, J. S.; Spencer, S. A.; Bonner, J. A. Factors Associated With Long-Term Dysphagia After Definitive Radiotherapy for Locally Advanced Head-and-Neck Cancer. *Int. J. Radiat. Oncol. Biol. Phys.* **2009**, *73*, 410–415.

(13) Dale, T.; Hutcheson, K.; Mohamed, A. S. R.; Lewin, J. S.; Gunn, G. B.; Rao, A. U. K.; Kalpathy-Cramer, J.; Frank, S. J.; Garden, A. S.; Messer, J. A.; Warren, B.; Lai, S.Y.; Beadle, B.M.; Morrison, W.H.; Phan, J.; Skinner, H.; Gross, N.; Ferrarotto, R.; Weber, R.S.; Rosenthal, D.I.; Fuller, C. D. Beyond Mean Pharyngeal Constrictor Dose for Beam Path Toxicity in Non-Target Swallowing Muscles: Dose-Volume Correlates of Chronic Radiation-Associated Dysphagia (RAD) after Oropharyngeal Intensity Modulated Radiotherapy. *Radiother. Oncol.* **2016**, *118*, 304–314.

(14) Caudell, J. J.; Schaner, P. E.; Desmond, R. A.; Meredith, R. F.; Spencer, S. A.; Bonner, J. A. Dosimetric Factors Associated With Long-Term Dysphagia After Definitive Radiotherapy for Squamous Cell Carcinoma of the Head and Neck. *Int. J. Radiat. Oncol. Biol. Phys.* **2010**, *76*, 403–409.

(15) Caglar, H. B.; Tishler, R. B.; Othus, M.; Burke, E.; Li, Y.; Goguen, L.; Wirth, L. J.; Haddad, R. I.; Norris, C. M.; Court, L. E.; Aninno, D.J.; Posner, M.R.; Allen, A.M. Dose to Larynx Predicts for Swallowing Complications After Intensity-Modulated Radiotherapy. *Int. J. Radiat. Oncol. Biol. Phys.* **2008**, *72*, 1110–1118.

(16) Gupta, V.; Reddy, N. P.; Canilang, E. P. Surface EMG Measurements at the Throat during Dry and Wet Swallowing. *Dysphagia* **1996**, *11*, 173–179.

(17) Vaiman, M.; Eviatar, E. Surface Electromyography as a Screening Method for Evaluation of Dysphagia and Odynophagia. *Head Face Med.* **2009**, *5*, 9.

(18) Vaiman, M. Standardization of Surface Electromyography Utilized to Evaluate Patients with Dysphagia. *Head Face Med.* **2007**, *3*, 26.

(19) Yoshida, M.; Groher, M. E.; Crary, M. A.; Mann, G. C.; Akagawa, Y. Comparison of Surface Electromyographic (sEMG) Activity of Submental Muscles between the Head Lift and Tongue Press Exercises as a Therapeutic Exercise for Pharyngeal Dysphagia. *Gerodontology* **2007**, *24*, 111–116.

(20) Constantinescu, G.; Jeong, J. W.; Li, X.; Scott, D. K.; Jang, K. I.; Chung, H. J.; Rogers, J. A.; Rieger, J. Epidermal Electronics for Electromyography: An Application to Swallowing Therapy. *Med. Eng. Phys.* **2015**, *38*, 807–812.

(21) Segev-Bar, M.; Haick, H. Flexible Sensors Based on Nanoparticles. *ACS Nano* **2013**, *7*, 8366–8378.

(22) Tao, L.-Q.; Wang, D.-Y.; Tian, H.; Ju, Z.-Y.; Liu, Y.; Pang, Y.; Chen, Y.-Q.; Yang, Y.; Ren, T.-L. Self-Adapted and Tunable Graphene Strain Sensors for Detecting Both Subtle and Large Human Motions. *Nanoscale* **2017**, *9*, 8266–8273.

(23) Tao, L.-Q.; Tian, H.; Liu, Y.; Ju, Z.-Y.; Pang, Y.; Chen, Y.-Q.; Wang, D.-Y.; Tian, X.-G.; Yan, J.-C.; Deng, N.-Q.; Yang, Y.; Ren, T.-L. An Intelligent Artificial Throat with Sound-Sensing Ability Based on Laser Induced Graphene. *Nat. Commun.* **2017**, *8*, 14579.

(24) Xu, R.; Wang, D.; Zhang, H.; Xie, N.; Lu, S.; Qu, K. Simultaneous Detection of Static and Dynamic Signals by a Flexible Sensor Based on 3D Graphene. *Sensors* **2017**, *17*, 1069.

(25) Wang, L.; Jackman, J. A.; Tan, E.; Park, J. H.; Potroz, M. G.; Hwang, E. T.; Cho, N.-J. High-Performance, Flexible Electronic Skin Sensor Incorporating Natural Microcapsule Actuators. *Nano Energy* **2017**, *36*, 38–45.

(26) Hwang, B. U.; Lee, J. H.; Trung, T. Q.; Roh, E.; Kim, D. Il; Kim, S. W.; Lee, N. E. Transparent Stretchable Self-Powered Patchable Sensor Platform with Ultrasensitive Recognition of Human Activities. *ACS Nano* **2015**, *9*, 8801–8810.

(27) Zhu, Y.; Hu, Y.; Zhu, P.; Zhao, T.; Liang, X.; Sun, R.; Wong, C. Enhanced Oxidation Resistance and Electrical Conductivity Copper Nanowires–graphene Hybrid Films for Flexible Strain Sensors. *New J. Chem.* **2017**, *41*, 4950–4958.

(28) Li, W.; Guo, J.; Fan, D. 3D Graphite-Polymer Flexible Strain Sensors with Ultrasensitivity and Durability for Real-Time Human Vital Sign Monitoring and Musical Instrument Education. *Adv. Mater. Technol.* **2017**, *2*, 1700070.

(29) Ertekin, C.; Pehlivan, M.; Aydoğdu, I.; Ertaşl, M.; Uludağ, B.; Çlelebi, G.; Çlolakoğlu, Z.; Sağduyu, A.; Yüceyar, N. An Electrophysiological Investigation of Deglutition in Man. *Muscle Nerve* **1995**, *18*, 1177–1186.

(30) Ertekin, C. Electrophysiological Evaluation of Oropharyngeal Swallowing in Myotonic Dystrophy. *J. Neurol. Neurosurg. Psychiatry* **2001**, *70*, 363–371.

(31) Ashida, I.; Miyaoka, S.; Miyaoka, Y. Comparison of Video-Recorded Laryngeal Movements during Swallowing by Normal Young Men with Piezoelectric Sensor and Electromyographic Signals. *J. Med. Eng. Technol.* **2009**, *33*, 496–501.

(32) Li, Q.; Hori, K.; Minagi, Y.; Ono, T.; Chen, Y.; Kondo, J.; Fujiwara, S.; Tamine, K.; Hayashi, H.; Inoue, M.; Maeda, Y. Development of a System to Monitor Laryngeal Movement during Swallowing Using a Bend Sensor. *PLoS One* **2013**, *8*, e70850.

(33) Schultheiss, C.; Schauer, T.; Nahrstaedt, H.; Seidl, R. O. Automated Detection and Evaluation of Swallowing Using a Combined Emg/bioimpedance Measurement System. *Sci. World J.* **2014**, *2014*.

(34) Schultheiss, C.; Schauer, T.; Nahrstaedt, H.; Seidl, R. O. Evaluation of an EMG Bioimpedance Measurement System for Recording and Analysing the Pharyngeal Phase of Swallowing. *Eur. Arch. Oto-Rhino-Laryngology* **2013**, *270*, 2149–2156.

(35) Zaretski, A. V; Root, S. E.; Savchenko, A.; Molokanova, E.; Printz, A. D.; Jibril, L.; Arya, G.; Mercola, M.; Lipomi, D. J. Metallic Nanoislands on Graphene as Highly Sensitive Transducers of Mechanical, Biological, and Optical Signals. *Nano Lett.* **2016**, *16*, 1375–1380.

(36) Marin, B. C.; Ramirez, J.; Root, S. E.; Aklile, E.; Lipomi, D. J. Metallic Nanoislands on Graphene: A Metamaterial for Chemical, Mechanical, Optical, and Biological Applications. *Nanoscale Horiz.* **2017**.

(37) Reimers-Neils, L.; Logemann, J.; Larson, C. Viscosity Effects on EMG Activity in Normal Swallow. *Dysphagia* **1994**, *9*, 101–106.

(38) Young, J. R. Radiation Dewlap. *Clin. Otolaryngol.* **1979**, *4*, 25–28.

(39) Standring, S. *Gray's Anatomy: The Anatomical Basis of Clinical Practice*; 41st ed.; 2016.

(40) Mankekar, G. *Swallowing - Physiology, Disorders, Diagnosis and Therapy*; 2015.

(41) Pearson, W. G.; Langmore, S. E.; Yu, L. B.; Zumwalt, A. C. Structural Analysis of Muscles Elevating the Hyolaryngeal Complex. *Dysphagia* **2012**, *27*, 445–451.

(42) Pearson, W. G.; Hindson, D. F.; Langmore, S. E.; Zumwalt, A. C. Evaluating Swallowing Muscles Essential for Hyolaryngeal Elevation by Using Muscle Functional Magnetic Resonance Imaging. *Int. J. Radiat. Oncol. Biol. Phys.* **2013**, *85*, 735–740.

(43) Shaw, S. M.; Martino, R. The Normal Swallow: Muscular and Neurophysiological Control. *Otolaryngol. Clin. North Am.* **2013**, *46*, 937–956.

(44) Jibril, L.; Ramírez, J.; Zaretski, A. V.; Lipomi, D. J. Single-Nanowire Strain Sensors Fabricated by Nanoskiving. *Sensors Actuators A Phys.* **2017**, *263*, 702–706.

(45) Jeon, H.; Lee, W.; Park, H.; Lee, H.; Kim, S.; Kim, H.; Jeon, B.; Park, K. Automatic Classification of Tremor Severity in Parkinson's Disease Using a Wearable Device. *Sensors* **2017**, *17*, 2067.

(46) Lonini, L.; Shawen, N.; Ghaffari, R.; Rogers, J.; Jayarman, A. Automatic Detection of Spasticity from Flexible Wearable Sensors. In *Proceedings of the 2017 ACM International Joint Conference on Pervasive and Ubiquitous Computing and Proceedings*

of the 2017 ACM International Symposium on Wearable Computers on - UbiComp '17; ACM Press: New York, New York, USA, 2017; pp. 133–136.

Chapter 3 Combining High Sensitivity and Dynamic Range: Wearable Thin-Film Composite Strain Sensors of Graphene, Ultrathin Palladium, and PEDOT:PSS

Abstract

Wearable mechanical sensors have the potential to transform healthcare by enabling patient monitoring outside of the clinic. A critical challenge in the development of mechanical—e.g., strain—sensors is the combination of sensitivity, dynamic range, and robustness. This work describes a highly sensitive and robust wearable strain sensor composed of three layered materials: graphene, an ultrathin film of palladium, and highly plasticized PEDOT:PSS. The role of the graphene is to provide a conductive, manipulable substrate for the deposition of palladium. When deposited at low nominal thicknesses (~8 nm) palladium forms a rough, granular film which is highly piezoresistive (i.e., the resistance increases with strain with high sensitivity). The dynamic range of these graphene/palladium films, however, is poor, and can only be extended to ~10% before failure. This fragility renders the films incompatible with wearable applications on stretchable substrates. To improve the working range of graphene/palladium strain sensors, a layer of highly plasticized PEDOT:PSS is used as a stretchable conductive binder. That is, the conductive polymer provides an alternative pathway for electrical conduction upon cracking of the palladium film and the graphene. The result was a strain sensor that possessed good sensitivity at low strains (0.001% engineering strain) but with a working range up to 86%. The piezoresistive performance can be optimized in a wearable device by sandwiching the conductive composite between a soft PDMS layer in contact with the skin and a harder layer at the air interface. When attached to the skin of the torso, the patch-like strain sensors were capable of detecting heartbeat (small strain) and respiration (large strain) simultaneously. This demonstration highlights the ability of the sensor to measure low and high strains in a single

interpolated signal, which could be useful in monitoring, for example, obstructive sleep apnea with an unobtrusive device.

3.1. Introduction

A major challenge in the development of wearable strain sensors is to combine low detection limits with high dynamic range. Ideally, a patch-like device would have the ability to sense minute mechanical strains originating underneath the skin (e.g., <0.1%) while also detecting—and not being destroyed by—large deformations (e.g., >10%). We present a highly sensitive and stretchable tattoo-like strain sensor that has a three-layer structure: (1) single-layer graphene decorated with (2) an ultrathin granular palladium film coated with (3) a thin film of highly plasticized PEDOT:PSS ("PEDOT dough").[1] We designed this "structured blend" to have multiple, synergistic, piezoresistive mechanisms. That is, the graphene provides an ultrathin and piezoresistive substrate for the deposition of the palladium. The granular film of palladium enhances the piezoresistive sensitivity of the graphene at low strains and decreases the overall electrical resistance. The plasticized PEDOT:PSS provides mechanical support and piezoresistance at high strains.[1,2] This composite material is capable of detecting strains as low as 0.001%, is electrically stable when strained as high as 86% (**Figure B.0.3**), and can be cyclically strained at least 250 cycles at 10% strain (**Figure B.0.7**). When attached to the torso, this piezoresistive sensor produced an interpolated signal containing large-amplitude modulations in resistance arising from respiration, along with smaller-amplitude ones arising from heartbeats.

3.2 Background

A variety of physiological processes produce mechanical signals which manifest at the surface of the skin. These signals include those arising from heartbeats, respiration, and movements of the voluntary muscles. Multifunctional wearable health monitors thus require

strain sensors with high sensitivity and dynamic range.[3–6] The most common type of strain sensor used for patch-like "epidermal"[7] or temporary tattoo-inspired devices are made using metallic traces, usually with thicknesses of hundreds of nanometers.[8] Metallic traces can be fabricated by deposition on rigid wafers from which they can be transferred to stretchable substrates.[8] The piezoresistance of a solid metallic film arises from the change in geometry upon stretching, in particular the increase in length and reduction in cross sectional dimensions. Geometric arguments show that the gauge factor—defined as $GF = \frac{\frac{\Delta R}{R}}{\varepsilon}$, where ΔR is the change in resistance of the sensor due to strain, R is the initial resistance, and ε is the applied strain—is limited to a maximum of 2.[9] While responsive to modest strains ($\leq 3\%$), metallic films tend to crack with greater deformations.[10] Additionally, the relatively low sensitivity of metallic films make them suitable to detect only large motions of the body.

To develop strain sensors with higher sensitivity, several research groups have used polymeric materials containing conductive nanomaterials as an alternative to metallic traces. As opposed to solid metallic traces, whose piezoresistance relies on a predictable change in geometry with strain, the mechanisms of nanomaterial-based strain sensors rely on displacement of conductive particles about their positions adopted at mechanical equilibrium. The overall mechanical behavior tends to depend on whether the polymer into which the nanoparticles are embedded (or onto which they are deposited) is hard or soft. There are many examples of piezoresistive nanoparticles integrated with hard polymers. For example, a sensor composed of carbon nanotubes in an epoxy matrix was capable of detecting strains as low as 0.01% with a gauge factor of 2.[11] This piezoresistance was attributed to the decrease in tunneling current as the carbon nanotubes were pulled apart.[11] Other groups developed strain sensors using graphene particles supported on flexible and stretchable substrates, capable of detecting low strains (<

0.1%) with wide ranging gauge factors (10^0–10^6).[12–14] The piezoresistance of graphene appears to arise from a change in electronic structure, as the elongation of C-C bonds of single-layer graphene causes a break in sublattice symmetry and opens the band gap.[15,16] Moreover, defects in graphene can also cause electron scattering that can further increase the resistance when the graphene is strained.[17,18] Other strategies to develop ultra-sensitive piezoresistive films include the use of thin metallic films on elastomeric substrates that are capable of detecting strains >1% with gauge factors ranging from 200 to 16,000 due to the formation of cracks in the films.[19–21] Sensors based on silicon MEMS devices are sensitive to small strains (0.00625-0.02%) with gauge factors of 20-40, but are not as stretchable as strain sensors based on nanoparticles embedded in or placed upon polymeric substrates.[22–24] While nanoparticle-based piezoresistors integrated with hard polymers are sensitive to small strains, these materials undergo electrical failure (open circuit) at modest strains (generally >2%).

The stretchability of a nanoparticle-based strain sensor can be increased by embedding the conductive particles in an elastomeric matrix.[25–27] Such sensors have been used to monitor stretching of the skin as a result of, for example, the bending of a joint.[28–31] Although these materials can accommodate large strains, they are generally not sensitive to strains of low magnitudes. It has often been observed that resistive strain sensors exhibit an inverse relationship between stretchability and sensitivity (e.g., gauge factor) of the material.[32,33] For example, stretchable sensors have been fabricated by coating elastic fibers with graphene and graphene oxide particles, which can withstand strains up to 100% and 150%, but have gauge factors of only 3.7 and 2 respectively.[34,35] Some methods to develop composite strain sensors include impregnating polydimethylsiloxane (PDMS) with a crumpled graphene/nanocellulose mix, stretchable up to 100% with a gauge factor of 7.[36] Other groups have made materials with higher

stretchability (~ 350%) or higher gauge factors (~35) but the same tradeoff between stretchability and sensitivity was observed.[37,38] Materials that are able to withstand large deformations with high sensitivity are appealing because they can offer the ability to detect subtle biomechanical signals interpolated with larger ones when used in wearable health monitoring applications.

Previous work by our group showed that an ultrathin palladium film on single-layer graphene transferred to PDMS can detect strains as low as 0.001% and stretch up to 9%.[2] These ultrathin films exhibit an island-like or granular morphology at nominal thicknesses of ≤10 nm (as measured by quartz crystal microbalance, QCM, during deposition). Unlike ultrathin films of other metals, which exhibit a much more disconnected island morphology and lower sensitivity, the morphologies of the films having the greatest sensitivity occur at the borderline between the discontinuous ("nanoisland") and continuous (though still granular) regimes with increasing nominal thicknesses. The morphology and interconnectivity of the grains depends strongly on the conditions used for deposition (e.g., deposition rate, substrate temperature, and identity of the substrate supporting the graphene[2]). We attribute the piezoresistivity of these films to several effects, which are operative to different degrees depending on the exact morphology of the granular film being used. These effects include (1) increased scattering of individual metallic nanostructures during stretching, (2) tunneling between closely spaced adjacent grains, (3) large-scale cracking and increased tortuosity of initially contiguous metal, and (4) the native piezoresistivity of graphene.[2] These films have been used by our group in a range of applications. For example, to monitor swallowing activity in patients treated for head and neck cancer,[39] to detect small strains produced by the contractions of cardiomyocytes,[2] and to measure the properties of fluids and solid objects in microfluidic devices by measuring the "bulge" that forms in sidewalls of the channels during transit.[40] A shortcoming of the metal-graphene

composite material is that it is limited by the fragility of graphene, which has a crack-onset strain of around 6% when supported by PDMS.[41] This drawback has previously limited the use of this material to applications where the sensor film rests on a substrate which was flexible (e.g., polyimide) but not stretchable.[39,42,43]

In this chapter, we report the development of a structured blend composite material consisting of single-layer graphene, ultrathin granular palladium, and a highly plasticized conductive polymer based on poly(3,4-ethylenedioxythiophene):poly(styrene sulfonate) (Gr/Pd/PEDOT:PSS, **Figure 3.1**). The conductivity and stretchability of PEDOT:PSS is well known to be improved with the use of additives; increased stretchability is required to make PEDOT:PSS compatible with skin-wearable applications.[44–46] The formulation of plasticized PEDOT:PSS, described by Oh and co-workers, consists of 92% wt PEDOT:PSS (2% wt dispersion in water), 3% wt Triton X-100 (a surfactant), and 5% wt DMSO.[1] The advantage of stacking these materials in a structured blend—as opposed to mixing them in a random blend—is that sensitivity can be retained with a wide dynamic range. By using a stack of conductive materials, the structured composite is able to detect strains as low as 0.001%, with stretchability up to 86% (**Figure A.0.3**), and thus the ability to sense the range of strains stemming from human activity. The device was capable of detecting strains arising from small- and large-strain events (e.g., simultaneous detection of heartbeats and respiration), demonstrating its potential to monitor conditions such as obstructive sleep apnea.

3.3 Results and Discussion

The structured blend of the Gr/Pd/PEDOT:PSS was designed to combine the high piezoresistivity of the Gr/Pd film with the stretchability of highly plasticized PEDOT:PSS. **Figure 3.1** illustrates the fabrication of the Gr/Pd/PEDOT:PSS sensor in two phases (deposition

of Gr/Pd and PEDOT:PSS, respectively). A granular film of palladium (nominal thickness of 8 nm) was evaporated on top of single-layer graphene supported on copper foil, followed by a sputter deposition of 50 nm of aluminum through a stencil containing a serpentine aperture (Step 1). The aluminum film served as an etch resist which would define for the serpentine layout of the Gr/Pd film. The exposed graphene on both sides of the copper foil was etched using oxygen plasma. Next, the aluminum film was etched using a solution of potassium hydroxide (Step 2). Following the etching process, polymethylmethacrylate (PMMA) was deposited on the copper/Gr/Pd substrate by spin coating (Step 2). The copper foil was then etched in a solution of ammonium persulfate and the serpentine pattern of Gr/Pd/PMMA was transferred by a water bath onto a thin layer of stiff PDMS (1 MPa) (Step 3). Once the pattern of Gr/Pd/PMMA was transferred, the PMMA was dissolved in acetone and the PEDOT:PSS formulation was deposited in a serpentine pattern by spray coating through a different stencil with the same serpentine pattern (Step 4). After depositing the PEDOT:PSS formulation, the Gr/Pd/PEDOT:PSS sensor was addressed with copper wires attached by carbon paint (Step 5). The device was encapsulated by a layer of softer PDMS (0.15 MPa), deposited by spin coating the mixed prepolymer followed by thermal curing (Step 5).

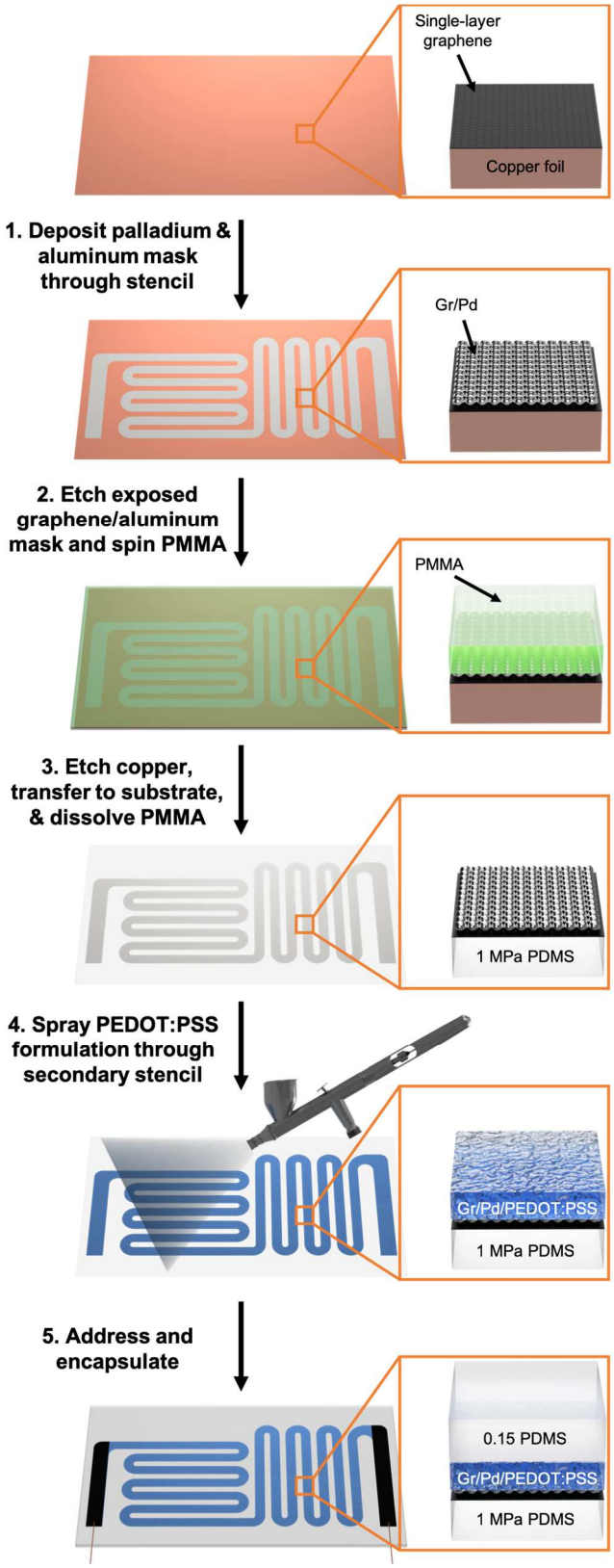

Figure 3.1. Schematic illustration of process used to fabricate the structured blend of Gr/Pd/PEDOT:PSS for use as a wearable strain sensor.

The piezoresistance of the palladium film on single-layer graphene is highly dependent on its nominal thickness (and thus its morphology and interconnectivity). A plot of the sheet resistance as a function of the nominal thickness of palladium deposited on top of single-layer graphene is shown in **Figure 3.2**. The sheet resistance of the palladium film on single-layer graphene exhibits a conspicuous increase from 0 nm (graphene only) to 2 nm film of palladium. This increase in resistance at the lowest nominal thicknesses could be attributable to the formation of Pd-C bonds on defect sites of graphene.[47] Palladium adatoms have also been observed to etch the graphene in the presence of oxygen during evaporation.[48] In the case of graphene transistors, the junction between the palladium electrodes and the graphene channel has also been shown to exhibit an increase in contact resistance at room temperature.[49] We attribute the decrease in sheet resistance for nominal thicknesses of palladium >2 nm to the formation of a sub-contiguous and eventually a continuous film of palladium at a thickness of 10 nm.

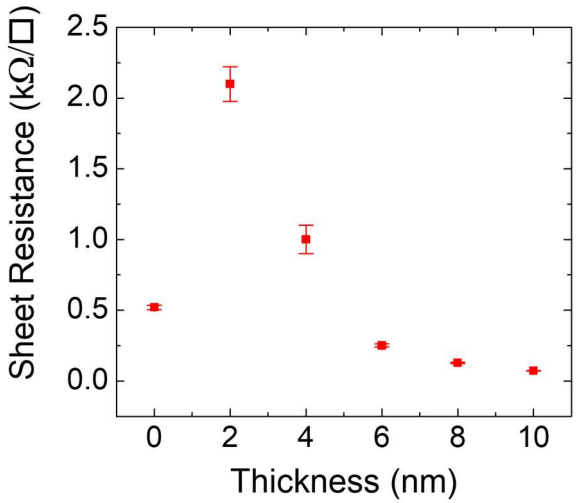

Figure 3.2. Electronic characterization of palladium films on single-layer graphene. Sheet resistance of discontinuous palladium films on single-layer graphene as a function of nominal thickness of palladium evaporated on top of the graphene layer.

The morphologies of the films at 2, 6, and 10 nm nominal thickness are shown in the atomic force microscope (AFM) and scanning electron microscope (SEM) images in **Figure 3.3**. At a low nominal thickness of palladium, the morphology of the film appears to have grains of a minute size (~ 5-10 nm diameter), with nanoscopic gaps between palladium grains (~ 10-15 nm). As more palladium is deposited, between 2 nm and 6 nm (4 nm palladium seen in **Figure A.0.2**), the grains appear to bridge together and the spacing between these bridged grains increases when compared to the thickness of 2 nm. This bridging continues at higher thicknesses, between 8 nm (seen in **Figure A.0.2)** and 10 nm, where the grains join towards a solid, visually contiguous film, with high surface coverage of the large palladium grains. The coverage seen in the microscopy images help explain the sheet resistance measurements for these respective nominal thicknesses, as the difference in sheet resistance lessens as more palladium is deposited, indicative of the formation of a bulk palladium film at 10 nm.

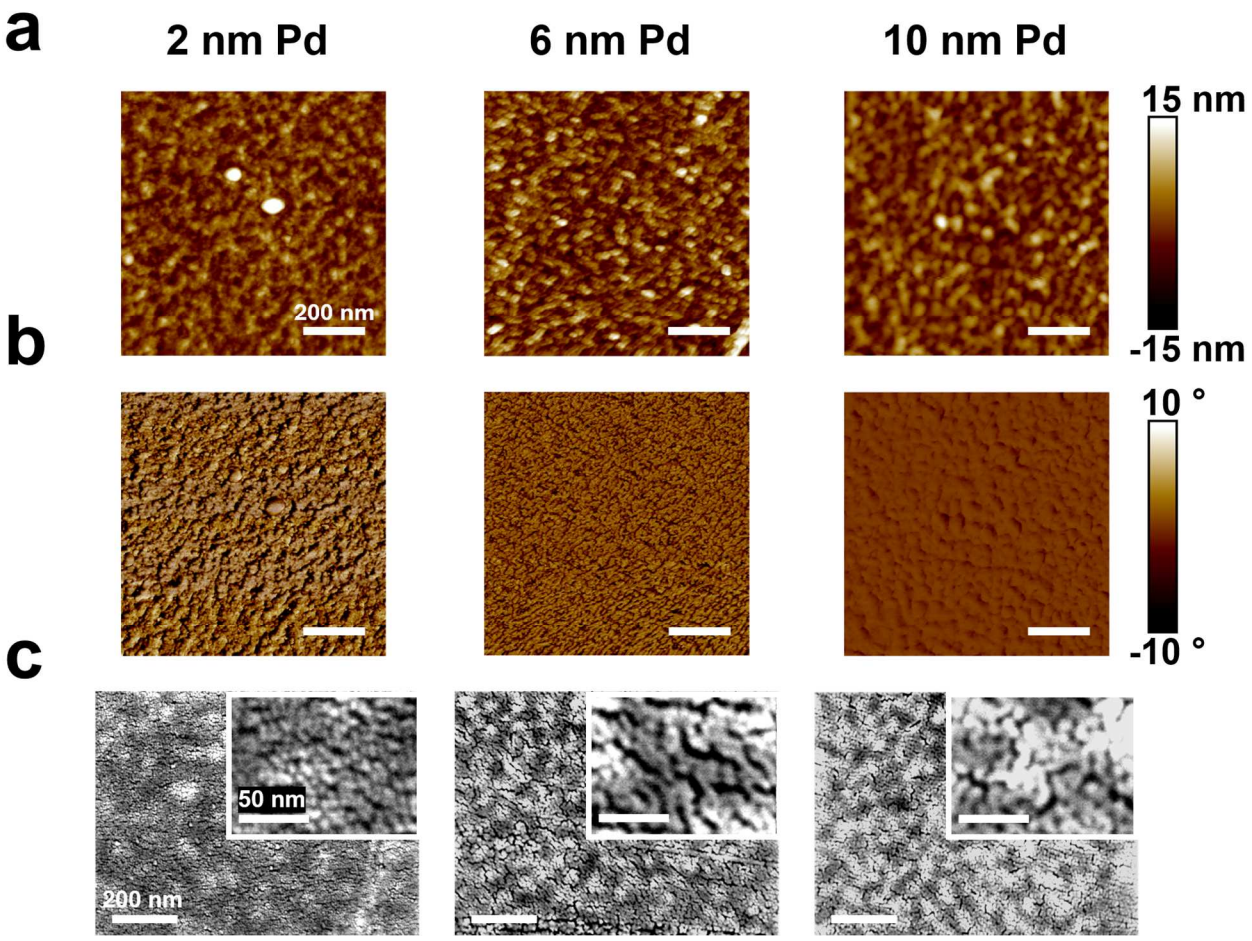

Figure 3.3. Morphological characterization of palladium films on single-layer graphene. Atomic force microscopy results depicting (a) height and (b) phase images depicting the palladium films of various thicknesses on single-layer graphene. (c) Scanning electron microscopy (SEM) images of palladium films of various nominal thicknesses on single-layer graphene.

The piezoresistance of the composite film is affected by the piezoresistive response of the individual components. **Figure 3.4** shows the normalized change in resistance experienced by the films on glass coverslips (thickness ~130 μm) when bent over a step edge of 13 μm, producing a tensile strain of 0.001%. These experiments were performed for five different materials: PEDOT:PSS "dough" (**3.4a**), 20 nm solid palladium film (**3.4b**), single-layer graphene (**4c**), graphene supporting 8 nm palladium film (**3.4d**), and the complete structured blend (**3.4e**). The PEDOT:PSS "dough" and the solid palladium film do not produce a piezoresistive signal at these low strains. In contrast, a clear piezoresistive response of single-layer graphene, ultrathin

palladium (8 nm), and the Gr/Pd/PEDOT:PSS composite film is seen in **Figure 3.4c-e**. Measurement of large and small deformations associated with physiological signals, however, requires the ability to be stretched while maintaining sensitivity at these higher strains.

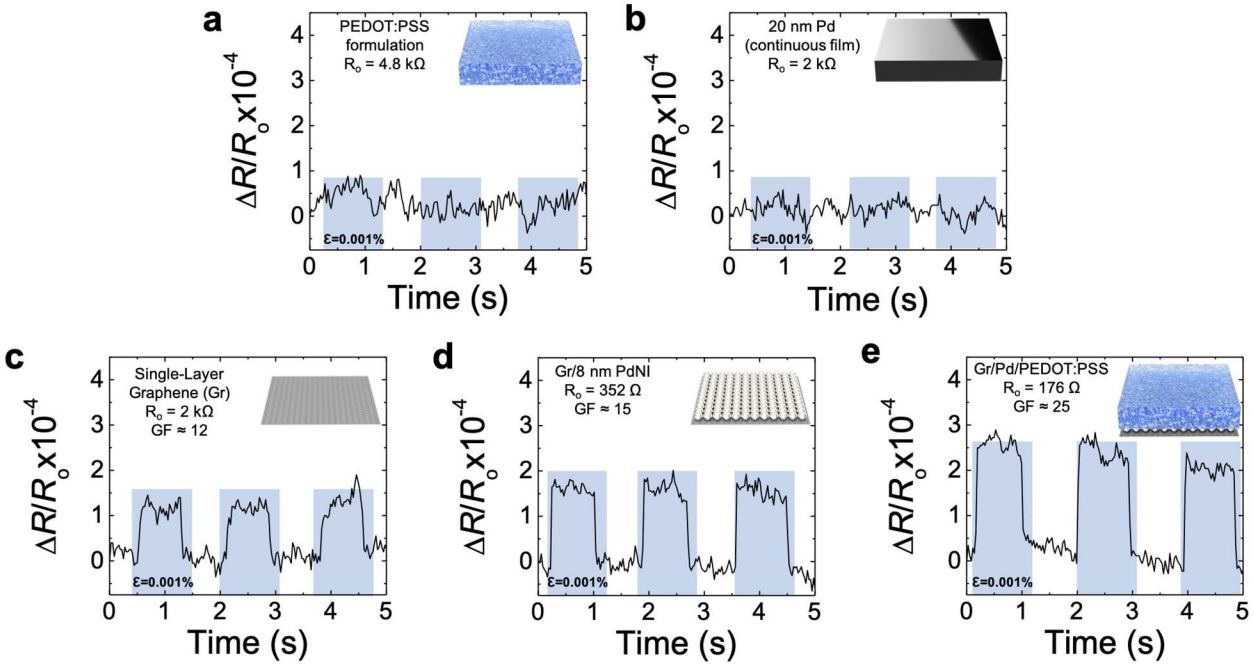

Figure 3.4. Piezoresistive characterization of the Gr/Pd/PEDOT:PSS material and its components on glass coverslips bent over a step edge of 13 μm (0.001% strain at the apex). Piezoresistive response of (a) pure PEDOT:PSS, (b) a 20 nm palladium film, (c) single-layer graphene, (d) single-layer graphene decorated with a granular palladium film of 8 nm nominal thickness, and (e) the complete composite of the Gr/Pd/PEDOT:PSS material.

After confirming the sensitivity of the structured blend to ultralow strains, the material was incorporated into a wearable device. In this application, the device needed to adhere conformally to skin, resist the formation of cracks in the sensor film, and have a wide dynamic range. The stability of the sensor on the skin depended on the stiffness of the elastomeric layers used for both the substrate (the layer in contact with the skin and supporting the graphene) and the encapsulant (the layer in contact with the PEDOT:PSS and the air). To minimize the mismatch in stiffness between the skin and the sensor, and thus improve adhesion to the skin, we

used PDMS with a relatively low modulus (0.15 MPa). (Softer PDMS also has an inherent viscoelastic tack that further improved adhesion to the skin.) To reduce the mismatch in modulus between the sensor layer and the encapsulant, and thus reduce the propensity for cracking, we used PDMS with a modulus of 1 MPa for the skin interface.[50,51] It should be noted that this reduction in modulus mismatch, which affects propensity in cracking, can lead to a reduction in the sensitivity (i.e. gauge factor) at higher strains, as seen in **Figure A.0.3**. Sensitivity to biaxial strains was afforded by patterning the sensor film into serpentines with a deposition mask.

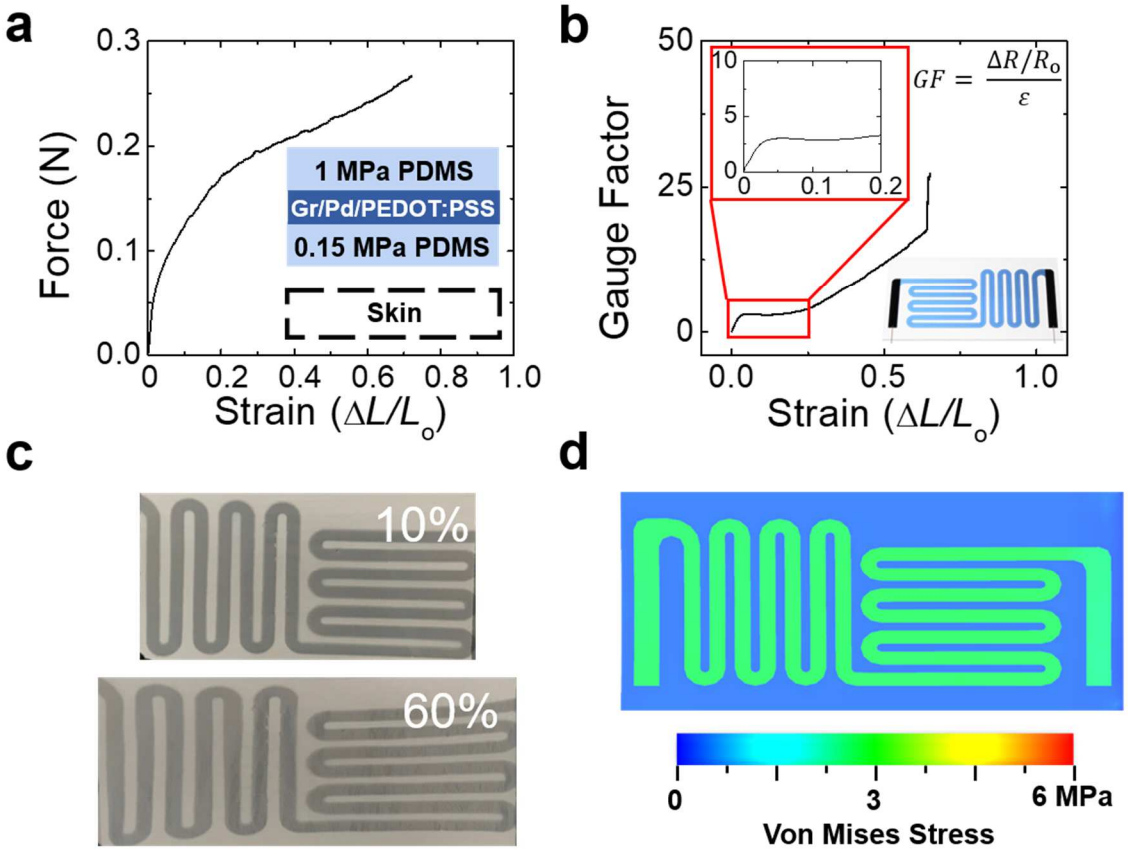

Figure 3.5. Characterization of Gr/Pd/PEDOT:PSS in a biaxial strain sensor pattern under uniaxial strain. The (b) gauge factor, (a) stress-strain curve, (c) photographic images, and (d) finite element analysis (FEA) of the Gr/Pd/PEDOT:PSS structured blend, with a 1 MPa PDMS encapsulant and a 0.15 MPa PDMS substrate.

The force-strain curve of the composite sensor is shown in **Figure 3.5a**. The behavior is dominated by the stiffest material in the device stack, in this case PDMS with a modulus of 1 MPa. The piezoresistive behavior and the photographic images of the rectangular Gr/Pd/PEDOT:PSS films with different encapsulants demonstrate that a use of a stiffer encapsulant reduces the formation of cracks and attenuates the gauge factor at higher strain regimes (**Figure A.0.3**). The combination of functions stemming from the sensor design enables increased signals when detecting smaller strain without risking signals saturation stemming from larger deformations.

We then tested if the sensor was capable of measuring both small and large strains simultaneously in a wearable device. Informed by our analysis, we placed the sensors under the left pectoral muscle of a healthy human subject (**Figure 3.6a**). The device is subject to stretch to approximately 10 - 15% strain when placed under the body, which can be well accommodated by the device, as indicated in the FEA simulation in **Figure 3.6b**. Additionally, these strains are well within the strain regime where the biaxial strain gauge has more sensitivity over the rectangular-shaped devices seen in **Figure A.0.3**. The device was capable of reliably detecting large human motions, such as wrist bends, seen in **Figure A.0.8**. While the sensor was able to detect the motions of the wrist, there were spikes in resistance stemming from the initiation of the wrist movement (bending or unbending). This can possibly be attributed to the viscoelastic response of the device when undergoing large strains at short timescales. The material is able to reliably perform and detect strains in the sensor device on non-smooth surfaces such as the human body. The ability to detect ultra-low strain signals and larger stretching deformations can be seen in **Figure 3.6c** and **Figure 3.6d**, as the sensor is able to detect heartbeats regardless of whether or not the human subject is breathing. This application highlights the complementarity

of sensitive nanoscale piezoresistors with conductive polymers. The ability to detect heartbeats and respiration simultaneously can enable the development of deployable sensors to potentially monitor and diagnose health disorders such as obstructive sleep apnea, whose diagnosis currently requires polysomnography using bulky equipment.[52–57]

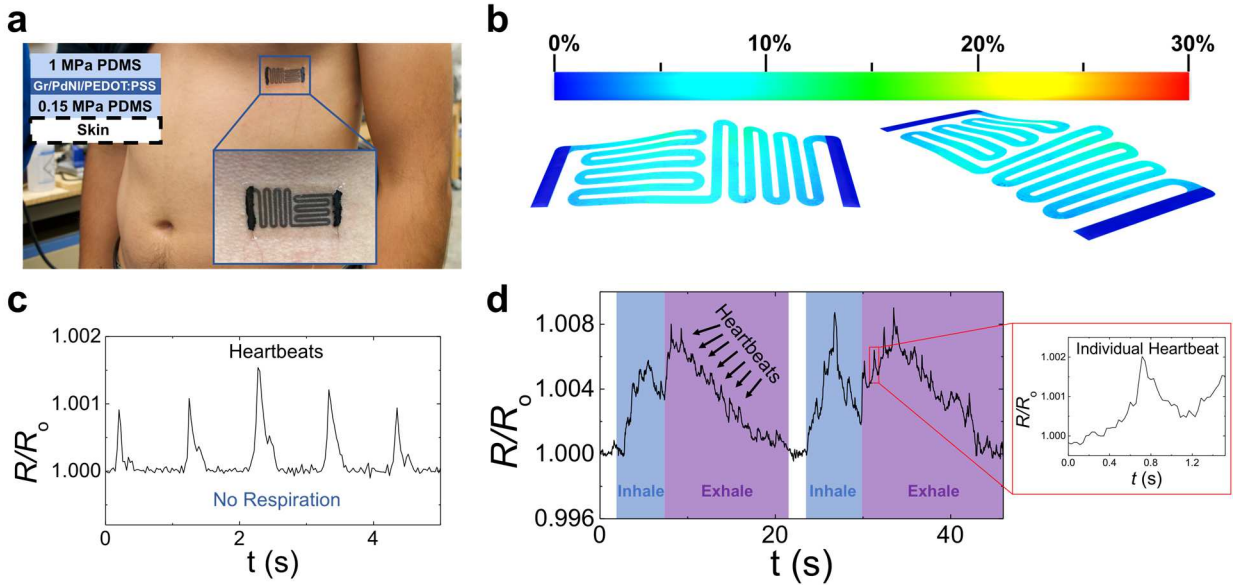

Figure 3.6. On-body testing of the Gr/Pd/PEDOT:PSS material with a 1 MPa PDMS encapsulant and a 0.15 MPa PDMS substrate, patterned into a serpentine strain gauge design. (a) Photograph and side view schematic of the wearable Gr/Pd/PEDOT:PSS sensor with a 1 MPa PDMS encapsulant and a 0.15 MPa PDMS substrate on the body of a human subject. (b) Finite element analysis (FEA) of the patterned Gr/Pd/PEDOT:PSS sensor as the material accommodates stress stemming from a normal force, simulating the force stemming from a heartbeat and/or respiration. Piezoresistive response of the patterned Gr/Pd/PEDOT:PSS sensor to simulations of (c) obstructive sleep apnea and (d) normal sleep by the human subject.

3.4. Conclusions

We have shown that a structured blend consisting of graphene, an ultrathin granular palladium film, and highly plasticized PEDOT:PSS can exhibit low detection limits, high sensitivities, and sufficient stretchability for wearable applications. In particular, the layer-by-layer architecture of Gr/Pd/PEDOT:PSS enables a multimodal piezoresistive response over

different strain regimes. This proof-of-concept application demonstrates the potential use of materials like Gr/Pd/PEDOT:PSS to remotely monitor patients who suffer from conditions like obstructive sleep apnea, suffered by 3–5% of the global population.[58,59] The data provided by a sensor like this can offer more actionable data to a user, such as a trained medical professional, and help them come to a decision that would otherwise not benefit the patient in time. In a larger context, materials like Gr/Pd/PEDOT:PSS represent potential materials-based solutions to real-world applications, where complex strains stemming from subtle and large strains need to be detected.

3.5 Methods

3.5.1. Fabrication of the sensor

Step 1: A nominal thickness of 8 nm of palladium nanoislands was deposited on top of single layer-graphene on copper foil (GrollTex, Inc.) using thermal evaporation (Orion System, AJA International) at a rate of 0.02 Å/s. A stainless steel stencil (Metal Etch Services, San Marcos, CA) was used to deposit the palladium nanoislands in a serpentine strain gauge shape, as shown in **Figure 3.1**. 50 nm of aluminum was deposited at 1.5 Å/s on top of the palladium by sputtering. The aluminum layer served as a mask to selectively etch off the graphene around the strain gauge pattern. Step 2: The graphene surrounding the design was then etched by oxygen plasma for 5 min. Afterward, the graphene on the back of the copper foil was etched off by oxygen plasma for 5 min. Similarly, the aluminum film was etched by submerging the sensor films into 0.025 M KOH in water (Fisher Scientific) for 1 min, leaving the serpentine strain gauge shape that comprises palladium nanoislands on a single layer of graphene. After etching the aluminum film, 4% PMMA (by mass, product no. 43982, Alfa Aesar) in anisole (Acros Organics) was deposited on top of the palladium nanoislands/graphene/copper by spin coating

(4000 rpm, 4000 rpm/s, 60 s). The film was then heated to 150 °C for 5 min to remove residual solvent. Step 3: The supporting copper foil was etched away in 0.05 g/mL ammonium persulfate (Acros Organics**)** in water. The film of Gr/Pd/PMMA was transferred out of the ammonium persulfate by adhering the edge of the film to a glass slide, lifting out the film from the ammonium persulfate, and plunging the glass slide into a water bath, releasing the film on the surface of the water.

A thin layer of 1 MPa PDMS was prepared by spin coating (2500 rpm, 2000 rpm/s, 5 min) a pre-cured mix (10 prepolymer : 1 curing agent by weight) onto a sheet of tattoo paper with a water- soluble layer (Laser Temporary Tattoo Kit, Papilio) followed by subsequent curing on a hotplate for 5 min at 150 □. The 1 MPa PDMS tattoo paper was then cut and mounted on a 7.62 cm × 5.08 cm glass slide using polyimide tape (Caplinq, Product No. PIT0.5S UT/25.4). The Gr/Pd/PMMA film was then transferred onto the 7.62 cm × 5.08 cm encapsulant of 1 MPa PDMS on tattoo paper by a water transfer technique, resulting in tattoo paper/PDMS/Gr/Pd/PMMA. Step 4: After transferring the obtaining the 1 MPa PDMS/Gr/Pd/PMMA architecture, the PMMA was dissolved in a hot acetone bath of around 40 □ for 1 min. The polyimide tape used to mount the tattoo paper/ 1 MPa PDMS sample prevented the acetone from seeping and prematurely soaking the tattoo paper. After the bath, the sample was immediately rinsed with IPA and placed under vacuum to dry. The PEDOT:PSS formulation was deposited by spray coating through a serpentine stencil. A bulk solution of the PEDOT:PSS formulation (92% wt PEDOT:PSS, 3% wt. Triton X-100, and 5% wt DMSO) was made and diluted in water (3 water: 1 PEDOT:PSS) to prevent clogging in the spray gun (200-9 Fine Head Gravity Feed Airbrush (G), Badger Air-Brush Co.).

The tattoo paper/1 MPa PDMS/Gr/Pd device was centered on a 14 cm diameter hotplate set to 150 □. The spray gun was fixed to a metal stand at a distance of 16.5 cm and at an angle of 60 degrees, both measured from sample to airbrush tip (see **Figure A.0.1**). The first step of the spraying routine consisted of six sprays (1 s duration each) that served as primer layers to improve the PEDOT:PSS formulation's wettability. The deposition of the primer layers was followed by four 10-second spray intervals, and eight 20-second spray intervals (200 s duration, total deposition time: 206 s). Between each spray interval, the sample was rotated by 90 degrees, the stencil was lifted from the PMMA/Gr/Pd/ PEDOT:PSS surface, and the PEDOT dough was allowed to dry for 1-minute. Step 5: After spraying the PEDOT:PSS formulation, the sensor was addressed with copper wire; carbon paint was painted on the contact area (DAG-T-502, Ted Pella, Inc.) and left to dry in a fume hood. Finally, the device was encapsulated by spin coating 0.15 MPa PDMS [30 prepolymer: 1 curing agent by weight] (4000 rpm, 4000 rpm/s, 60 s), and curing the PDMS for 5 minutes at 150□ on a hotplate, resulting in the finished device (tattoo paper/1 MPa PDMS/Gr/Pd/PEDOT:PSS/0.15 MPa PDMS).

3.5.2. Cantilever experiment

For the cantilever strain experiment, where the materials were strained to 0.001% (seen in **Figure 3.2**), a 1 cm × 0.5 cm film of the respective materials materials were transferred and/or deposited on the center of a 2.54 cm × 2.54 cm glass cover slip (Sail Brand, 22 mm × 22 mm, 130-170 μm thickness). The device on the coverslip was then partially suspended, clamped with a 1.27 cm overlap, over a step edge of ~13 μm, made by adhering polyimide tape (Caplinq, Product No. PIT0.5S UT/25.4) to a 7.62 cm × 5.08 cm glass slide. The tensile strain applied to the sensor device was calculated by FEA analysis of our experimental setup, previously published by our group.[2]

3.5.2. Pull Test of the Gr/Pd/PEDOT:PSS sensor device

Pull test measurements where conducted using a Keithley 2611B Source Meter running a custom LABView program and a Mark-10 Force Gauge (MS-05). The sensor sample was cut out of the 7.62 cm × 5.08 cm glass slide. The tattoo paper backing was removed with a wet Kimwipe, and the sample was transferred to the grips of the force gauge and addressed to the source meter. The sample was pulled at a speed of 1 mm/sec while running the source meter and the force gauge simultaneously.

3.5.2. FEA Modeling

All finite element analysis models were done using Fusion360 (Autodesk). The film thicknesses were scaled by 10 in order to prevent failure of the simulation. A load of 6 N was applied in all cases (uniaxial strain and strain normal to the device plane).

3.5.2. On Body Experiments

On Body measurements where conducted using a Keithley 2611B running LABView. The sample was cut out of the 7.62 cm × 5.08 cm glass slide. The sensor was placed on the ribcage, slightly under the chest, while the subject was lying down. The tattoo paper backing was removed with a wet Kimwipe, which dissolved the water-soluble film on the tattoo paper. The wires of the sensor device were addressed to the Keithley 2400 sourcemeter, and the data was obtained while the healthy subject breathed in the supine position.

Acknowledgements

This work was supported by the National Institutes of Health Director's New Innovator Award, Grant No. 1DP2EB022358. J.R. and D.R. acknowledge support provided by the National Science Foundation Graduate Research Fellowship Program under Grant No. DGE-1144086.

Additional support was provided by the Center for Wearable Sensors in the Jacobs School of Engineering at the University of California San Diego, and member companies Qualcomm, Sabic, Cubic, Dexcom, Corning, Honda, Samsung, and Sony. A.C. acknowledges support from the Initiative for Maximizing Student Development (IMSD) program, supported by the National Institute of General Medical Sciences under Grant No. R25GM083275. This work was performed in part at the San Diego Nanotechnology Infrastructure (SDNI), a member of the National Nanotechnology Coordinated Infrastructure, which is supported by the National Science Foundation (Grant No. ECCS-1542148).

Chapter 3, in full, is a reprint of the material as it appears in *ACS Appl. Nano Mater.* **2019**, *2* (4), 2222–2229. American Chemical Society, 2019. Julian Ramírez, Daniel Rodriquez, Armando D. Urbina, Anne M. Cardenas, and Darren J. Lipomi. The dissertation author was the primary investigator and author of this paper.

References

(1) Oh, J. Y.; Kim, S.; Baik, H.-K.; Jeong, U. Conducting Polymer Dough for Deformable Electronics. *Adv. Mater.* **2016**, *28* (22), 4455–4461.

(2) Zaretski, A. V; Root, S. E.; Savchenko, A.; Molokanova, E.; Printz, A. D.; Jibril, L.; Arya, G.; Mercola, M.; Lipomi, D. J. Metallic Nanoislands on Graphene as Highly Sensitive Transducers of Mechanical, Biological, and Optical Signals. *Nano Lett.* **2016**, *16* (2), 1375–1380.

(3) Trung, T. Q.; Lee, N. E. Flexible and Stretchable Physical Sensor Integrated Platforms for Wearable Human-Activity Monitoringand Personal Healthcare. *Adv. Mater.* **2016**, *28* (22), 4338–4372.

(4) Kang, I.; Schulz, M. J.; Kim, J. H.; Shanov, V.; Shi, D. A Carbon Nanotube Strain Sensor for Structural Health Monitoring. *Smart Mater. Struct.* **2006**, *15* (3), 737–748.

(5) Senesky, D. G.; Jamshidi, B.; Pisano, a. P. Harsh Environment Silicon Carbide Sensors for Health and Performance Monitoring of Aerospace Systems: A Review. *IEEE Sens. J.* **2009**, *9* (11), 1472–1478.

(6) Lynch, J. P. A Summary Review of Wireless Sensors and Sensor Networks for Structural Health Monitoring. *Shock Vib. Dig.* **2006**, *38* (2), 91–128.

(7) Kim, D. H.; Lu, N.; Ma, R.; Kim, Y. S.; Kim, R. H.; Wang, S.; Wu, J.; Won, S. M.; Tao, H.; Islam, A.; Yu, K. J.; Kim, T. I.; Chowdhury, R.; Ying, M.; Xu, L.; Li, M.; Chung, H. J.; Keum, H.; McCormick, M.; Liu, P.; Zhang, Y. W.; Omenetto, F. G.; Huang, Y.; Coleman, T.; Rogers, J. A. Epidermal Electronics. *Science (80-.).* **2011**.

(8) Kang, D. Y.; Kim, Y. S.; Ornelas, G.; Sinha, M.; Naidu, K.; Coleman, T. P. Scalable Microfabrication Procedures for Adhesive-Integrated Flexible and Stretchable Electronic Sensors. *Sensors (Switzerland)* **2015**, *15* (9), 23459–23476.

(9) Kim, Y. S.; Lu, J.; Shih, B.; Gharibans, A.; Zou, Z.; Matsuno, K.; Aguilera, R.; Han, Y.; Meek, A.; Xiao, J.; Tolley, M. T.; Coleman, T. P. Scalable Manufacturing of Solderable and Stretchable Physiologic Sensing Systems. *Adv. Mater.* **2017**, *29* (39), 1–11.

(10) Li, T.; Huang, Z.; Suo, Z.; Lacour, S. P.; Wagner, S. Stretchability of Thin Metal Films on Elastomer Substrates. *Appl. Phys. Lett.* **2004**, *85* (16), 3435–3437.

(11) Hu, N.; Karube, Y.; Yan, C.; Masuda, Z.; Fukunaga, H. Tunneling Effect in a Polymer/Carbon Nanotube Nanocomposite Strain Sensor. *Acta Mater.* **2008**, *56* (13), 2929–2936.

(12) Bae, S. H.; Lee, Y.; Sharma, B. K.; Lee, H. J.; Kim, J. H.; Ahn, J. H. Graphene-Based Transparent Strain Sensor. *Carbon* **2013**, *51* (1), 236–242.

(13) Zhao, J.; He, C.; Yang, R.; Shi, Z.; Cheng, M.; Yang, W.; Xie, G.; Wang, D.; Shi, D.; Zhang, G. Ultra-Sensitive Strain Sensors Based on Piezoresistive Nanographene Films. *Appl. Phys. Lett.* **2012**, *101* (6), 063112.

(14) Wang, Y.; Wang, L.; Yang, T.; Li, X.; Zang, X.; Zhu, M.; Wang, K.; Wu, D.; Zhu, H. Wearable and Highly Sensitive Graphene Strain Sensors for Human Motion Monitoring. *Adv. Funct. Mater.* **2014**, *24* (29), 4666–4670.

(15) Pereira, V. M.; Castro Neto, A. H.; Peres, N. M. R. Tight-Binding Approach to Uniaxial Strain in Graphene. *Phys. Rev. B - Condens. Matter Mater. Phys.* **2009**, *80* (4), 1–8.

(16) Ni, Z. H.; Yu, T.; Lu, Y. H.; Wang, Y. Y.; Feng, Y. P.; Shen, Z. X. Uniaxial Strain on Graphene : Raman Spectroscopy Study and Band Gap Opening. *ACS Nano* **2008**, *2* (11), 2301–2305.

(17) Smith, A. D.; Niklaus, F.; Paussa, A.; Schröder, S.; Fischer, A. C.; Sterner, M.; Wagner, S.; Vaziri, S.; Forsberg, F.; Esseni, D.; Östling, M.; Lemme, M. C. Piezoresistive Properties of Suspended Graphene Membranes under Uniaxial and Biaxial Strain in Nanoelectromechanical Pressure Sensors. *ACS Nano* **2016**, *10* (11), 9879–9886.

(18) Smith, A. D.; Niklaus, F.; Paussa, A.; Vaziri, S.; Fischer, A. C.; Sterner, M.; Forsberg, F.; Delin, A.; Esseni, D.; Palestri, P.; Östling, M.; Lemme, M. C. Electromechanical Piezoresistive Sensing in Suspended Graphene Membranes. *Nano Lett.* **2013**, *13* (7), 3237–3242.

(19) Yang, T.; Li, X.; Jiang, X.; Lin, S.; Lao, J.; Shi, J.; Zhen, Z.; Li, Z.; Zhu, H. Structural Engineering of Gold Thin Films with Channel Cracks for Ultrasensitive Strain Sensing. *Mater. Horizons* **2016**, *3* (3), 248–255.

(20) Kang, D.; Pikhitsa, P. V.; Choi, Y. W.; Lee, C.; Shin, S. S.; Piao, L.; Park, B.; Suh, K. Y.; Kim, T. Il; Choi, M. Ultrasensitive Mechanical Crack-Based Sensor Inspired by the Spider Sensory System. *Nature* **2014**, *516* (7530), 222–226.

(21) Park, B.; Kim, J.; Kang, D.; Jeong, C.; Kim, K. S.; Kim, J. U.; Yoo, P. J.; Kim, T. Dramatically Enhanced Mechanosensitivity and Signal-to-Noise Ratio of Nanoscale Crack-Based Sensors: Effect of Crack Depth. *Adv. Mater.* **2016**, *28* (37), 8130–8137.

(22) Cao, L.; Kim, T. S.; Mantell, S. C.; Polla, D. L. Simulation and Fabrication of Piezoresistive Membrane Type MEMS Strain Sensors. *Sensors Actuators, A Phys.* **2000**, *80* (3), 273–279.

(23) Mohammed, A. A. S.; Moussa, W. A.; Lou, E. Development and Experimental Evaluation of a Novel Piezoresistive MEMS Strain Sensor. *IEEE Sens. J.* **2011**, *11* (10), 2220–2232.

(24) Hautamaki, C.; Zurn, S.; Mantell, S. C.; Polla, D. L. Experimental Evaluation of MEMS Strain Sensors Embedded in Composites. *J. Microelectromechanical Syst.* **1999**, *8* (3), 272–279.

(25) Seyedin, M. Z.; Razal, J. M.; Innis, P. C.; Wallace, G. G. Strain-Responsive Polyurethane/PEDOT:PSS Elastomeric Composite Fibers with High Electrical Conductivity. *Adv. Funct. Mater.* **2014**, *24* (20), 2957–2966.

(26) Cheng, Y.; Wang, R.; Chan, K. H.; Lu, X.; Sun, J.; Ho, G. W. A Biomimetic Conductive Tendril for Ultrastretchable and Integratable Electronics, Muscles, and Sensors. *ACS Nano* **2018**, *12* (4), 3898–3907.

(27) Lipomi, D. J.; Vosgueritchian, M.; Tee, B. C. K.; Hellstrom, S. L.; Lee, J. A.; Fox, C. H.; Bao, Z. Skin-like Pressure and Strain Sensors Based on Transparent Elastic Films of Carbon Nanotubes. *Nat. Nanotechnol.* **2011**, *6* (12), 788–792.

(28) Jing, X.; Mi, H.; Lin, Y.; Enriquez, E.; Peng, X.; Turng, L. Highly Stretchable and Biocompatible Strain Sensors Based on Mussel-Inspired Super-Adhesive Self-Healing Hydrogels for Human Motion Monitoring. *ACS Appl. Mater. Interfaces* **2018**, *10*, 20897–20909.

(29) Yamada, T.; Hayamizu, Y.; Yamamoto, Y.; Yomogida, Y.; Izadi-Najafabadi, A.; Futaba,

D. N.; Hata, K. A Stretchable Carbon Nanotube Strain Sensor for Human-Motion Detection. *Nat. Nanotechnol.* **2011**, *6* (5), 296–301.

(30) Roh, E.; Hwang, B. U.; Kim, D.; Kim, B. Y.; Lee, N. E. Stretchable, Transparent, Ultrasensitive, and Patchable Strain Sensor for Human-Machine Interfaces Comprising a Nanohybrid of Carbon Nanotubes and Conductive Elastomers. *ACS Nano* **2015**, *9* (6), 6252–6261.

(31) Hwang, B. U.; Lee, J. H.; Trung, T. Q.; Roh, E.; Kim, D. Il; Kim, S. W.; Lee, N. E. Transparent Stretchable Self-Powered Patchable Sensor Platform with Ultrasensitive Recognition of Human Activities. *ACS Nano* **2015**, *9* (9), 8801–8810.

(32) Amjadi, M.; Kyung, K. U.; Park, I.; Sitti, M. Stretchable, Skin-Mountable, and Wearable Strain Sensors and Their Potential Applications: A Review. *Adv. Funct. Mater.* **2016**, *26* (11), 1678–1698.

(33) Wu, H.; Liu, Q.; Chen, H.; Shi, G.; Li, C. Fibrous Strain Sensor with Ultra-Sensitivity, Wide Sensing Range, and Large Linearity for Full-Range Detection of Human Motion. *Nanoscale* **2018**, *10* (37), 17512–17519.

(34) Cheng, Y.; Wang, R.; Sun, J.; Gao, L. A Stretchable and Highly Sensitive Graphene-Based Fiber for Sensing Tensile Strain, Bending, and Torsion. *Adv. Mater.* **2015**, *27* (45), 7365–7371.

(35) Park, J. J.; Hyun, W. J.; Mun, S. C.; Park, Y. T.; Park, O. O. Highly Stretchable and Wearable Graphene Strain Sensors with Controllable Sensitivity for Human Motion Monitoring. *ACS Appl. Mater. Interfaces* **2015**, *7* (11), 6317–6324.

(36) Yan, C.; Wang, J.; Kang, W.; Cui, M.; Wang, X.; Foo, C. Y.; Chee, K. J.; Lee, P. S. Highly Stretchable Piezoresistive Graphene-Nanocellulose Nanopaper for Strain Sensors. *Adv. Mater.* **2014**, *26* (13), 2022–2027.

(37) Gong, S.; Lai, D. T. H.; Su, B.; Si, K. J.; Ma, Z.; Yap, L. W.; Guo, P. Highly Stretchy Black Gold E-Skin Nanopatches as Highly Sensitive Wearable Biomedical Sensors. *Adv. Electron. Mater.* **2015**, 1–7.

(38) Gong, S.; Lai, D. T. H.; Wang, Y.; Yap, L. W.; Si, K. J.; Shi, Q.; Jason, N. N.; Sridhar, T.; Uddin, H.; Cheng, W. Tattoolike Polyaniline Microparticle-Doped Gold Nanowire Patches as Highly Durable Wearable Sensors. *ACS Appl. Mater. Interfaces* **2015**, *7* (35), 19700–19708.

(39) Ramírez, J.; Rodriquez, D.; Qiao, F.; Warchall, J.; Rye, J.; Aklile, E.; S.-C. Chiang, A.; Marin, B. C.; Mercier, P. P.; Cheng, C. K.; Hutcheson, K. A.; Shinn, E. H.; Lipomi, D. J. Metallic Nanoislands on Graphene for Monitoring Swallowing Activity in Head and Neck Cancer Patients. *ACS Nano* **2018**, *12* (6), 5913–5922.

(40) Dhong, C.; Edmunds, S. J.; Ramírez, J.; Kayser, L. V.; Chen, F.; Jokerst, J. V.; Lipomi, D. J. Optics-Free, Non-Contact Measurements of Fluids, Bubbles, and Particles in Microchannels Using Metallic Nano-Islands on Graphene. *Nano Lett.* **2018**, *18* (8), 5306–5311.

(41) Bae, S.; Kim, H.; Lee, Y.; Xu, X.; Park, J. S.; Zheng, Y.; Balakrishnan, J.; Lei, T.; Ri Kim, H.; Song, Y. Il; Kim, Y. J.; Kim, K. S.; Özyilmaz, B.; Ahn, J. H.; Hong, B. H.; Iijima, S. Roll-to-Roll Production of 30-Inch Graphene Films for Transparent Electrodes. *Nat. Nanotechnol.* **2010**, *5* (8), 574–578.

(42) Marin, B. C.; Root, S. E.; Urbina, A. D.; Aklile, E.; Miller, R.; Zaretski, A. V.; Lipomi, D. J. Graphene-Metal Composite Sensors with Near-Zero Temperature Coefficient of Resistance. *ACS Omega* **2017**, *2* (2), 626–630.

(43) Marin, B. C.; Liu, J.; Aklile, E.; Urbina, A. D.; Chiang, A. S. C.; Lawrence, N.; Chen, S.; Lipomi, D. J. SERS-Enhanced Piezoplasmonic Graphene Composite for Biological and Structural Strain Mapping. *Nanoscale* **2017**, *9* (3), 1292–1298.

(44) Savagatrup, S.; Chan, E.; Renteria-Garcia, S. M.; Printz, A. D.; Zaretski, A. V.; O'Connor, T. F.; Rodriquez, D.; Valle, E.; Lipomi, D. J. Plasticization of PEDOT:PSS by Common Additives for Mechanically Robust Organic Solar Cells and Wearable Sensors. *Adv. Funct. Mater.* **2015**, *25* (3), 427–436.

(45) Vosgueritchian, M.; Lipomi, D. J.; Bao, Z. Highly Conductive and Transparent PEDOT:PSS Films with a Fluorosurfactant for Stretchable and Flexible Transparent Electrodes. *Adv. Funct. Mater.* **2012**, *22* (2), 421–428.

(46) Dimitriev, O. P.; Grinko, D. A.; Noskov, Y. V.; Ogurtsov, N. A.; Pud, A. A. PEDOT:PSS Films-Effect of Organic Solvent Additives and Annealing on the Film Conductivity. *Synth. Met.* **2009**, *159* (21–22), 2237–2239.

(47) Gong, C.; McDonnell, S.; Qin, X.; Azcatl, A.; Dong, H.; Chabal, Y. J.; Cho, K.; Wallace, R. M. Realistic Metal-Graphene Contact Structures. *ACS Nano* **2014**, *8* (1), 642–649.

(48) Ramasse, Q. M.; Zan, R.; Bangert, U.; Boukhvalov, D. W.; Son, Y. W.; Novoselov, K. S. Direct Experimental Evidence of Metal-Mediated Etching of Suspended Graphene. *ACS Nano* **2012**, *6* (5), 4063–4071.

(49) Xia, F.; Perebeinos, V.; Lin, Y. M.; Wu, Y.; Avouris, P. The Origins and Limits of Metal-Graphene Junction Resistance. *Nat. Nanotechnol.* **2011**, *6* (3), 179–184.

(50) Rodriquez, D.; Kim, J.-H.; Root, S. E.; Fei, Z.; Boufflet, P.; Heeney, M.; Kim, T.-S.; Lipomi, D. J. Comparison of Methods for Determining the Mechanical Properties of Semiconducting Polymer Films for Stretchable Electronics. *ACS Appl. Mater. Interfaces* **2017**, *9* (10), 8855–8862.

(51) Alkhadra, M. A.; Root, S. E.; Hilby, K. M.; Rodriquez, D.; Sugiyama, F.; Lipomi, D. J. Quantifying the Fracture Behavior of Brittle and Ductile Thin Films of Semiconducting Polymers. *Chem. Mater.* **2017**, *29* (23), 10139–10149.

(52) Gao, X.; Zhang, J.-J.; Ge, Z.; Jiang, X.-M.; Xiao, P.-X.; Tian, N.-L.; Kan, J.; Lee, C.; Chen, S. Obstructive Sleep Apnea Affects the Clinical Outcomes of Patients Undergoing Percutaneous Coronary Intervention. *Patient Prefer. Adherence* **2016**, 871.

(53) Gami, A. S.; Olson, E. J.; Shen, W. K.; Wright, R. S.; Ballman, K. V.; Hodge, D. O.; Herges, R. M.; Howard, D. E.; Somers, V. K. Obstructive Sleep Apnea and the Risk of Sudden Cardiac Death: A Longitudinal Study of 10,701 Adults. *J. Am. Coll. Cardiol.* **2013**, *62* (7), 610–616.

(54) Pedrosa, R. P.; Drager, L. F.; Gonzaga, C. C.; Sousa, M. G.; De Paula, L. K. G.; Amaro, A. C. S.; Amodeo, C.; Bortolotto, L. A.; Krieger, E. M.; Bradley, T. D.; Lorenzi-Filho, G. Obstructive Sleep Apnea: The Most Common Secondary Cause of Hypertension Associated with Resistant Hypertension. *Hypertension* **2011**, *58* (5), 811–817.

(55) Gottlieb, D. J.; Yenokyan, G.; Newman, A. B.; O'Connor, G. T.; Punjabi, N. M.; Quan, S. F.; Redline, S.; Resnick, H. E.; Tong, E. K.; Diener-West, M.; Shahar, E. Prospective Study of Obstructive Sleep Apnea and Incident Coronary Heart Disease and Heart Failure: The Sleep Heart Health Study. *Circulation* **2010**, *122* (4), 352–360.

(56) Ferré, A.; Vila, J.; Jurado, M. J.; Arcalis, N.; Camps, J.; Cambrodi, R.; Romero, O. Sleep-Related Painful Erections Associated with Obstructive Sleep Apnea Syndrome. *Arch. Sex. Behav.* **2012**, *41* (4), 1059–1063.

(57) Abouda, M.; Jomni, T.; Yangui, F.; Charfi, M. R.; Arnulf, I. Sleep-Related Painful Erections in a Patient With Obstructive Sleep Apnea Syndrome. *Arch. Sex. Behav.* **2016**, *45* (1), 241–245.

(58) Franklin, K. A.; Lindberg, E. Obstructive Sleep Apnea Is a Common Disorder in the Population-A Review on the Epidemiology of Sleep Apnea. *J. Thorac. Dis.* **2015**, *7* (8), 1311–1322.

(59) Punjabi, N. M. The Epidemiology of Adult Obstructive Sleep Apnea. *Proc. Am. Thorac. Soc.* **2008**, *5* (2), 136–143.

Chapter 4 Exploring the Limits of Sensitivity for Strain Gauges of Graphene and Hexagonal Boron Nitride Decorated with Metallic Nanoislands

Abstract

The purpose of this work is to clarify the mechanism of piezoresistance in a class of ultra-sensitive strain gauges based on metallic films on 2D substrates ("2D/M" films). The metals used are gold or palladium deposited as ultrathin films (≤16 nm). These films transition from a regime of subcontiguous growth to a percolated morphology with increasing nominal thickness. The 2D substrates are either single-layer graphene or hexagonal boron nitride (hBN). By using either a conductor (graphene) or an insulator (hBN), it is possible to de-couple the relative contributions of the metal and the 2D substrate from the overall piezoresistance of the composite structure. Here, we use a combination of measurements including electron microscopy, automated image analysis, temperature-dependent conductivity, and measurements of gauge factor of the films as they are bent over a 1-μm step edge (0.0001% or 1 ppm). Our observations are enumerated as follows: (1) of the four permutations of metal and 2D substrate, all combinations except hBN/Au are able to resolve 1 ppm strain (considered extraordinary for strain gauges) at some threshold thickness of metal; (2) for non-contiguous (i.e., unpercolated) films of metal on hBN, changes in resistance for these small step strains cannot be detected; (3) for percolated films on hBN, changes in resistance upon strain can be resolved only for palladium and not for gold; (4) graphene does not exhibit detectable changes in resistance when subjected to step strains of either 1 or 10 ppm, but does so upon the deposition of any amount of gold or palladium, even for nominal thicknesses below the threshold for percolation. Our observations reveal unexpected complexity in the properties of these simple composite materials, and ways in which these materials might be combined to exhibit even greater sensitivity.

4.1. Introduction

Strain gauges are ubiquitous components of instruments used in research and technology, from wearable sensors,[1] to structural health monitors.[2] The majority of commercial strain gauges are based on solid, unstructured materials—e.g., metallic foils and semiconductor slabs—which undergo a change in electrical resistance when mechanically deformed.[3] The resistance of an isotropic conductor can be defined as:

$$R = \frac{A\rho}{L} \tag{1}$$

Where A is the cross-sectional area, ρ is the resistivity and L is the length of the conductor. In the case of solid metals or alloys under tensile strain, the variation in resistance can primarily be attributed to a transformation in the geometry of the conductor: elongation of the stretched axis and compression of the transverse axis (i.e., the normal Poisson effect).[4,5] Devices exploiting this effect are limited to a maximum gauge factor of 2.[5] This limitation has led to the development of strain gauges based on semiconductors, in which the variation in the resistance is due to a transformation in the geometry and a change in the resistivity—i.e., "piezoresistance."[6–8]

For strain gauges based on semiconductors, the change in the resistivity is due to shifts in the electronic band structure.[9] The most common type of semiconductor devices are microelectromechanical systems (MEMS) strain gauges based on silicon. They can resolve strains of ~ 0.01% (100 microstrains or 100 ppm strain) with gauge factors ranging from 20 to 40, but are used only in applications where the total strain is ≤0.3% due to the rigidity of crystalline semiconductors.[10–12]

To overcome these challenges, a variety of strain gauges based on nanostructured materials have been developed.[4,13–16] For example, our laboratory has introduced the use of single-layer graphene decorated with ultrathin metallic films laminated to flexible or stretchable

substrates.[16] On graphene, metals deposited with low nominal thicknesses (e.g., less than approximately 10 nm) adopt a highly granular structure ("nanoislands"). These metal-graphene composite gauges exhibit a large piezoresistive response and, when paired with the proper instrumentation, are capable of resolving strains on the order of 0.001% (10 ppm). Moreover, these sensors can be tuned to exhibit a near-zero temperature coefficient of resistance (TCR) with the proper balance of metal (which has a positive TCR) on graphene (which has a negative TCR).[17] The mechanism responsible for the piezoresistance of these composite films has not been straightforward to establish, largely because graphene,[1,18,19] metallic films,[5,20,21] and closely spaced metallic particles[22–24] have been shown to exhibit sensitivity to strain when used alone (though usually in response to strains larger than the ones explored here). It was our belief that we could obtain a refined understanding of the piezoresistance by systematically changing the metal, the nominal thickness (and thus the interconnectivity of the nanoislands), and the identity of the 2D substrate (i.e., graphene or hexagonal boron nitride). While the morphologies of metallic films on graphene and hBN have been the subject of previous work,[25–27] here, our goal was to use these 2D substrates for their conductive and insulating properties in order to compare the difference in piezoresistance performance of various 2D/M films. With this empirical comparison, we sought to narrow the range of possible mechanisms which could account for the piezoresistance of the composite films. This investigation of the ways in which the structure influences the electrical performance would enable the fabrication of strain gauges with even greater sensitivity, the ability to resolve even lower strains, and greater reproducibility than is now possible.

4.2. Background

4.2.1. Figures of merit.

The tensile or compressive deformation of a strain gauge is referred to as the engineering strain, which is the change in length of the strained axis divided by its length at equilibrium. Engineering strain (hereafter strain) is expressed as either a percent or a fraction (0.01 = 1% = 10,000 ppm = 10,000 microstrains). In this paper, the performance of a strain gauge is quantified using two interrelated metrics: gauge factor (i.e., "sensitivity"), and lowest resolvable strain (the resolution where the initial state of the specimen is at mechanical equilibrium).

The relative change in the electrical resistance of a material due to applied strain is quantified by the gauge factor (GF):

$$GF = \frac{\Delta R/R_o}{\varepsilon} \tag{2}$$

where ΔR is the change in the resistance under engineering strain, ε, with respect to the initial resistance at mechanical equilibrium, R_o. For an isotropic conductor that exhibits no piezoresistive response, the gauge factor can be expressed solely in terms of how the geometry of the specimen is transformed with applied strain[6]:

$$GF_{np} = 1 + 2\nu \tag{3}$$

where, ν is the material's Poisson ratio. Given that the Poisson ratio must be less than 0.5, the maximum possible gauge factor for non-piezoresistive materials is two.[28] However, some materials can exhibit gauge factors much greater than two. This increase is accounted for by adding a term[6]:

$$GF_p = 1 + 2\nu + \frac{\Delta\rho/\rho}{\varepsilon} \tag{4}$$

This term is called the piezoresistive coefficient; it describes the relative strain-induced change in the resistivity of the material. The gauge factor can be thought of as describing the "sensitivity" of the electrical resistance of a strain gauge to deformation. When the gauge factor

is greater than two, piezoresistance must be a contributing factor. While the gauge factor captures how responsive a material is to strain, it does not describe the range of strain over which the piezoresistive response is reproducible, i.e., the dynamic range. The gauge factor need not be constant over this range; for nanoparticle-based strain gauges, it usually is not. The minimum deformation necessary to create a signal that is differentiable from the noise is called the "resolution." Given that the resolution is dependent on the noise, the resolution is also dependent on the apparatus used to measure the resistance, and thus resolution—and hence gauge factor—is a system-level quantity. From an experimental standpoint, it is important to establish a robust contact between the wires used for measurement and the sensor film, as a poor contact can lead to large variation under strain and provide sensitivity values that are misleading. In this paper, we were particularly interested in determining the lowest strain that can be resolved by the system. While not specifically discussed in this work, other aspects of strain sensor performance, such as multi-directional sensitivity, are also critical aspects of future technologies based on strain gauges.[29]

4.2.2. Graphene.

Single-layer graphene exhibits reproducible piezoresistance and can thus be used as a strain gauge, with gauge factors ranging from 2-4, as reported by multiple groups.[19,30,31] The piezoresistance of single-layer graphene at strains approximately ≥0.4% is generally attributed to scattering effects stemming from unscreened charge impurities or random pseudomagnetic fields due to random strain fluctuations in the film.[30,32] Others have attributed the piezoresistance of single-layer graphene to an opening in the band gap due to the break in sublattice symmetry when C-C bonds are elongated.[33,34] The strain at which the band structure opening of graphene occurs, however, has been calculated to be above 20% by using various mathematical models

and computational simulations.[30,35–37] Such calculations, however, assume pristine, single-crystal, and defect-free graphene, which is difficult to obtain on scales larger than hundreds of microns.[38,39] Strain gauges for practical applications usually require lengths >1 mm, and will thus nearly always contain grain boundaries and defects not considered in simulations of pristine materials. Strain gauges based on graphene flakes, supported on flexible and stretchable substrates, are capable of detecting strains from 0.1% - 0.4% with wide ranging gauge factors (10^0–10^6) while maintaining compatibility with the substrate.[18,40,41]

4.2.3. Ultrathin metallic films.

One type of structure which has been exploited for its piezoresistive qualities are ultrathin metallic films on elastomeric substrates. In these composite structures, the increase in resistance upon mechanical strain has been attributed to the formation of nanoscale cracks, around which the electrical current must travel in a tortuous pathway. Upon release of the strain, the cracks close (wholly or in part), and conductivity is restored. These processes result in a type of strain gauge characterized by ultra-high sensitivity and reversibility.[15] Metallic thin film sensors, with thicknesses of tens of nanometers, have demonstrated notable sensitivity, with gauge factors up to 16,000; at strains of 2%, the film tends to form cracks and eventually bifurcates and forms an open circuit.[15,42,43] The combination of these films with self-healing polymers have led to the development of nanoscale metallic film sensors capable of withstanding 10^6 cycles under 2% strain, as the polymer is able to assist in closing the gaps formed by mechanical deformation.[14] These devices possess a greater dynamic range than that of silicon-based MEMS device but cannot resolve strains as low as the ones tested on MEMS devices (~ 0.3%). Applications requiring both mechanical deformability and high sensitivity require materials that can offer both a wide dynamic range of operation and the ability to detect the lowest strains possible.

4.2.4. Ultrathin metallic films on 2D graphene.

Our laboratory has been exploring an approach that combines the advantages of strain gauges based on single-layer graphene and those based on ultrathin metallic films. These composite structures can detect lower strains, have higher sensitivities, and exhibit wider dynamic range than either component alone. At low nominal thicknesses (≤10 nm), the morphology of gold and palladium on single-layer graphene progresses from separated island-like clusters (subcontiguous coverage) to a film of contiguous nanoscale grains. We have used these composite materials as strain gauges in a variety of applications. For example, as the active component of a wearable sensor to monitor swallowing activity when attached to the neck,[44] pulse and respiration waveforms simultaneously when attached to the ribcage,[45] and monitoring the pulse waveform on the wrist while minimizing signal drift stemming from thermal effects.[17] The composite material was also useful in a number of cellular biophysical measurements, in vitro. For example, the films have been used to monitor the mechanical activity of rat cardiomyocytes,[16] and when embedded in the sidewalls of microfluidic channels could be used to detect cells and particles as they transitted.[46] In another example, the strain-dependent variations in near-field coupling between adjacent gold nanoislands on graphene made it possible to detect (optically) the contractions of a 2D layer of myoblast cells as they were stimulated (electrically).[47]

4.3. Experimental Design

4.3.1. Framework.

The central goal of this study was to establish the range of possible mechanisms consistent with the high sensitivity of strain gauges based on ultrathin, granular metallic films ("nanoislands") supported by 2D materials. For example, both graphene and thin metallic films

exhibit piezoresistance when measured in isolation, but it is unclear which material dominates the electrical properties of the composite. (Moreover, it is unclear the extent to which mechanisms such as tunneling between closely spaced islands, increased scattering of electrons in necked regions, formation of microcracks, and quantization of electron transport due to confinement in the height axis play a role.) To tease out the relative contributions of the graphene and the metallic film to the overall piezoresistance of the graphene/metal composite, we compared results obtained with single-layer graphene (Gr) with those obtained with hexagonal boron nitride (hBN). The use of hBN as a substrate removes the conductivity and piezoresistivity possessed by graphene while retaining the island-like morphology of the metallic films, along with the ability to transfer these composite films to a variety of flexible and stretchable substrates. For the metallic films, we used both palladium and gold, which exhibit drastically different morphologies but similar piezoresistive effects when deposited on graphene at low nominal thicknesses. Thus, the four permutations of 2D substrate/metal composites (**2D/M**) used were **Gr/Pd**, **Gr/Au**, **hBN/Pd**, **hBN/Au**. In addition to the elemental makeup of the composites, the nominal thickness of metal deposited also has a profound effect on the interconnectivity and thus transport behavior of the films. We chose a narrow range (2 nm and 10 nm for palladium, and 2 nm and 16 nm for gold) and visualized the morphology by scanning electron microscopy (SEM, for gold, which exhibited relatively large islands and gaps) and transmission electron microscopy (TEM, for palladium, which exhibited smaller ones). The interconnectivity of the nanoislands were quantified by image analysis. When testing the piezoresistance of the four composites, we used small step strains of 1 ppm and 10 ppm to eliminate possible effects based on buckling, delamination, and large-scale cracking, which

occur when films are subjected to larger strains. To shed light on transport pathways activated thermally (e.g., tunneling), we obtained temperature-dependent conductivity measurements.

4.4. Selection of Materials

4.4.1. Hexagonal boron nitride (hBN) and graphene.

Hexagonal boron nitride (hBN) is a single-layer sheet of boron and nitrogen atoms which alternate with a honeycomb structure akin to graphene, but with a 2% larger lattice constant.[48–50] With a bandgap of 5.97 eV, hBN can be treated as an insulator.[51,52] Like graphene, hBN also supports the formation of metallic islands whose morphology and interconnectivity can be controlled by changing the underlying substrate by partial wetting transparency, and also by the rate, temperature, and method of deposition.[16,53,54] Like graphene, hBN (and the metallic structures it supports) can be manipulated and transferred to many types of substrates.

4.4.2. Gold and palladium.

Previous types of 2D/M strain gauges produced by our laboratory have used palladium and gold. Both metals form granular films on graphene at low nominal thicknesses, but the morphologies are distinct. In general, palladium inherently forms small, quasi-spherical grains (ca. 5 nm) with a high surface coverage and connectivity as metal is deposited. Gold, on the other hand, forms larger, faceted grains (>10 nm), and low surface coverage and connectivity before the film percolates at higher nominal thicknesses of metal deposition.[16,17,45] In previous work, the lowest strain resolved by Gr/Pd (8 nm) and for Gr/Au (5 nm) was 0.001% (10 ppm).[16,45] However, these were the smallest strains tested.

4.4.3. Measurements of gauge factor.

The piezoresistance was measured by transferring the 2D/M films to glass coverslips and performing a cantilever bend test. In this test, rectangular strips of the 2D/M films are connected to a sourcemeter using a two-wire configuration. The coverslips are placed over the step edge such that it is perpendicular to the long axis of the 2D/M film, with the step edge approximately equidistant from the electrical contacts. The film is subjected to a bending strain by depressing the edge of the overhanging glass substrate until it reaches the bottom step. To generate 0.0001% bending strain (1 ppm or 1 microstrain), we etched a 1-μm step edge into a silicon wafer. To generate bending strains of 10 ppm, we performed the same experiment except using a step edge of ~10 μm made from polyimide tape.[16,45]

4.4.4. Thermal coefficient of resistance.

The change in electrical resistance of most materials upon a change in temperature is known as the temperature coefficient of resistance (TCR). In a typical strain gauge based on a piezoresistive mechanism, materials with a substantial TCR confound measurements of strain, because the resistance is also affected by temperature. The problem of non-zero TCR in metallic foils has been solved in the case of commercial strain gauges by the use of constantan, a copper-nickel alloy that exhibits a near-zero TCR. Pure metals generally have a positive TCR (because of increased scattering of conduction electrons), while graphene has a negative TCR (due to thermally activated transport). In previous work from our group, we have shown that films of either gold or palladium on graphene could be made to have a TCR near zero in a range of 20 – 70 °C by tuning the nominal thickness and thus the surface coverage. The TCR can also give insight as to the mechanism of conduction in films of closely spaced nanoparticles. For example, electron tunneling between adjacent nanoparticles has been shown to be an active piezoresistive

mechanism in films of colloidal gold.[55] Nanoparticle films whose conduction mechanism involves tunneling have an inverse relationship between the log of resistance and temperature.[56,57] This relationship has been seen in nanoparticle films of both palladium and gold, as well as in some of their alloys.[58–62] In our case, measurement of a negative TCR in hBN/Au or hBN/Pd (in either percolated or unpercolated regimes) would suggest that tunneling plays a significant role in the electrical conductivity and possibly also in the piezoresistance of these composite films.

4.5. Results

4.5.1. Fabrication of 2D/M films.

A summary of the process used for fabrication of the 2D/M films is shown in **Figure 4.1**. Described in further detail in the **Methods** section, a thin film of gold or palladium (metal, M) was thermally evaporated with varying nominal thickness on top of graphene or hBN (two-dimensional substrate, 2D) supported on copper foil (step 1). After depositing the metal film, poly(methyl methacrylate) (PMMA) was deposited on the Cu/2D/M composite by spin coating (step 2). The copper foil was then etched by floating the Cu/2D/M/PMMA sample in ammonium persulfate, and the 2D/M/PMMA film was transferred by a water bath onto a final receiving substrate of a glass coverslip (step 3). The PMMA in the 2D/M/PMMA film was then dissolved in heated acetone (step 4). The 2D/M film, now supported by glass, was addressed with copper wires attached by carbon paint. A TEM micrograph depicting of a sample of a film of palladium islands on single-layer graphene can be seen in **Figure C.0.1**.

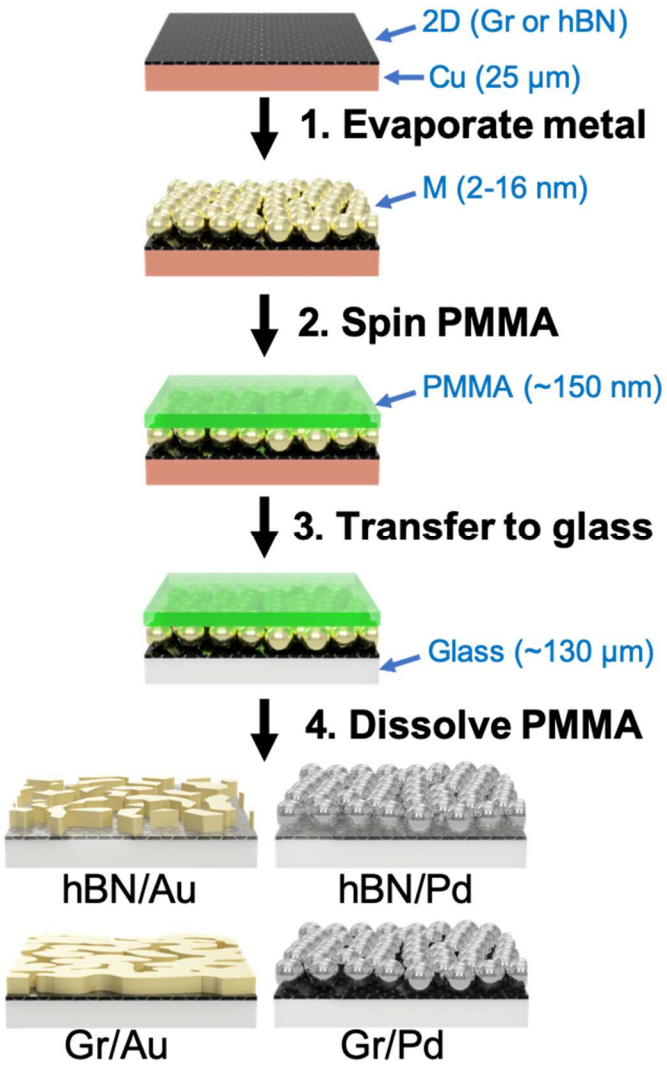

Figure 4.1 Schematic figure depicting fabrication of the 2D substrate/metallic nanoisland films.

4.5.2. Connectivity of gold nanoislands on graphene and hBN.

Thermal evaporation of gold at low nominal thicknesses produced islands and gaps of a size large enough to be visualized by scanning electron microscopy. We obtained SEM images for Gr/Au and hBN/Au films for nominal thicknesses of gold from 2 to 16 nm in increments of 2 nm (**Figure 4.2**). This range of nominal thicknesses was selected in order to produce a gradual reduction in interparticle spacing and change in morphology from disconnected to percolated as more metal is evaporated. Using image analysis, it was possible to determine both the fraction of

the surface that was covered by islands along with the interconnectivity of the metal. The interconnectivity was quantified by measuring the number of "discrete islands" per square micron. A discrete island is one for which it is possible to trace an uninterrupted path from one side of the image to the other. Plots of fractional coverage and discrete islands are plotted as a function of nominal thickness for both graphene (top) and hBN (bottom). Deposition of gold on either graphene or hBN produces a similar increase in surface coverage. The relatively steep increase in coverage between 8 and 12 nm possibly corresponds to increased favorability of lateral spreading as opposed to vertical growth in this range of nominal thickness. Films of gold on both 2D substrates appear to be mostly percolated at nominal thicknesses ≥12 nm, as determined by size of the large island in the SEM images for nominal thicknesses of 14 nm (e.g., "all white," indicating a large size of the island). When comparing graphene to hBN as a substrate, it appears that gold spreads more readily on graphene than on hBN, as the grains have a greater fractional coverage and are more highly connected at lower nominal thicknesses for graphene as opposed to hBN. A set of SEM micrographs of Gr/Au and hBN/Au with different nominal thicknesses (from 2-10 nm) can be seen in **Figure C.0.2**.

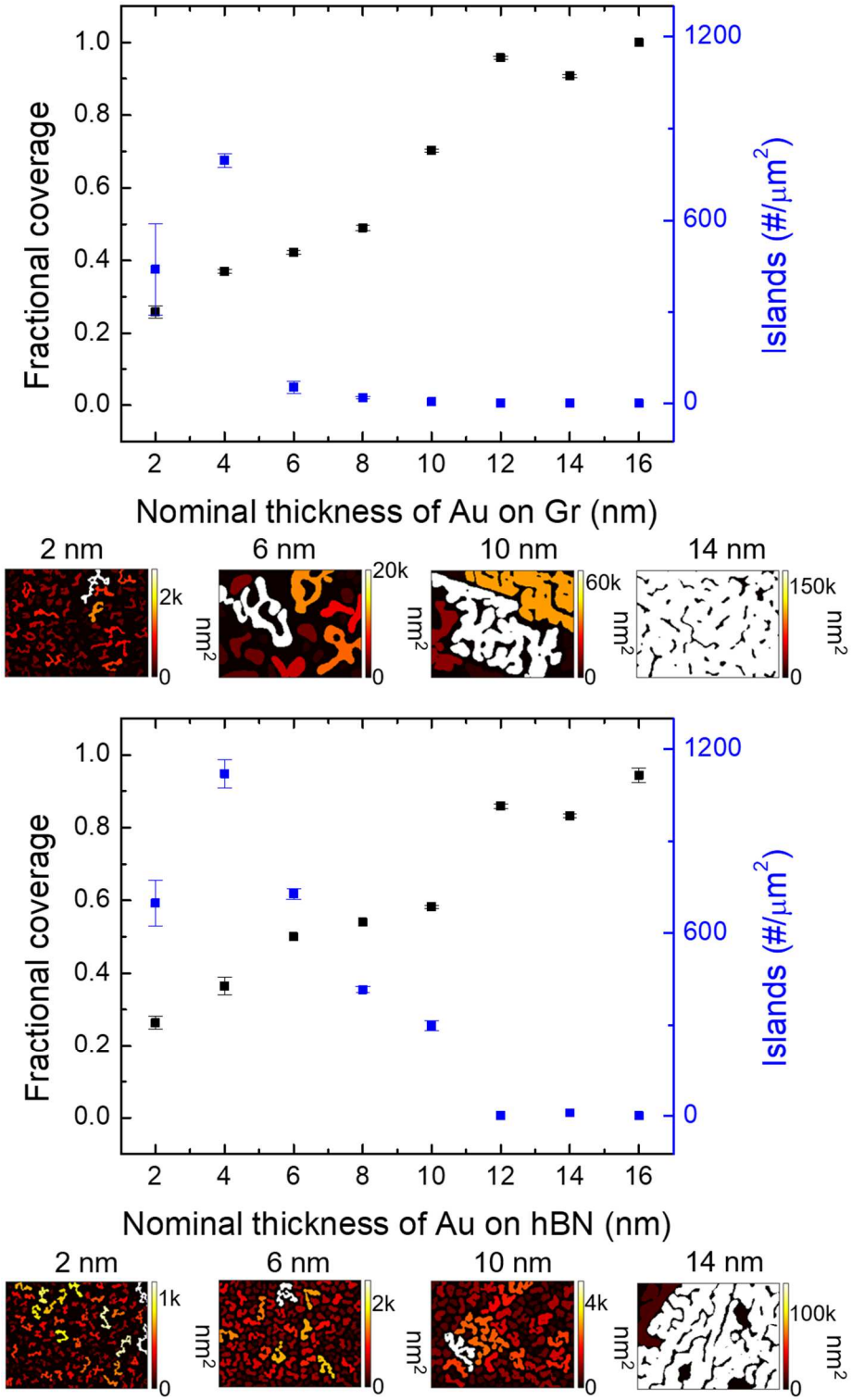

Figure 4.2 SEM image analysis. Plots of fractional coverage and density of discrete nanoislands of ultrathin gold films supported on either single-layer graphene or hBN as a function of nominal thickness of gold deposited. Sizes of the images analyzed are 502 × 376 nm. Islands are colored by the projected area (nm^2). Island colored in white (for 14 nm nominal thickness) is due to the size being greater than 100k nm^2.

4.5.3. Connectivity of palladium nanoislands on graphene and hBN.

We then performed a similar analysis for palladium as opposed to gold, seen in **Figure 4.3**. However, the morphology of palladium—consisting of small (~12 nm) quasi-spherical grains separated by nanoscale gaps much smaller than those exhibited by gold made it necessary to use TEM as opposed to SEM (**Figure 4.2**). Compared to gold, palladium exhibits a notably higher surface coverage at every nominal thickness, with coverage reaching approximately 90% at 10 nm (**Figure 4.3**). Moreover, percolation (i.e., presumed electrical contiguity of metal based on image analysis) appears to occur at a nominal thickness of 4 nm on graphene and 6 nm on hBN, i.e., at lower nominal thicknesses compared to gold on either substrate. The earlier onset of percolation in palladium can partially be attributed to the inherently higher surface coverage and a greater number of islands per area at low nominal thicknesses. A set of TEM micrographs of Gr/Pd and hBN/Pd for different nominal thicknesses (from 2-10 nm) can be seen in **Figure C.0.3**.

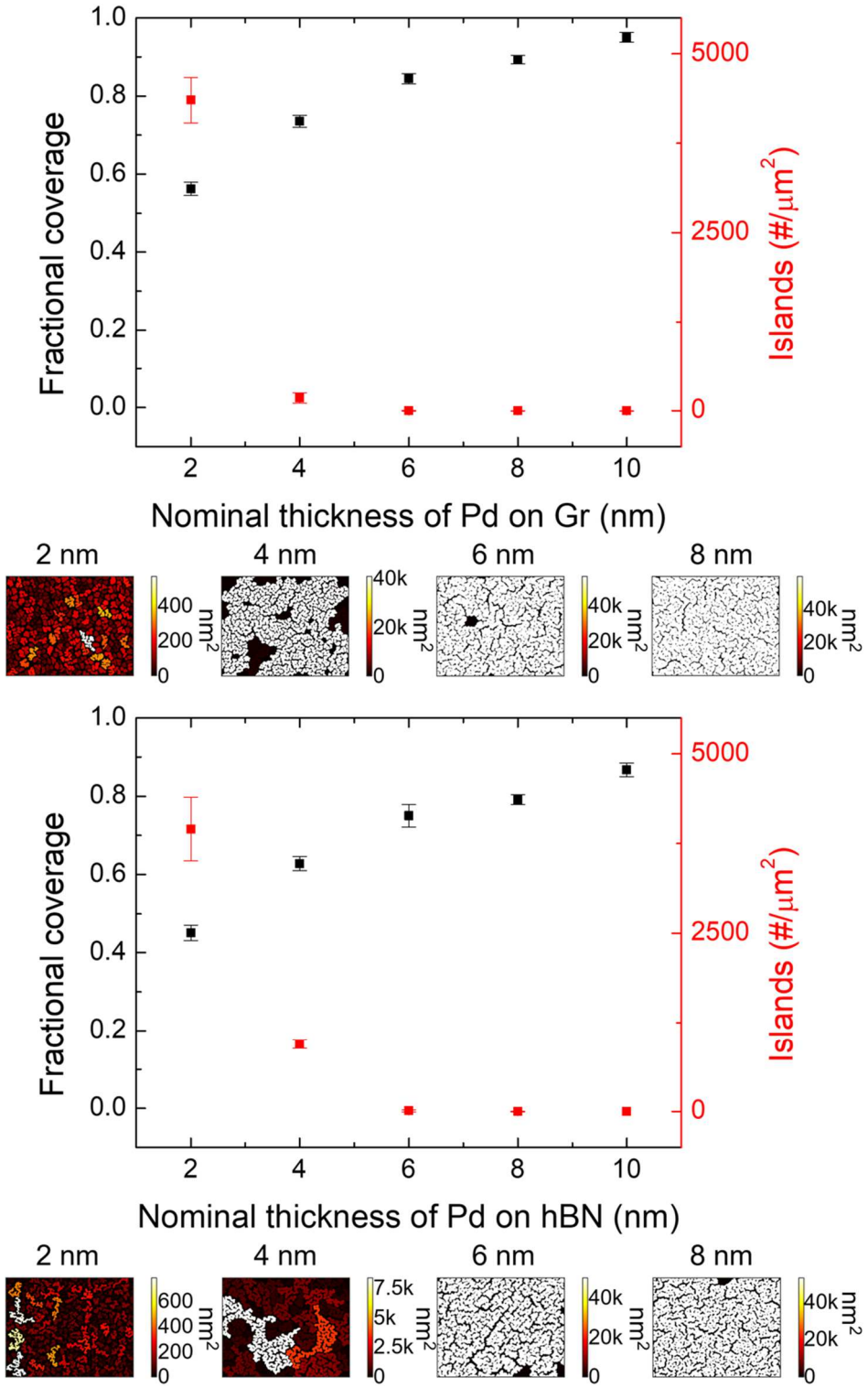

Figure 4.3 TEM image analysis. Plots of fractional coverage and density of discrete nanoislands of ultrathin palladium films supported on either single-layer graphene or hBN as a function of nominal thickness of palladium deposited. Sizes of the images analyzed are 293 × 293 nm. Islands are colored by the projected area (nm^2). Island colored in white (for 6 nm nominal thickness) is due to the size being greater than 40k nm^2.

The evolution in surface coverage of the metallic films of low nominal thickness is influenced by two parameters: the binding energy (the minimum energy required to disassemble a system of particles) of the metal atom to the substrate and its activation barrier to diffusion. For gold and palladium on graphene and hBN, palladium has the greater binding energy while both possess similar diffusion barriers.[26,63] Our observations of the progression of the surface coverage as a function of nominal thickness of both metals on either 2D substrate are consistent with these parameters. For example, at similar nominal thicknesses, palladium exhibits greater fractional surface coverage and a larger number of discrete islands than gold on either graphene or hBN. This behavior is likely a consequence of the greater binding energy of palladium to graphene, and also to hBN, than gold to graphene. Comparing 2D substrates, surface coverage is somewhat greater on graphene, but number of islands is greater on hBN.

In considering the differences in morphology of the metals when changing the 2D substrates, we observed that the number and size of islands for palladium is similar when the metal is deposited on either graphene or hBN (for the same nominal thicknesses). In the case of gold, however, the number of islands is notably greater in the case of hBN while the size of the islands is much greater on graphene, starting from a nominal thickness of 6 nm until the islands percolate. Considering that the binding energy of gold is low (~0.09 eV) when compared to palladium (~ 1 eV) on either 2D substrate and the activation barrier for diffusion of gold is also low (~ 0.4 eV on Gr and ~ 0.13 eV on hBN), the differences in morphology between Gr/Au and hBN/Au can potentially stem from the small amount of energy required to disassemble and diffuse gold adatoms on the 2D surfaces.[26,27,63,64]

4.5.4. Sheet resistance measurements.

To support the microscopy results which identified the onset of percolation (visually), we measured the sheet resistances of the composite films as a function of nominal thickness (**Figure 4.4**). In the case of hBN/Pd, nominal thicknesses ≥ 6 nm of palladium affected a transition from insulating to conductive, while for hBN/Au, ≥ 12 nm of gold on hBN transitioned from insulating to conductive. (Data points for hBN/M which registered as open circuits are not shown.) These findings are consistent with the image analysis of **Figure 4.2** and **Figure 4.3** where the number of islands per square centimeter decreases to zero at the same nominal thickness that the sheet resistance became measurable. Gr/M films gave measurable sheet resistances at all nominal thicknesses, which can be attributed to the conductivity inherent to single-layer graphene. A curious feature of Gr/M (black squares in **Figure 4.4**) is the initial increase in sheet resistance (for palladium, **4.4a**) or roughly constant value (for gold, **4.4b**) for the first few nanometers of metal deposited. The increase in sheet resistance in the metal films supported on graphene can possibly be due to the introduction of defect or scattering sites that can alter the band structure of pristine graphene.[25,65–68]

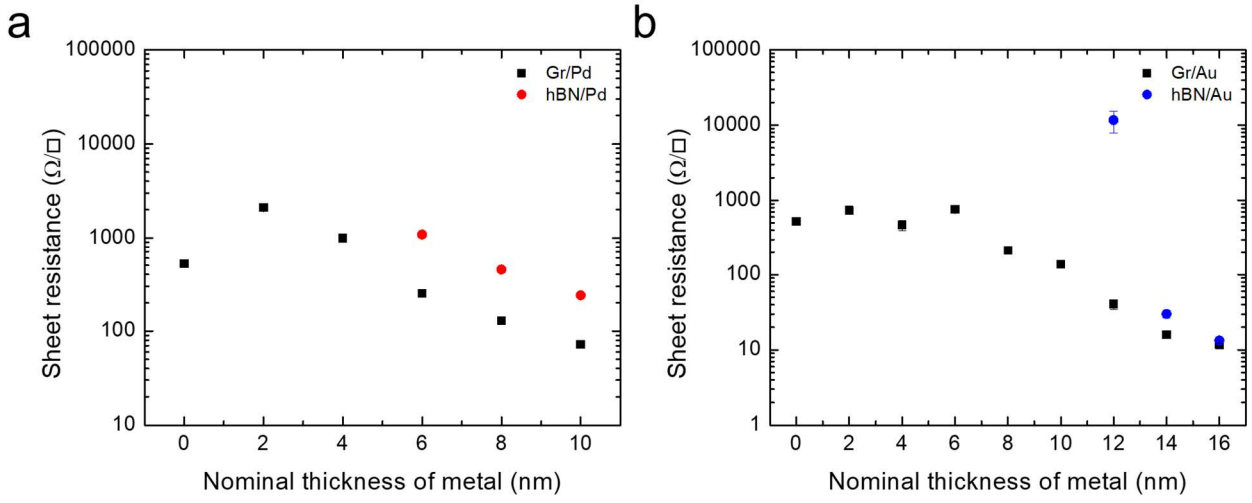

Figure 4.4 Sheet resistance of 2D/M films. Sheet resistance measurements of (a) 2D/Pd and (b) 2D/Au as a function of nominal thickness of metal deposited. Data for (a) Gr/Pd reprinted with permission from ref.42.

4.5.5. Piezoresistive response.

The films were tested for their piezoresistive response by subjecting them to 0.001% (10 ppm) and 0.0001% (1 ppm) bending strains using the cantilever setup shown in **Figure 4.5**. Among all four permutations of 2D/M films tested, Gr/Pd, hBN/Pd, and Gr/Au were able to detect strains of 1 ppm. Films consisting of hBN/Au showed open circuits for all nominal thicknesses ≤10 nm (and thus no piezoresistance) owing to the insulating behavior of hBN and the lack of interconnectivity of gold. For higher nominal thicknesses, at which gold formed a percolated network, the films were conductive but did not undergo a measurable change in resistance for either 1 ppm or 10 ppm strain. In the case of hBN/Pd, the unpercolated films gave open circuits, while the percolated films (≥ 6 nm nominal thickness) exhibited relatively large changes in resistance for both the 1 ppm and 10 ppm step strain, confirming that the highly granular film of palladium alone is responsible for the piezoresistance. Interestingly, the gauge factor was larger for the smaller step strain, suggesting that much of the effects leading to the piezoresistive response occurred upon the early stages of deformation. We attribute the lack of piezoresistive sensitivity in hBN/Au films to greater ductility and thicker connections (e.g., "isthmuses") between adjacent islands which, compared to palladium, are less likely to break at small strains. It should be noted that previous work by our group has demonstrated the reliability of these films under cyclical strain.[44,45]

In contrast to films of either gold or palladium supported by hBN, all metallic films supported by graphene—even unpercolated ones—exhibited a measurable change in the resistance at 1 ppm strain. The resistance of graphene alone, however, was insensitive to strains of either 1 ppm or 10 ppm (**Figure 4.5**). Coincidentally, the deposition of an unpercolated film

onto graphene did not decrease its resistance (**Fig. 4a/b**), yet these films exhibited a measurable gauge factor, whereas graphene alone did not, at least at the very small step strains tested. Thus, a reduction in conductivity with small nominal thicknesses corresponded to the onset of piezoresistive sensitivity. The mechanism for this transition is not entirely clear, though, several changes in the graphene occur at the initial stages of metallization, which could be envisioned to affect the evolution in electrical resistance with strain. For example, palladium is known to react with graphene—forming palladium carbide bonds—which degrades its conductivity.[65,66] The effect of mechanical deformation on the electronic structure of so-modified graphene is not clear. Moreover, the adhesion of metal islands to the surface of graphene would also produce an inhomogeneous strain field whose effects on the electromechanical behavior are not straightforward to predict. Plots of the Gr/M responses to 1 ppm strain for a case of a disconnected metal film and a percolated subcontiguous film can be seen in **Figure C.0.4**.

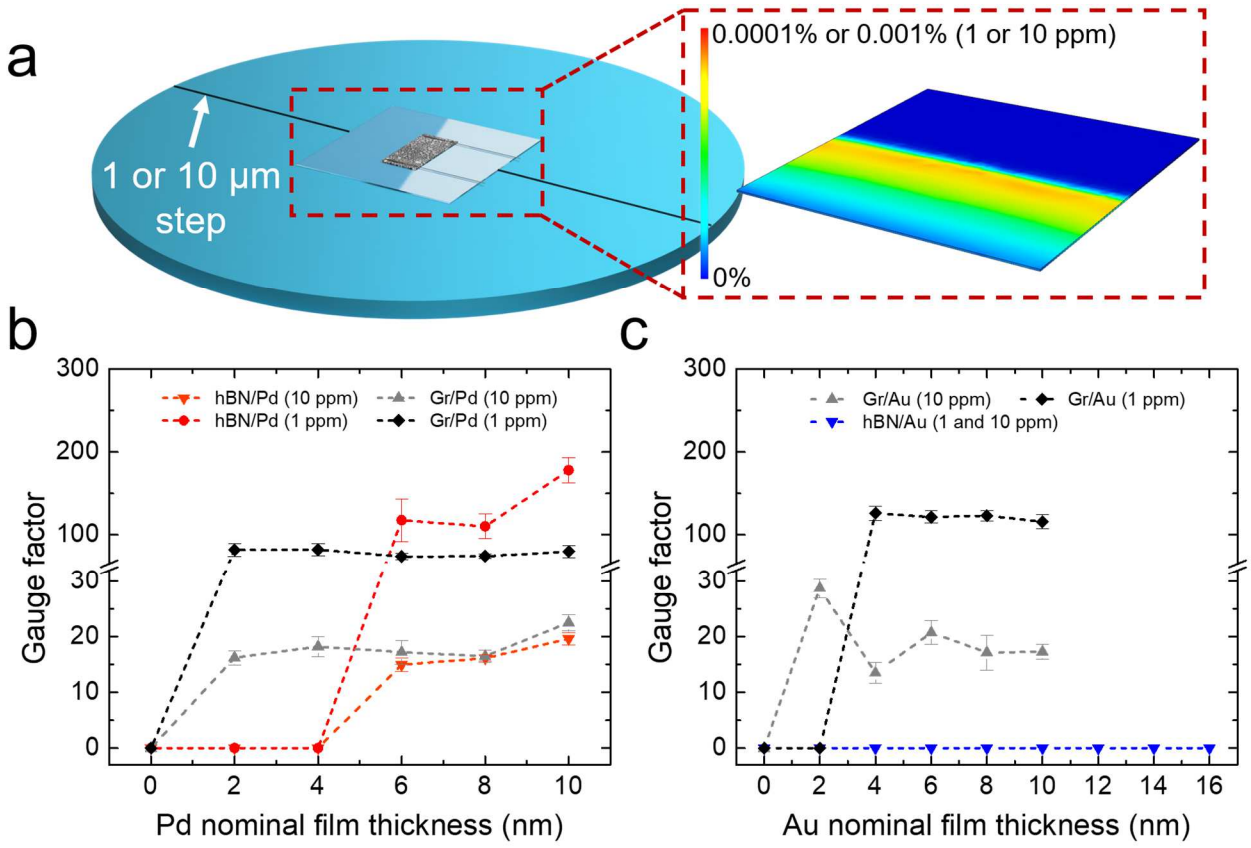

Figure 4.5 Piezoresistive characterization of 2D/M films. (a) Experimental schematic drawing and finite element analysis (FEA) of cantilever strain experiments that generated either 1 ppm or 10 ppm tensile strain. Gauge factor measurements of the piezoresistive response of (b) 2D/Pd and (c) 2D/Au samples.

4.5.6. Temperature coefficient of resistance.

To elucidate the mechanism of conductivity in the 2D/M composites that produced a piezoresistive response, we measured the temperature coefficient of resistance (TCR). In particular, we were looking for evidence of decreased resistance with increasing temperature, especially in hBN/M, which would be consistent with a contribution of tunneling to the overall conductivity (which would also implicate a piezoresistive mechanism mediated, at least in part, by tunneling). To obtain the measurements, samples were placed on heating stage and the temperature was raised from 20 □ to 70 □, in increments of 5 □. The data points corresponding to hBN/Pd were measured here for the first time, while those corresponding to Gr/M were

obtained from our previous work[69] (**Figure 4.6a** and **Figure 4.6b**). In the case of the hBN/Pd composites, all nominal thicknesses of palladium tested gave a positive TCR. Increased resistance in metals at high temperature is generally attributed to scattering.[70,71] We conclude from these measurements—along with the fact that these films appear to be percolated by TEM (**Figure 4.3**)—that tunneling is not dominant and does not appreciably contribute to the piezoresistive mechanism of hBN/Pd films.

The temperature-dependent resistivity of Gr/M films is complicated by the fact that graphene itself has a negative TCR, which could be erroneously interpreted as evidence for tunneling between metallic particles. Previous work from our group (reproduced in **Figure 4.6**) has demonstrated that the negative TCR of graphene can be overcome with the deposition of a sufficient nominal thickness of metal. It should be noted however, that depositing an excessive amount of metal on single-layer graphene can create a film with a TCR of sufficient magnitude to interfere with the ability of the film to respond reliably to strain. For example, the transition from negative to positive TCR for Gr/Au occurs at nominal thicknesses of approximately 8 nm while the transition for Gr/Pd occurs at 0.9 nm.[17] Given the morphology of these films seen in **Figure 4.2** and **Figure 4.3** we can deduce that the transition of TCR from negative to positive happens approximately at the onset of percolation, where the conductive pathway changes from dominated by graphene to dominated by metal. It should be noted that a higher metal deposition rate of 0.05 Å/s was used in previous TCR measurements (**Figure 4.6a** and **Figure 4.6b**) compared to a rate of 0.03 Å/s for this study, which could account for morphological differences (namely different nominal thicknesses at which percolation occurs) between the studies. Nevertheless, we can infer that the TCR values of our samples measured in **Figure 5** can be either negative due to the negative TCR of pristine graphene (i.e. Au $\leq$ 8 nm) or near-

zero/positive (i.e. Pd ≥ 0.9 nm). Regardless of the TCR, all graphene samples with any amount of metal (even unpercolated coverages) registered sensitivity to 1 ppm strain. These observations highlight the importance of both the graphene and the metal in producing the piezoresistive response, though they also point away from tunneling as a dominant mechanism of either conductance or piezoresitance.[72] **Table 4.1** tabulates comparisons of the gauge factor and the lowest resolvable strain of the 2D/M composites.

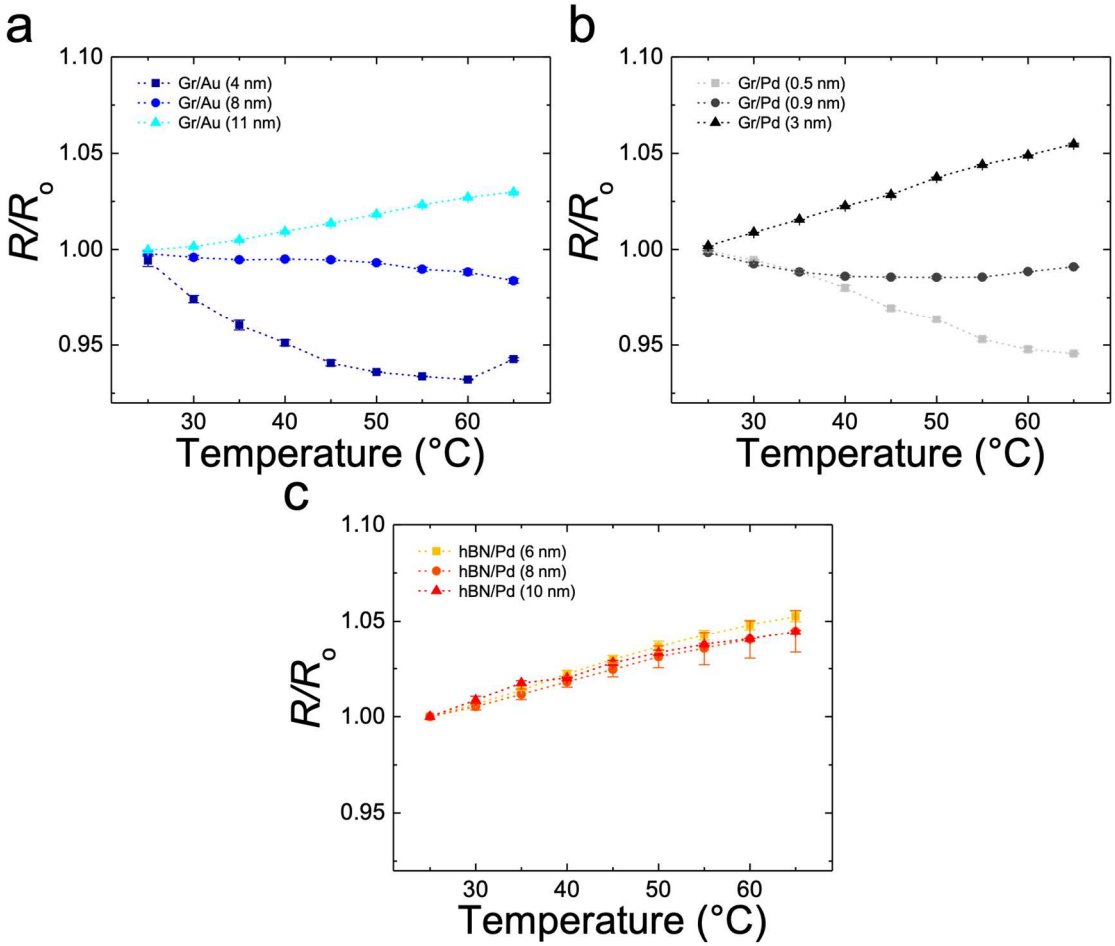

Figure 4.6 Temperature coefficient of resistance of 2D/M films. (a,b) TCR measurements of Gr/M systems from previous work (top row, reprinted with permission from ref.17) and (c) hBN/Pd systems capable of detecting 1 ppm strain.

Table 4.1 Table depicting figures of merit for the 2D substrate/metal composites and their respective components. Metal morphology on top of the 2D substrate is classified as a disconnected film (d) or a percolated subcontiguous film (p). The values in nm refer to nominal thickness, as measured by quartz crystal microbalance during deposition.

2D/M	**Sheet Resistance** (Ω/sq.)	**Gauge Factor at 1 ppm strain**	**Lowest resolvable strain** (ppm strain)
Gr	521	0	>10
Gr/Pd (d, 2 – 4 nm)	1001 – 2100	81.5-82	1
Gr/Pd (p, 6 – 10 nm)	72 – 251	74-80	1
Gr/Au (d, 2 – 8 nm)	213 – 737	123-126	1
Gr/Au (p, 10 – 16 nm)	12 – 137	~116	1
hBN	N/A	0	N/A
hBN/Pd (d, 2 – 4 nm)	N/A	0	N/A
hBN/Pd (p, 6 – 10 nm)	240 – 1087	118-178	1
hBN/Au (d, 2 – 8 nm)	N/A	0	N/A
hBN/Au (p, 10 – 16 nm)	13 – 11620	0	>10

4.6. Conclusions

These experiments have shed light on the mechanism of piezoresistance of ultrasensitive strain gauges based on metallic films on 2D substrates. In particular, the use of hexagonal boron nitride as an alternative to graphene to separate the intrinsic piezoresistance of the 2D substrate from that of the metal highlighted the profound effect of the substrate. Indeed, unpercolated films of metal on hBN produced no piezoresistive response at strains ≤10 ppm; physical continuity of the metallic film was necessary to achieve sensitivity, and only in the case of palladium, for the regime of small strains tested. In contrast, the electrical resistance of even disconnected films of

metal on graphene could resolve strains ≥1 ppm. Interestingly, however, the electrical resistance of graphene alone did not have a resolution high enough to detect small strains. The fact that morphologies on hBN in which the metal was disconnected produced open circuits—along with the fact that the resistance of these films increased with temperature—also point to the absence of tunneling as a dominant mode of either conductance or piezoresistivity. We highlight the low strains detectable (≥1 ppm) by several entries in **Table 4.1**. These strains are among the smallest ever tested for nanostructured strain gauges, and could thus be useful in measuring small effects in structural health monitoring and biomechanics (particularly of cells, which produce small forces and displacements). Shortcomings of our approach are that it is empirical and does not consider electronic coupling between the metal and the 2D substrates or quantization of charge transport in the metallic films given their extremely small thicknesses. For example, a simple thought experiment, described in the Supporting Information, suggests that dissimilar densities of states between continuous regions of different thicknesses could lead to significant backscattering of conduction electrons; this effect would in principle be augmented with tensile strains, when stress may be concentrated in the thinner regions.[73–78] Other differences between the 2D substrates, such as the mechanical properties and adhesion to metal adatoms, could possibly contribute to the differences in piezoresistive performance when comparing the Gr/M to its hBN/M counterpart. In sum, however, we believe that the phenomenological approach used here—especially the use of hBN as an alternative to graphene—helps to elucidate the mechanism by which piezoresistance arises so that such systems can be made more reliable and sensitive in a variety of applications in engineering and healthcare.

4.7. Methods

4.7.1. Fabrication.

The following steps refer to those indicated in **Figure 1**. Step 1: The nominal thickness of palladium or gold nanoislands was deposited on top of single layer-graphene or single-layer hexagonal boron nitride on copper foil (GrollTex, Inc.) using thermal evaporation (Orion System, AJA International) at a rate of 0.03 Å/s. Step 2: 4% PMMA (by mass, product no. 43982, Alfa Aesar) in anisole (Acros Organics) was deposited on top of the copper foil/2D substrate/metal by spin coating (4000 rpm, 4000 rpm/s, 60 s). The film was then heated to 150 °C for 5 min to remove residual solvent. Step 3: The copper foil/2D substrate/metal/PMMA was cut into 0.5 cm × 1 cm strips and the supporting copper foil was etched away in 0.05 g/mL ammonium persulfate (Acros Organics**) in water**. The film of 2D substrate/metal/PMMA was transferred out of the ammonium persulfate by adhering the edge of the film to a glass slide, lifting out the film from the ammonium persulfate, and plunging the glass slide into a water bath, releasing the film on the surface of the water.

The 2D substrate/Metal/PMMA film was then transferred onto a 2.54 cm × 2.54 cm glass coverslip (Sail Brand, 130-170 μm thickness), resulting in glass coverslip/2D substrate/metal/PMMA. Step 4: After transferring the obtaining the glass coverslip/2D substrate/metal/PMMA architecture, the PMMA was dissolved in a hot acetone bath of around 40 □ for three repetitions of 5 min. The After the bath, the sample was immediately rinsed with IPA and placed under vacuum to dry. After allowing the composite film to dry, the sensor was addressed with copper wire; carbon paint was painted on the contact area (DAG-T-502, Ted Pella, Inc.) and left to dry in a fume hood, resulting in the finished device (glass coverslip/2D substrate/Metal/Copper wire). This fabrication technique was used to create devices for cantilever and TCR experiments.

4.7.2. Imaging and image analysis.

The imaging of the gold nanoisland samples on graphene and hBN were done on a Zeiss Sigma 500 SEM. All samples were imaged at accelerating voltages ≤1 kV, with an aperture size of 30μm. Imaging of the palladium samples on graphene and hBN were done on a JEOL 1200 EX II TEM. All samples were images at an accelerating voltage of 80 kV.

For the analysis of the SEM and TEM images, the raw image files were edited by Adobe Photoshop CC 2019 Software by increasing the contrast, and in the case of TEM images, converting pixels stemming from the islands to white and gaps were converted to black pixels. The edited SEM and TEM images were analyzed using a custom python code, which extensively used the mahotas computer vision and image processing library.[79] An iteration of this code is available freely at (https://github.com/juramire1/SEM_TEM_Image_Analysis). An overview of the analysis is given previous work.[17]

4.7.3. Measurements of gauge factor.

For the cantilever strain experiment, where the materials were strained to 0.0001% (1 ppm, seen in **Figure 5**), the device on the coverslip was partially suspended, clamped with a 1.27 cm overlap, over a silicon step edge of ~1 μm. The step edge in silicon was created by spinning a layer SU8 photoresist over a silicon wafer and developing half of the wafer to define a straight edge across the wafer diameter. The exposed silicon surface was etched using reactive ion etching (RIE ICP - Oxford Plasmalab 100) for 4 min. A radio frequency source at 30 W and an inductively coupled plasma (ICP) source at1200 W was used, with 25 sccm of SF_6 and 50 sccm of C_4F_8 at a chamber pressure of 15 mTorr. After etching the silicon surface, the remaining photoresist was removed. In the case of 0.0001% (1 ppm) strain, the device on the coverslip was partially suspended, clamped with a 1.27 cm overlap, over a Si step edge of ~1 μm, made by

adhering polyimide tape (Caplinq, Product No. PIT0.5S UT/25.4) to a 7.62 cm × 5.08 cm glass slide. The resistance measurements were recorded using two-point measurements using a Keithley 2611B SourceMeter and custom LabView software. The tensile strain applied to the sensor device was calculated by FEA analysis of our experimental setup, described below. Signal drift in the sensors, due to thermal effects, were corrected using OriginPro 8.1.

4.7.4. Finite-element modeling.

All finite element analysis models were done using Fusion360 (Autodesk). A force was applied to the edge of the glass coverslip overhanging the respective cantilever steps. The force applied corresponded to the vertical displacement between the hanging coverslip edge and the supporting substrate.

4.7.5. Sheet resistance.

Samples for sheet-resistance measurements were prepared using the evaporation and polymer-coating technique indicated above, then cut into 2.54 cm x 2.54 cm squares and mounted on 5.08 cm x 7.62 cm glass slides. The sheet resistance was measured using a 4-point probe attachment on a Keithley 2400 SourceMeter and confirmed with contact-free resistance measurement (Delcom 20J3).

4.7.6. Temperature coefficient of resistance (TCR).

To determine the thermal coefficient of resistance, samples (of 2D substrate/metal) were cut into 0.5 cm × 1 cm strips, mounted onto a 2.54 cm × 2.54 cm glass coverslip (Sail Brand, 130-170 μm thickness), and copper wire contacts were addressed using carbon paint (DAG-T-502, Ted Pella, Inc.). These devices were heated from room temperature to 70°C, in 5°C increments using an Instec mK2000 high precision temperature controller. The resistance of each

device was recorded using a Keithley 2611B after a steady-state resistance was reached (<1% change).

Acknowledgements

This work was supported by the National Institutes of Health Director's New Innovator Award, Grant 1DP2EB022358. J.R. acknowledges support provided by the National Science Foundation Graduate Research Fellowship Program under Grant DGE-1144086. A.U. acknowledges support provided by the San Diego Nanotechnology Infrastructure REU summer program, supported by National Science Foundation (Grant ECCS-1542148). Additional support was provided by the Center for Wearable Sensors in the Jacobs School of Engineering at the University of California, San Diego, and member companies Qualcomm, Sabic, Cubic, Dexcom, Corning, Honda, Samsung, and Sony. This work was performed in part at the San Diego Nanotechnology Infrastructure (SDNI), a member of the National Nanotechnology Coordinated Infrastructure, which is supported by the National Science Foundation (Grant ECCS-1542148).

Chapter 4, in full, is a reprint of material that has been submitted for publication. Julian Ramírez[†], Armando D. Urbina[†], Andrew T. Kleinschmidt, Mickey Finn III, Samuel J. Edmunds, Guillermo L. Esparza, and Darren J. Lipomi. The dissertation author was the primary investigator and author of this paper.

References

(1) Yang, T.; Jiang, X.; Zhong, Y.; Zhao, X.; Lin, S.; Li, J.; Li, X.; Xu, J.; Li, Z.; Zhu, H. A Wearable and Highly Sensitive Graphene Strain Sensor for Precise Home-Based Pulse Wave Monitoring. *ACS Sensors* **2017**, *2* (7), 967–974.

(2) Segev-Bar, M.; Haick, H. Flexible Sensors Based on Nanoparticles. *ACS Nano* **2013**, *7* (10), 8366–8378.

(3) Lynch, J. P. A Summary Review of Wireless Sensors and Sensor Networks for Structural Health Monitoring. *Shock Vib. Dig.* **2006**, *38* (2), 91–128.

(4) Jibril, L.; Ramírez, J.; Zaretski, A. V.; Lipomi, D. J. Single-Nanowire Strain Sensors Fabricated by Nanoskiving. *Sensors Actuators, A Phys.* **2017**, 263, 702-706.

(5) Kim, Y. S.; Lu, J.; Shih, B.; Gharibans, A.; Zou, Z.; Matsuno, K.; Aguilera, R.; Han, Y.; Meek, A.; Xiao, J.; Tolley, M. T.; Coleman, T. P. Scalable Manufacturing of Solderable and Stretchable Physiologic Sensing Systems. *Adv. Mater.* **2017**, *29* (39), 1–11.

(6) Hollander, L. E.; Vick, G. L.; Diesel, T. J. The Piezoresistive Effect and Its Applications. *Rev. Sci. Instrum.* **1960**, *31* (3), 323–327.

(7) He, R.; Yang, P. Giant Piezoresistance Effect in Silicon Nanowires. *Nat. Nanotechnol.* **2006**, *1* (1), 42–46.

(8) Smith, C. S. Piezoresistance Effect in Germanium and Silicon. *Phys. Rev.* **1954**, *94* (1), 42–49.

(9) Bardeen, J.; Shockley, W. Deformation Potentials and Mobilities in Non-Polar Crystals. *Phys. Rev.* **1950**, *80* (1), 72–80.

(10) Cao, L.; Kim, T. S.; Mantell, S. C.; Polla, D. L. Simulation and Fabrication of Piezoresistive Membrane Type MEMS Strain Sensors. *Sensors Actuators, A Phys.* **2000**, 80 (3), 273-279.

(11) Mohammed, A. A. S.; Moussa, W. A.; Lou, E. Development and Experimental Evaluation of a Novel Piezoresistive MEMS Strain Sensor. *IEEE Sens. J.* **2011**, 11 (10), 2220-2232

(12) Hautamaki, C.; Zurn, S.; Mantell, S. C.; Polla, D. L. Experimental Evaluation of MEMS Strain Sensors Embedded in Composites. *J. Microelectromechanical Syst.* **1999**, 8 (3), 272-279.

(13) Jeon, H.; Hong, S. K.; Kim, M. S.; Cho, S. J.; Lim, G. Omni-Purpose Stretchable Strain Sensor Based on a Highly Dense Nanocracking Structure for Whole-Body Motion Monitoring. *ACS Appl. Mater. Interfaces* **2017**, *9* (48), 41712–41721.

(14) Park, B.; Lee, S.; Choi, H.; Kim, J. U.; Hong, H.; Jeong, C.; Kang, D.; Kim, T. Il. A Semi-Permanent and Durable Nanoscale-Crack-Based Sensor by on-Demand Healing. *Nanoscale* **2018**, *10* (9), 4354–4360.

(15) Kang, D.; Pikhitsa, P. V.; Choi, Y. W.; Lee, C.; Shin, S. S.; Piao, L.; Park, B.; Suh, K. Y.; Kim, T. Il; Choi, M. Ultrasensitive Mechanical Crack-Based Sensor Inspired by the Spider Sensory System. *Nature* **2014**, *516* (7530), 222–226.

(16) Zaretski, A. V; Root, S. E.; Savchenko, A.; Molokanova, E.; Printz, A. D.; Jibril, L.; Arya, G.; Mercola, M.; Lipomi, D. J. Metallic Nanoislands on Graphene as Highly Sensitive Transducers of Mechanical, Biological, and Optical Signals. *Nano Lett.* **2016**, *16* (2),

1375–1380.

(17) Marin, B. C.; Root, S. E.; Urbina, A. D.; Aklile, E.; Miller, R.; Zaretski, A. V.; Lipomi, D. J. Graphene–Metal Composite Sensors with Near-Zero Temperature Coefficient of Resistance. *ACS Omega* **2017**, *2* (2), 626–630.

(18) Zhao, J.; He, C.; Yang, R.; Shi, Z.; Cheng, M.; Yang, W.; Xie, G.; Wang, D.; Shi, D.; Zhang, G. Ultra-Sensitive Strain Sensors Based on Piezoresistive Nanographene Films. *Appl. Phys. Lett.* **2012**, *101* (6) 063112-1–063112-5.

(19) Smith, A. D.; Niklaus, F.; Paussa, A.; Schröder, S.; Fischer, A. C.; Sterner, M.; Wagner, S.; Vaziri, S.; Forsberg, F.; Esseni, D.; Östling, M.; Lemme, M. C. Piezoresistive Properties of Suspended Graphene Membranes under Uniaxial and Biaxial Strain in Nanoelectromechanical Pressure Sensors. *ACS Nano* **2016**, *10* (11), 9879–9886.

(20) Jen, S. U.; Yu, C. C.; Liu, C. H.; Lee, G. Y. Piezoresistance and Electrical Resistivity of Pd, Au, and Cu Films. *Thin Solid Films* **2003**, 434 (1-2), 316-322.

(21) Meiksin, Z. H.; Hudzinski, R. A. A Theoretical Study of the Effect of Elastic Strain on the Electrical Resistance of Thin Metal Films. *J. Appl. Phys.* **1967**, *38* (11), 4490–4494.

(22) Beloborodov, I. S.; Lopatin, A. V.; Vinokur, V. M.; Efetov, K. B. Granular Electronic Systems. *Rev. Mod. Phys.* **2007**, *79* (2), 469–518.

(23) Lee, J.; Kim, S.; Lee, J.; Yang, D.; Park, B. C.; Ryu, S.; Park, I. A Stretchable Strain Sensor Based on a Metal Nanoparticle Thin Film for Human Motion Detection. *Nanoscale* **2014**, *6* (20), 11932–11939.

(24) Xie, B.; Mao, P.; Chen, M.; Li, Z.; Liu, C.; Qin, Y.; Yang, L.; Wei, M.; Liu, M.; Wang, X.; Han, D.; Li, S.; Song, F.; Han, M.; Liu, J. M.; Wang, G. A Tunable Palladium Nanoparticle Film-Based Strain Sensor in a Mott Variable-Range Hopping Regime. *Sensors Actuators, A Phys.* **2018**, *272*, 161–169.

(25) Manadé, M.; Viñes, F.; Illas, F. Transition Metal Adatoms on Graphene: A Systematic Density Functional Study. *Carbon N. Y.* **2015**, *95*, 525–534.

(26) Yazyev, O. V.; Pasquarello, A. Metal Adatoms on Graphene and Hexagonal Boron Nitride: Towards Rational Design of Self-Assembly Templates. *Phys. Rev. B - Condens. Matter Mater. Phys.* **2010**, *82* (4), 1–5.

(27) Chan, K. T.; Neaton, J. B.; Cohen, M. L. First-Principles Study of Metal Adatom Adsorption on Graphene. *Phys. Rev. B - Condens. Matter Mater. Phys.* **2008**, *77* (23) 235430-1–235430-12.

(28) Roylance, D. *Mechanical Properties of Materials*; Massachusetts Institute of Technology: Cambridge, MA, 2008.

(29) Kim, K. K.; Hong, S.; Cho, H. M.; Lee, J.; Suh, Y. D.; Ham, J.; Ko, S. H. Highly Sensitive and Stretchable Multidimensional Strain Sensor with Prestrained Anisotropic Metal Nanowire Percolation Networks. *Nano Lett.* **2015**, *15* (8), 5240–5247.

(30) Huang, M.; Pascal, T. A.; Kim, H.; Goddard, W. A.; Greer, J. R. Electronic−Mechanical Coupling in Graphene from in Situ Nanoindentation Experiments and Multiscale Atomistic Simulations. *Nano Lett.* **2011**, *11* (3), 1241–1246.

(31) Smith, A. D.; Niklaus, F.; Paussa, A.; Vaziri, S.; Fischer, A. C.; Sterner, M.; Forsberg, F.; Delin, A.; Esseni, D.; Palestri, P.; Östling, M.; Lemme, M. C. Electromechanical Piezoresistive Sensing in Suspended Graphene Membranes. *Nano Lett.* **2013**, *13* (7), 3237–3242.

(32) Couto, N. J. G.; Costanzo, D.; Engels, S.; Ki, D.-K.; Watanabe, K.; Taniguchi, T.; Stampfer, C.; Guinea, F.; Morpurgo, A. F. Random Strain Fluctuations as Dominant Disorder Source for High-Quality on-Substrate Graphene Devices. *Phys. Rev. X* **2014**, *4* (4), 1–13.

(33) Skomski, R.; Dowben, P. A.; Sky Driver, M.; Kelber, J. A. Sublattice-Induced Symmetry Breaking and Band-Gap Formation in Graphene. *Mater. Horiz.* **2014**, *1* (6), 563–571.

(34) Hicks, J.; Tejeda, A.; Taleb-Ibrahimi, A.; Nevius, M. S.; Wang, F.; Shepperd, K.; Palmer, J.; Bertran, F.; Le Fèvre, P.; Kunc, J.; De Heer, W. A.; Berger, C.; Conrad, E. H. A Wide-Bandgap Metal-Semiconductor-Metal Nanostructure Made Entirely from Graphene. *Nat. Phys.* **2013**, *9* (1), 49–54.

(35) Pereira, V. M.; Castro Neto, A. H.; Peres, N. M. R. Tight-Binding Approach to Uniaxial Strain in Graphene. *Phys. Rev. B - Condens. Matter Mater. Phys.* **2009**, *80* (4), 1–8.

(36) Ni, Z. H.; Yu, T.; Lu, Y. H.; Wang, Y. Y.; Feng, Y. P.; Shen, Z. X. Uniaxial Strain on Graphene: Raman Spectroscopy Study and Band-Gap Opening. *ACS Nano* **2008**, *2* (11), 2301–2305.

(37) Kim, K. S.; Zhao, Y.; Jang, H.; Lee, S. Y.; Kim, J. M.; Kim, K. S.; Ahn, J.-H.; Kim, P.; Choi, J.-Y.; Hong, B. H. Large-Scale Pattern Growth of Graphene Films for Stretchable Transparent Electrodes. *Nature* **2009**, *457* (7230), 706–710.

(38) Li, X.; Cai, W.; An, J.; Kim, S.; Nah, J.; Yang, D.; Piner, R.; Velamakanni, A.; Jung, I.; Tutuc, E.; Banerjee, S. K.; Colombo, L.; Ruoff, R. S. Large-Area Synthesis of High-Quality and Uniform Graphene Films on Copper Foils. *Science (80-.).* **2009**, *324* (5932), 1312–1314.

(39) Zaretski, A. V.; Moetazedi, H.; Kong, C.; Sawyer, E. J.; Savagatrup, S.; Valle, E.; O'Connor, T. F.; Printz, A. D.; Lipomi, D. J. Metal-Assisted Exfoliation (MAE): Green, Roll-to-Roll Compatible Method for Transferring Graphene to Flexible Substrates.

Nanotechnology **2015**, *26* (4), 045301-1–045301-7.

(40) Wang, Y.; Wang, L.; Yang, T.; Li, X.; Zang, X.; Zhu, M.; Wang, K.; Wu, D.; Zhu, H. Wearable and Highly Sensitive Graphene Strain Sensors for Human Motion Monitoring. *Adv. Funct. Mater.* **2014**, *24* (29), 4666–4670.

(41) Hu, N.; Karube, Y.; Yan, C.; Masuda, Z.; Fukunaga, H. Tunneling Effect in a Polymer/Carbon Nanotube Nanocomposite Strain Sensor. *Acta Mater.* **2008**, *56* (13), 2929–2936.

(42) Yang, T.; Li, X.; Jiang, X.; Lin, S.; Lao, J.; Shi, J.; Zhen, Z.; Li, Z.; Zhu, H. Structural Engineering of Gold Thin Films with Channel Cracks for Ultrasensitive Strain Sensing. *Mater. Horizons* **2016**, *3* (3), 248–255.

(43) Park, B.; Kim, J.; Kang, D.; Jeong, C.; Kim, K. S.; Kim, J. U.; Yoo, P. J.; Kim, T. Dramatically Enhanced Mechanosensitivity and Signal-to-Noise Ratio of Nanoscale Crack-Based Sensors: Effect of Crack Depth. *Adv. Mater.* **2016**, *28* (37), 8130–8137.

(44) Ramírez, J.; Rodriquez, D.; Qiao, F.; Warchall, J.; Rye, J.; Aklile, E.; S.-C. Chiang, A.; Marin, B. C.; Mercier, P. P.; Cheng, C. K.; Hutcheson, K. A.; Shinn, E. H.; Lipomi, D. J. Metallic Nanoislands on Graphene for Monitoring Swallowing Activity in Head and Neck Cancer Patients. *ACS Nano* **2018**, *12* (6), 5913–5922.

(45) Ramírez, J.; Rodriquez, D.; Urbina, A. D.; Cardenas, A. M.; Lipomi, D. J. Combining High Sensitivity and Dynamic Range: Wearable Thin-Film Composite Strain Sensors of Graphene, Ultrathin Palladium, and PEDOT:PSS. *ACS Appl. Nano Mater.* **2019**, *2* (4), 2222–2229.

(46) Dhong, C.; Edmunds, S. J.; Ramirez, J.; Kayser, L.; Chen, F.; Jokerst, J.; Lipomi, D. J. Optics-Free, Non-Contact Measurements of Fluids, Bubbles and Particles in Microchannels Using Metallic Nanoislands on Graphene. *Nano Lett.* **2018**, 18 (8), 5306-5311.

(47) Marin, B. C.; Liu, J.; Aklile, E.; Urbina, A. D.; Chiang, A. S. C.; Lawrence, N.; Chen, S.; Lipomi, D. J. SERS-Enhanced Piezoplasmonic Graphene Composite for Biological and Structural Strain Mapping. *Nanoscale* **2017**, *9* (3), 1292–1298.

(48) Pozzo, M.; Alfè, D.; Lacovig, P.; Hofmann, P.; Lizzit, S.; Baraldi, A. Thermal Expansion of Supported and Freestanding Graphene: Lattice Constant versus Interatomic Distance. *Phys. Rev. Lett.* **2011**, *106* (13), 135501(1)–135501(4).

(49) Dean, C. R.; Young, A. F.; Meric, I.; Lee, C.; Wang, L.; Sorgenfrei, S.; Watanabe, K.; Taniguchi, T.; Kim, P.; Shepard, K. L.; Hone, J. Boron Nitride Substrates for High-Quality Graphene Electronics. *Nat. Nanotechnol.* **2010**, *5* (10), 722–726.

(50) Govind Rajan, A.; Strano, M. S.; Blankschtein, D. Ab Initio Molecular Dynamics and

Lattice Dynamics-Based Force Field for Modeling Hexagonal Boron Nitride in Mechanical and Interfacial Applications. *J. Phys. Chem. Lett.* **2018**, *9* (7), 1584–1591.

(51) Giovannetti, G.; Khomyakov, P. A.; Brocks, G.; Kelly, P. J.; Van Den Brink, J. Substrate-Induced Band Gap in Graphene on Hexagonal Boron Nitride: Ab Initio Density Functional Calculations. *Phys. Rev. B - Condens. Matter Mater. Phys.* **2007**, *76* (7), 2–5.

(52) Watanabe, K.; Taniguchi, T.; Kanda, H. Direct-Bandgap Properties and Evidence for Ultraviolet Lasing of Hexagonal Boron Nitride Single Crystal. *Nat. Mater.* **2004**, *3* (6), 404–409.

(53) Rafiee, J.; Mi, X.; Gullapalli, H.; Thomas, A. V.; Yavari, F.; Shi, Y.; Ajayan, P. M.; Koratkar, N. A. Wetting Transparency of Graphene. *Nat. Mater.* **2012**, *11* (3), 217–222.

(54) Li, H.; Zeng, X. C. Wetting and Interfacial Properties of Water Nanodroplets in Contact with Graphene and Monolayer Boron-Nitride Sheets. *ACS Nano* **2012**, *6* (3), 2401–2409.

(55) Parker, R. L.; Krinsky, A. Electrical Resistance-Strain Characteristics of Thin Evaporated Metal Films. *J. Appl. Phys.* **1963**, *34* (9), 2700–2708.

(56) Neugebauer, C. A.; Webb, M. B. Electrical Conduction Mechanism in Ultrathin, Evaporated Metal Films. *J. Appl. Phys.* **1962**, *33* (1), 74–82.

(57) Hill, R. M. Electrical Conduction in Ultra Thin Metal Films. II. Experimental. *Proc. R. Soc. A Math. Phys. Eng. Sci.* **1969**, *309* (1498), 397–417.

(58) Kazmerski, L. L.; Racine, D. M. Growth, Environmental, and Electrical Properties of Ultrathin Metal Films. *J. Appl. Phys.* **1975**, *46* (2), 791–795.

(59) Tick, P. A.; Fehlner, F. P. Electrical Behavior of Composite Discontinuous Films. *J. Appl. Phys.* **1972**, *43* (2), 362–368.

(60) Xie, B.; Mao, P.; Chen, M.; Li, Z.; Liu, C.; Qin, Y.; Yang, L.; Wei, M.; Liu, M.; Wang, X.; Han, D.; Li, S.; Song, F.; Han, M.; Liu, J. M.; Wang, G. Sensors and Actuators A : Physical A Tunable Palladium Nanoparticle Film-Based Strain Sensor in a Mott Variable-Range Hopping Regime. *Sensors Actuators A. Phys.* **2018**, *272*, 161–169.

(61) van Lith, J.; Lassesson, A.; Brown, S. A.; Schulze, M.; Partridge, J. G.; Ayesh, A. A Hydrogen Sensor Based on Tunneling between Palladium Clusters. *Appl. Phys. Lett.* **2007**, *91* (18), 1–3.

(62) Wagner, S.; Pundt, A. Conduction Mechanisms during the Growth of Pd Thin Films: Experiment and Model. *Phys. Rev. B - Condens. Matter Mater. Phys.* **2008**, *78* (15), 1–14.

(63) Liu, X.; Wang, C. Z.; Hupalo, M.; Lin, H. Q.; Ho, K. M.; Tringides, M. C. Metals on Graphene: Interactions, Growth Morphology, and Thermal Stability. *Crystals* **2013**, *3* (1),

79–111.

(64) Pandey, P. A.; Bell, G. R.; Rourke, J. P.; Sanchez, A. M.; Elkin, M. D.; Hickey, B. J.; Wilson, N. R. Physical Vapor Deposition of Metal Nanoparticles on Chemically Modified Graphene: Observations on Metal-Graphene Interactions. *Small* **2011**, *7* (22), 3202–3210.

(65) Gong, C.; McDonnell, S.; Qin, X.; Azcatl, A.; Dong, H.; Chabal, Y. J.; Cho, K.; Wallace, R. M. Realistic Metal-Graphene Contact Structures. *ACS Nano* **2014**, *8* (1), 642–649.

(66) Ramasse, Q. M.; Zan, R.; Bangert, U.; Boukhvalov, D. W.; Son, Y. W.; Novoselov, K. S. Direct Experimental Evidence of Metal-Mediated Etching of Suspended Graphene. *ACS Nano* **2012**, *6* (5), 4063–4071.

(67) Xia, F.; Perebeinos, V.; Lin, Y. M.; Wu, Y.; Avouris, P. The Origins and Limits of Metal-Graphene Junction Resistance. *Nat. Nanotechnol.* **2011**, *6* (3), 179–184.

(68) Pi, K.; McCreary, K. M.; Bao, W.; Han, W.; Chiang, Y. F.; Li, Y.; Tsai, S. W.; Lau, C. N.; Kawakami, R. K. Electronic Doping and Scattering by Transition Metals on Graphene. *Phys. Rev. B - Condens. Matter Mater. Phys.* **2009**, *80* (7), 1–5.

(69) Marin, B. C.; Root, S. E.; Urbina, A. D.; Aklile, E.; Miller, R.; Zaretski, A. V.; Lipomi, D. J. Graphene-Metal Composite Sensors with Near-Zero Temperature Coefficient of Resistance. *ACS Omega,* **2017**, 2 (2), 626-630.

(70) Leonard, W. F.; Ramey, R. L. Temperature Coefficient of Resistance in Thin Metal Films. *J. Appl. Phys.* **1966**, *37* (9), 3634–3635.

(71) Zhang, Q. G.; Zhang, X.; Cao, B. Y.; Fujii, M.; Takahashi, K.; Ikuta, T. Influence of Grain Boundary Scattering on the Electrical Properties of Platinum Nanofilms. *Appl. Phys. Lett.* **2006**, *89* (11), 2004–2007.

(72) Namba, Y. Resistivity and Temperature Coefficient of Thin Metal Films with Rough Surface. *Jpn. J. Appl. Phys.* **1970**, *9* (11), 1326–1329.

(73) Chiang, T. C. Quantum Physics of Thin Metal Films. *AAPPS Bull.,* **2008**, *18* (2).

(74) Kittel, C. *Introduction to Solid State Physics, 8th Edition*, 8th ed.; Wiley & Sons, New York, NY, 2004.

(75) Hook, J. R.; Hall, H. E. *Solid State Physics, 2nd Edition*, 2nd ed.; Wiley & Sons, New York, NY, 1995.

(76) Landauer, R. Spatial Variation of Currents and Fields Due to Localized Scatterers in Metallic Conduction. *IBM J. Res. Dev.* **1957**, *1* (3), 223–231.

(77) Wharam, D. A.; Thornton, T. J.; Newbury, R.; Pepper, M.; Ahmed, H.; Frost, J. E. F.;

Hasko, D. G.; Peacock, D. C.; Ritchie, D. A.; Jones, G. A. C. One-Dimensional Transport and the Quantisation of the Ballistic Resistance. *J. Phys. C Solid State Phys.* **1988**, 21, L209–L214

(78) Van Wees, B. J.; Van Houten, H.; Beenakker, C. W. J.; Williamson, J. G.; Kouwenhoven, L. P.; Van Der Marel, D.; Foxon, C. T. Quantized Conductance of Point Contacts in a Two-Dimensional Electron Gas. *Phys. Rev. Lett.* **1988**, *60* (9), 848–850.

(79) L. P. Coelho, Mahotas: Open Source Software for Scriptable Computer Vision, J. Open Res. Softw., **2013**, 1(1), e3.

Appendix A Supporting Information for Chapter 2

A.1. Strain Sensor Device Characterization

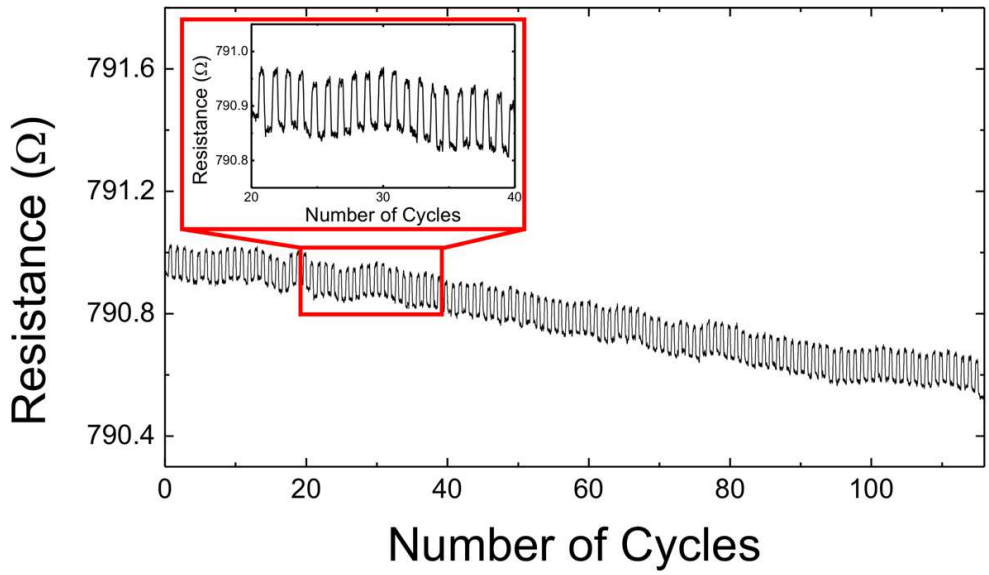

Figure A.0.1. Characterization of wearable sensor device under cyclic 0.02% strain. Characterization of device stability under 115 bending cycles of 0.02% strain.

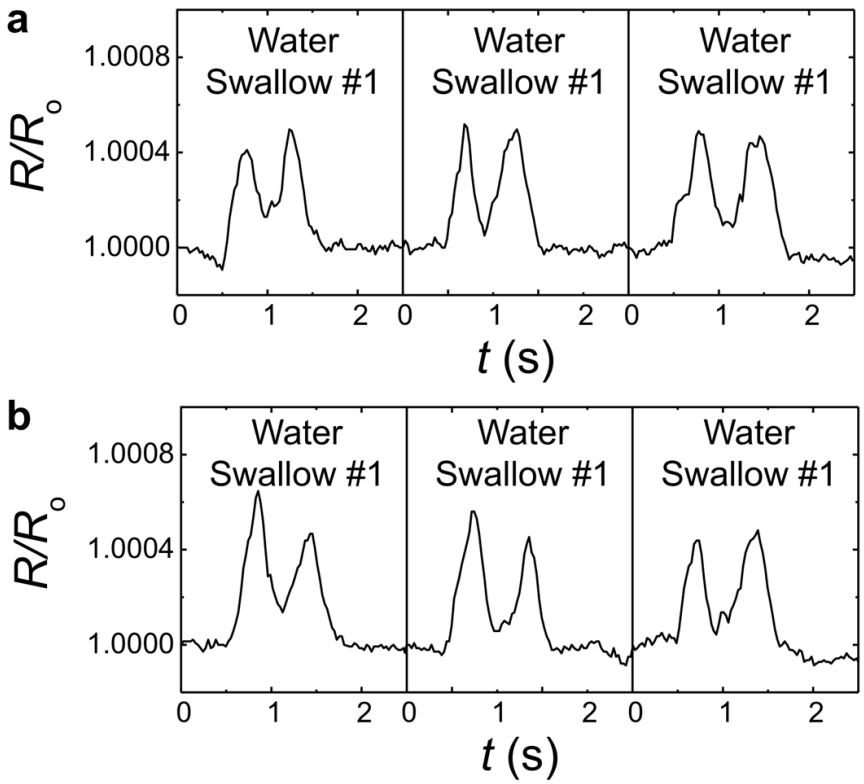

Figure A.0.2. Swallowing strain signal characterization based on elevation of heartbeat. Signal characterization as a healthy subject swallowed a bolus of 10 mL of water with (a) a resting heart rate (~55 bpm) and (b) an elevated heart rate (~95 bpm).

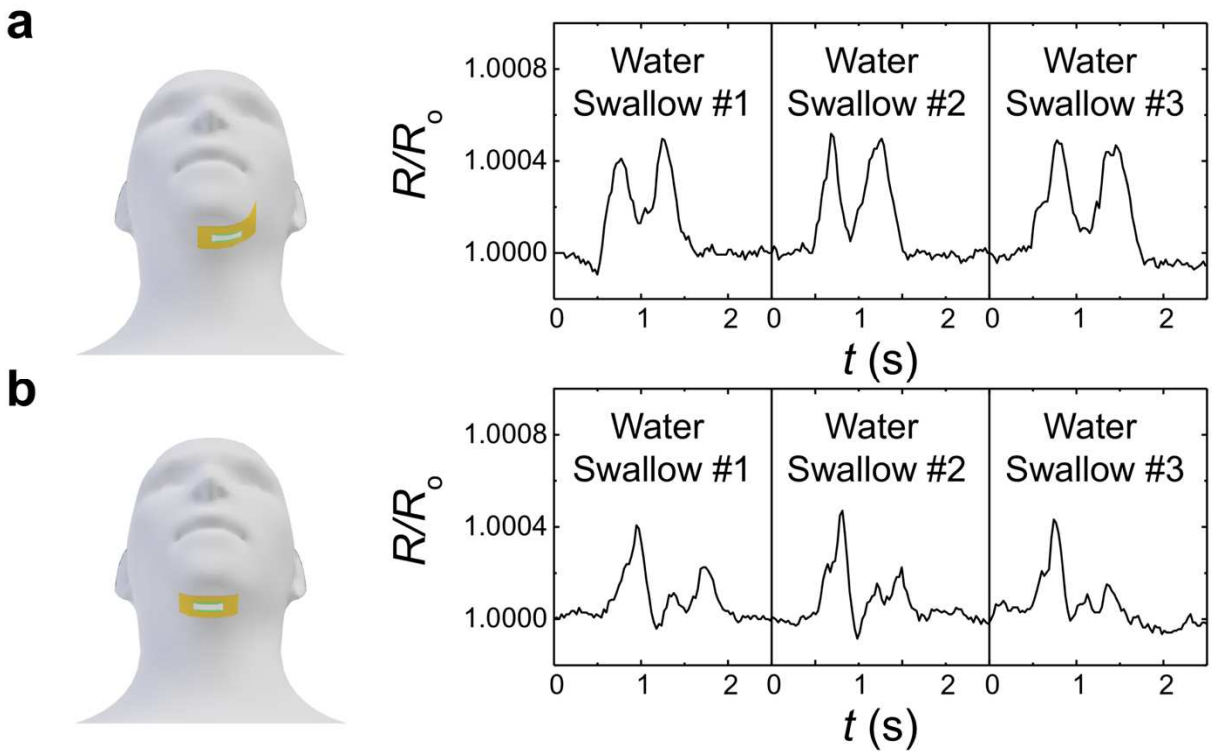

Figure A.0.3. Swallowing strain signal characterization based on device placement. Signal characterization as a healthy subject swallowed a bolus of 10 mL of water with (a) the sensor device attached in the normal position and (b) the sensor device attached to the left of the original position (on the surface of the submental triangle).

A.2. Medical Information for Head and Neck Cancer Patients

Table A.0.1 Table listing information for the head and neck cancer patients. The table lists the patients whose strain and EMG data is presented and their respective information, including gender, ethnic group, and age. The table also presents whether the patient only had cancer or radiation treatment on one side of the head and neck (unilateral) or both sides (bilateral), the amount of radiation the patient received during treatment, and if the patient developed dysphagia after treatment. The location of the patient data in the manuscript is also provided.

Name	Sex	Age	Ethnic group	Unilateral or bilateral treatment	Total radiation dose (Gy)	Dysphagia (Y/N)	Signals seen in
Patient A	M	83	White	Bilateral	70.35	Y	Figure 3b, Figure 4
Patient B	M	67	Hispanic or Latino	Bilateral	70.33	Y	Figure 3b
Patient C	M	76	Unknown	Bilateral	69.96	Y	Figure 3b
Patient D	M	54	Hispanic or Latino	Bilateral	66.0	N	Figure 3b
Patient E	F	58	White	Unilateral	66.33	N	Figure 3b, Figure 3c, Figure 4
Patient F	F	47	White	Bilateral	69.96	N	Figure 3b
Patient G	M	79	White	Bilateral	69.3	N	Figure 3d
Patient H	M	59	White	Bilateral	66	Y	Figure 6
Patient I	M	66	Asian	N/A	N/A	Y	N/A
Patient J	M	60	Unknown	Bilateral	70.33	Y	N/A
Patient K	M	43	White	Bilateral	69.96	Y	N/A
Patient L	M	57	Hispanic or Latino	Unilateral	69.3	N	N/A
Patient M	M	60	White	Bilateral	69.3	N	N/A
Patient N	M	47	White	Unilateral	69.3	N	N/A

A.3. Machine Learning Algorithm Development

A.3.1. Experimental Description

Preliminary data analysis of the sensor measurements via pattern recognition and machine learning on swallow activities yielded high accuracy rate for two tasks (**Table A.0.2**). The first task was to classify the swallowing signals of one subject based on the food bolus being swallowed. In this case, the swallowing signals were a subject swallowing 10 mL of water, a tablespoon of yogurt, and a bite from a cracker. The model was trained using a set of the swallowing data labeled as swallowing activity for a water, yogurt, or cracker bolus, and was then tested by using the trained model to predict the label for the rest of the data set. For the second task, the algorithm was trained with signals from a dysphagic patient and a healthy subject swallowing the same bolus, in this case 10 mL of water, and a new measurement could be classified as either a swallow from the healthy subject or the dysphagic patient.

Table A.0.2 Table describing the two classification tasks performed by the machine-learning algorithm. The table describes the two statistical classification tasks performed by the machine-learning algorithm. A statistical classification task deals with determining which categorical variable (class) a sample belongs to. First, the algorithm was tasked with identifying the signal of a bolus swallowed by the healthy subject between three possible choices. Second, the algorithm was tasked with identifying if the signal was that of a healthy subject or a dysphagic patient swallowing the same bolus.

Task	Data	Label	Prediction
Bolus Classification	Sensor measurements for a given set of boluses	Boluses	Given a new measurement, identify the bolus
User Identification	Sensor measurements for a fixed swallow activity for a given set of users	Users	Given a new measurement, identify the user

A.3.2. Signal Preprocessing

The raw signals from the sensor during swallowing have numerous sources of noise that make the tasks performed by the machine learning algorithm difficult. Primary examples of noise coming from the raw swallowing signals include: 1) the irregular time stamp for each resistance

reading per signal, 2) swallow signal time offset – where the actual swallowing events recorded in the sensor signals may not match in time across different measurements, and 3) variations of different signal measurements of a single bolus by a single user due to factors such as fatigue and irritation. The data was preprocessed before using the signals to reduce the error from the noise and variability of swallowing signals, thereby obtaining well-structured data points that can be compared with each other, rendering further efforts to derive generalized patterns easier. Data preprocessing consists of procedures that sanitizes raw resistance readings. First, we take the irregularly sampled data, interpolate the normalized resistance values, and resample the reading at uniform time stamps.[1] Further preprocessing was done by smoothing the original raw swallowing signal with a Savitzky-Golay filter, where an approximate, smooth curve was fitted that captured the general pattern of the raw signal.[2] After smoothing the signals, the swallowing signals of the same bolus type are then matched to the highest strain event to ensure that the swallow events across separate measurements are aligned with respect to time. **Figure S4** illustrates the methods performed on the signal measurements.

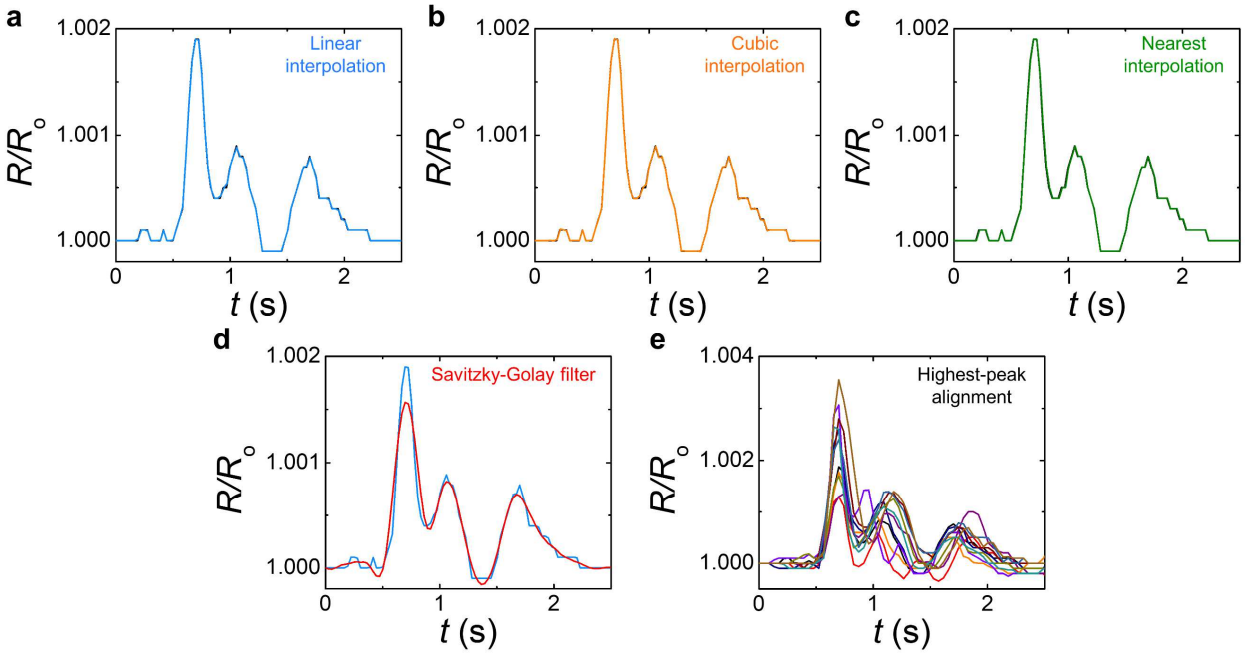

Figure A.0.4. Swallowing strain signal characterization based on device placement. Signal characterization as a healthy subject swallowed a bolus of 10 mL of water with (a) the sensor device attached in the normal position and (b) the sensor device attached to the left of the original position (on the surface of the submental triangle).

A.3.3. Feature Extraction

Feature extraction from sanitized signals consists of either automated or manual identification of statistical properties that are key to learning statistical models. Manual feature extraction requires human experts identifying properties in the data using statistical and mathematical techniques. Automatic feature extraction, on the other hand, often involves unsupervised learning algorithms, where the labels and meaningful properties are derived from the structure or distribution of data, without preexisting guidelines. Common methods relevant to feature extraction include unsupervised machine learning algorithms such as clustering, principal component analysis (PCA), and automatic feature learning by Bayesian latent factor models. Time series methods such as Fourier transform and auto correlation/regression are also popular choices for drawing useful features from temporal data, such as sensor signals and historical

logs. Figure S5 shows results from soft k-means clustering analysis on water swallow measurements.3

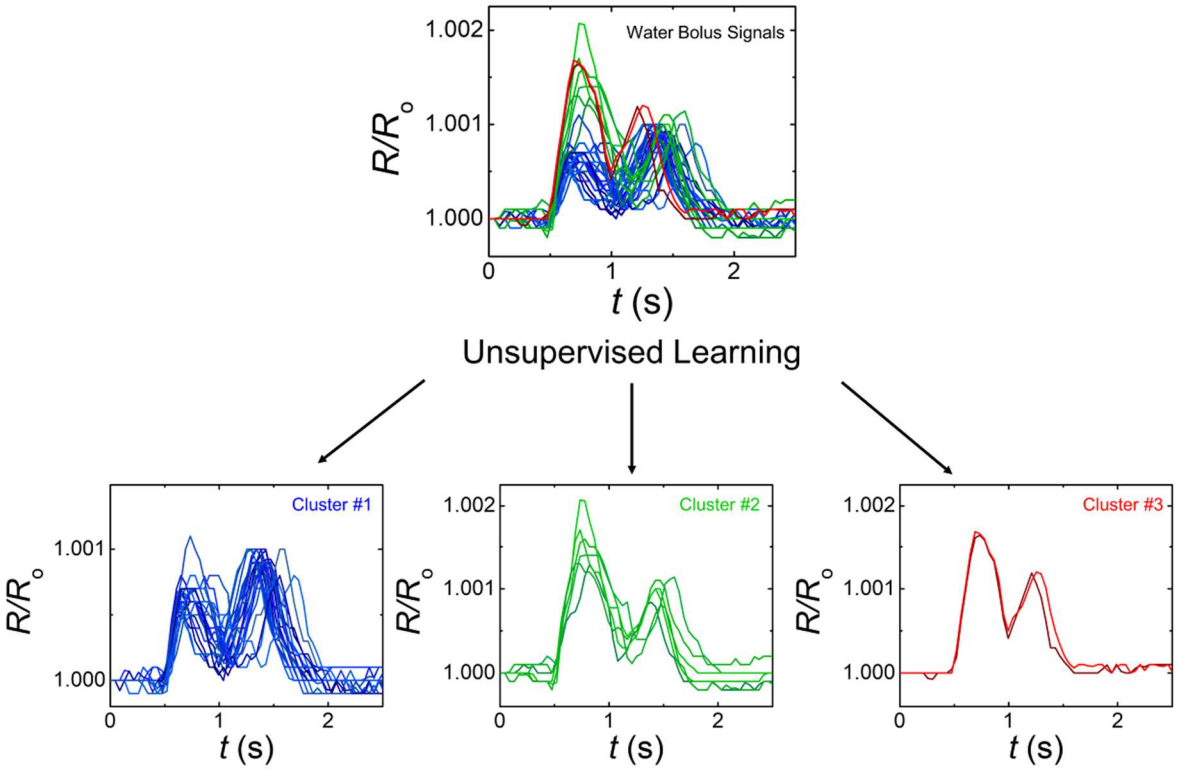

Figure A.0.5. Swallowing strain signal characterization based on device placement. Signal characterization as a healthy subject swallowed a bolus of 10 mL of water with (a) the sensor device attached in the normal position and (b) the sensor device attached to the left of the original position (on the surface of the submental triangle).

A.3.4. Model and Results

Most of the predictive tasks we have considered so far are associated with categorization, which are classical supervised machine learning classification problems, where labels (i.e. "yogurt" or "cracker" in bolus classification) are available to serve as guidelines in our training and evaluation methods. Prevalent supervised classifier models that have strong theoretical foundations include logistic regression, Support Vector Machine (SVM), boosted classifiers, and

various Bayesian methods. In our prototype data analysis on the swallow signals, we have also formulated an efficient classification model based on the L1-distance of the per-class average (**Equation S1**) that outperforms tuned SVM and AdaBoosted classifiers (**Table A.0.3**). The test results for the three models were generated through 4-fold cross validation on bolus classification and 3-fold cross validation on human subject discrimination. Cross-validation consists of stochastically partitioning the training data further into a training and a validation set. Models are then trained on the partitioned training set, and evaluated on the validation set. The stochastic property of the partitioning theoretically yields a more accurate approximation of the actual performance of the model. Furthermore, model parameters that require manual tuning can be selected by comparing the results of the classifiers, with different values assigned to the parameters, across cross-validation runs.

Setup:

$C = \{1, \ldots c\}$ where each c_i is a class for some classification task.

Training set $\langle X, Y \rangle$ where:

$X = \{\vec{x}^{(1)}, \vec{x}^{(2)}, \ldots, \vec{x}^{(m)}\}$ where each $\vec{x}^{(h)}$ is a sanitized t m-dimensional sensor measurement.

$Y = \{y^{(1)}, y^{(2)}, \ldots, y^{(m)}\}$ where each $y^{(h)} \in C$ is a label for $\vec{x}^{(h)}$

Model:

$M = \{\vec{\mu}^{(1)}, \ldots, \vec{\mu}^{(c)}\}$ where each $\vec{\mu}^{(i)}$ is a t m-dimensional measurement average s.t.:

$$\vec{\mu}^{(i)} = \frac{1}{Count_{y^{(h)} \in Y}(y^{(h)} = i)} \sum_{y^{(h)} \in Y : y^{(h)} = i} \vec{x}^{(h)}$$

In other words, each $\vec{\mu}^{(i)}$ is the mean vector of all the $\vec{x}^{(h)} \in X$ where the corresponding $y_h = i$, i.e. the signal average of class i.

Feature inclusion parameter:

$r : 0 < r \leq t$ – the number of features that will be used for prediction. This value can be tuned on the training set through cross-validation.

$F =$ top r indices f with the highest value for $\Sigma_{k=1}^{m-1} \Sigma_{l=k+1}^{m} \left| \vec{\mu}_f^{(k)} - \vec{\mu}_f^{(l)} \right|$, where $\vec{\mu}_f^{(i)}$ is the value at the f th index of the signal average of class i

In other words, F is a vector of r dimensions, consisting of the r indices of the $\vec{\mu}$'s where the sum of pair-wise $\boldsymbol{L1}$ distance of the points are the greatest.

Prediction:

$\vec{x}$ – an unseen, sanitized $\boldsymbol{m}$-dimensional sensor measurement.

$$y_{predict} = \arg\min_i \sum_{f \in F} \left| \vec{\mu}_f^{(i)} - \vec{x}_f \right|$$

Equation A.0.1 Simple L1-distance model for classifying sanitized sensor measurements. Description of the classification model formulated that is based on the L1-distance of the per-class average.

Table A.0.3 Classification results for both tasks, using three different machine learning algorithms. Classification Accuracy for SVM, AdaBoost, and L1-distance for the tasks of 1). Distinguishing between the swallow signals of three different boluses: water, yogurt and cracker and 2). Identifying the water swallow signals of a control subject vs. a patient.

Tasks	Prediction Accuracy		
	SVM	AdaBoost	L1-distance
Bolus Classification	0.569	0.717	0.864
Control vs. Patient Discrimination	0.721	0.886	0.947

A.4. References

(1) Barber, C. B.; Dobkin, D. P.; Huhdanpaa, H. The Quickhull Algorithm for Convex Hulls. ACM Trans. Math. Softw. 1996, 22, 469–483.

(2) Savitzky, A.; Golay, M. J. E. Smoothing and Differentiation of Data by Simplified Least Squares Procedures. Anal. Chem. 1964, 36, 1627–1639.

(3) Lloyd, S. P. Least Squares Quantization in PCM. IEEE Trans. Inf. Theory 1982, 28, 129–137.

Appendix B Supporting Information for Chapter 3

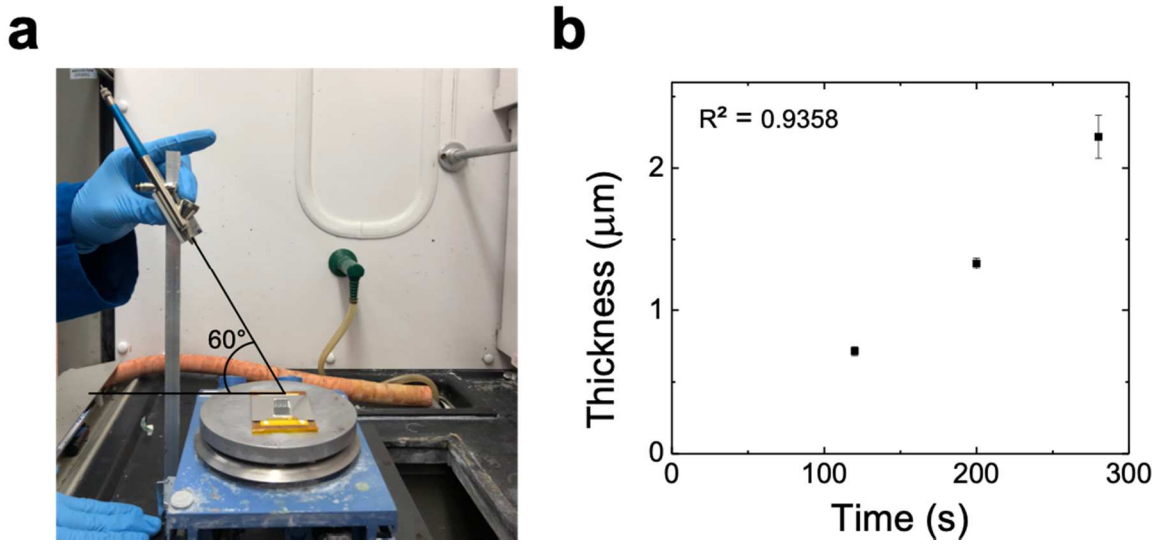

Figure B.0.1. Thickness of PEDOT:PSS formulation layer using spray coating technique. (a) Photograph of the experimental setup of the spray coating of the PEDOT:PSS formulation for the Gr/Pd/PEDOT:PSS structured blend and (b) plot of thickness of the PEDOT:PSS layer as a function of deposition time (duration of primer layer deposition not included) of the PEDOT:PSS formulation with the spray gun.

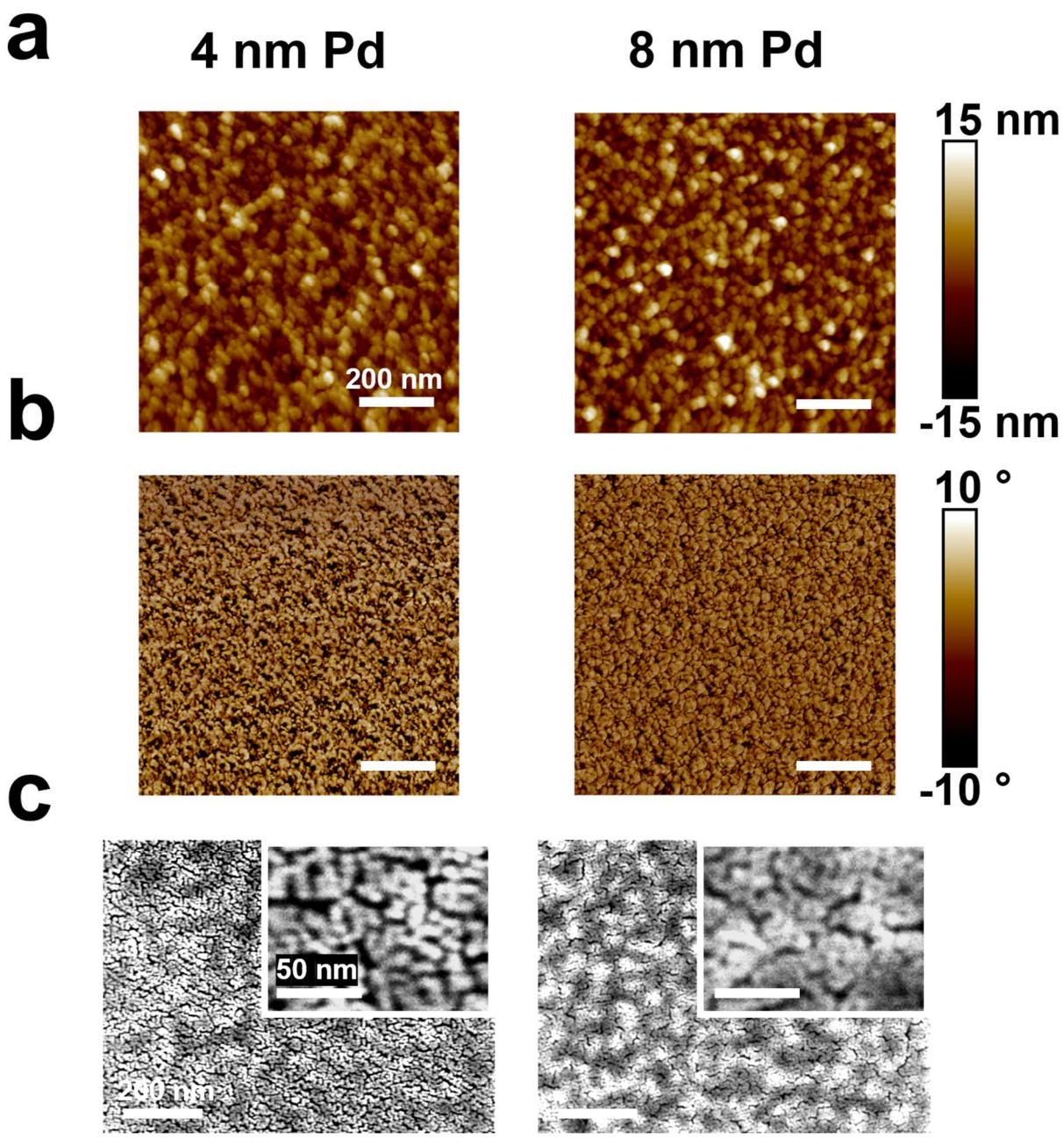

Figure B.0.2. Morphological characterization of palladium films on single-layer graphene. Atomic force microscopy results depicting (a) phase and (b) height images depicting the palladium films of various thicknesses on single-layer graphene. (c) Surface Electron Microscopy (SEM) images of palladium films of various thicknesses on single-layer graphene.

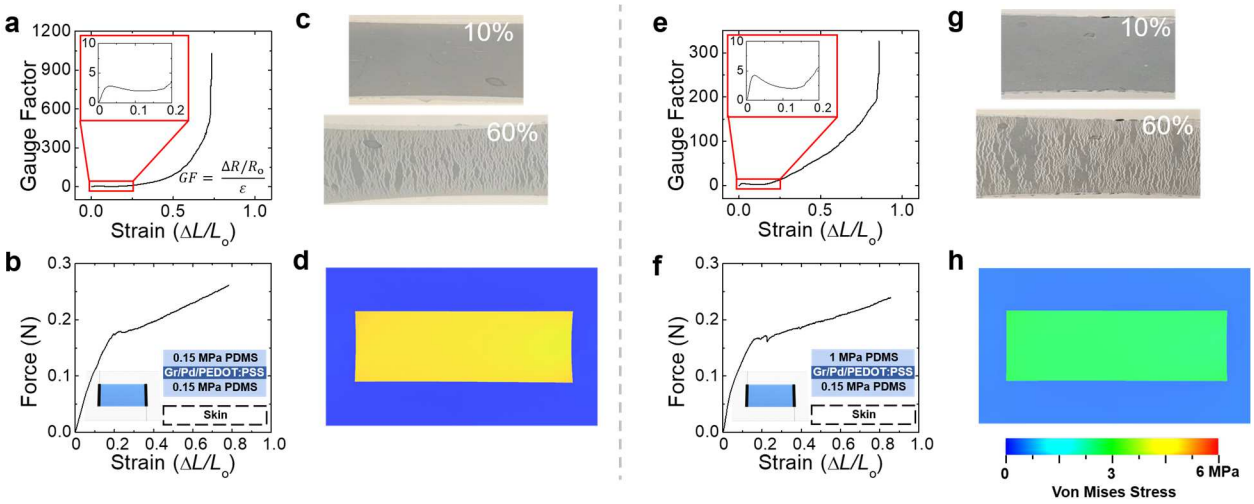

Figure B.0.3. Strain characterization of rectangular Gr/Pd/PEDOT:PSS pattern under uniaxial strain. The gauge factor, mechanical response, photographic images, and finite element analysis (FEA) of the Gr/Pd/PEDOT:PSS structured blend with (a-d) a 0.15 MPa PDMS substrate and a 0.15 Mpa PDMS encapsulant, (e-h) a 0.15 Mpa PDMS substrate and a 1 Mpa PDMS encapsulant.

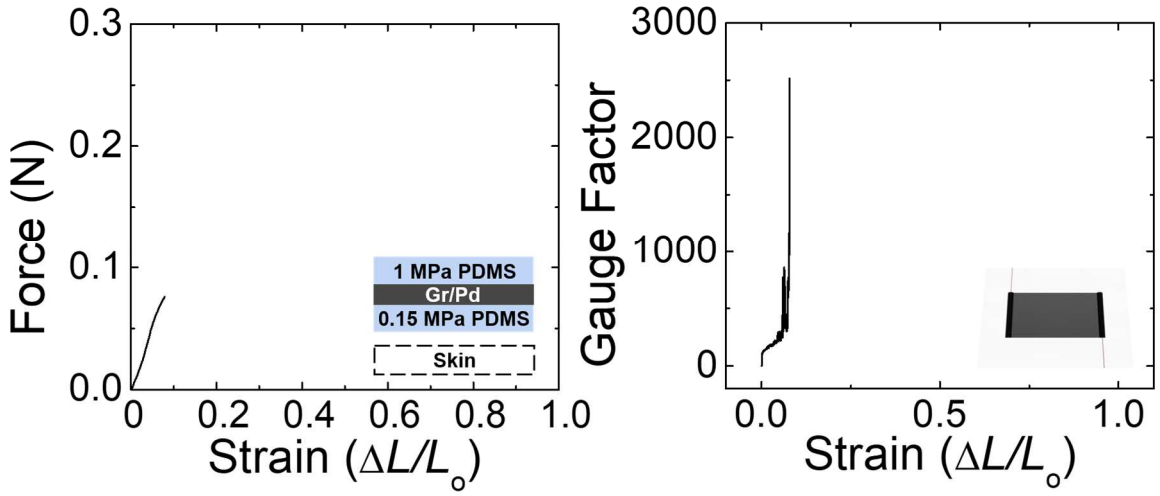

Figure B.0.4. Strain characterization of rectangular Gr/Pd pattern under uniaxial strain. The gauge factor and mechanical response of the Gr/Pd structured blend with a 1 Mpa PDMS encapsulant and a 0.15 Mpa PDMS substrate.

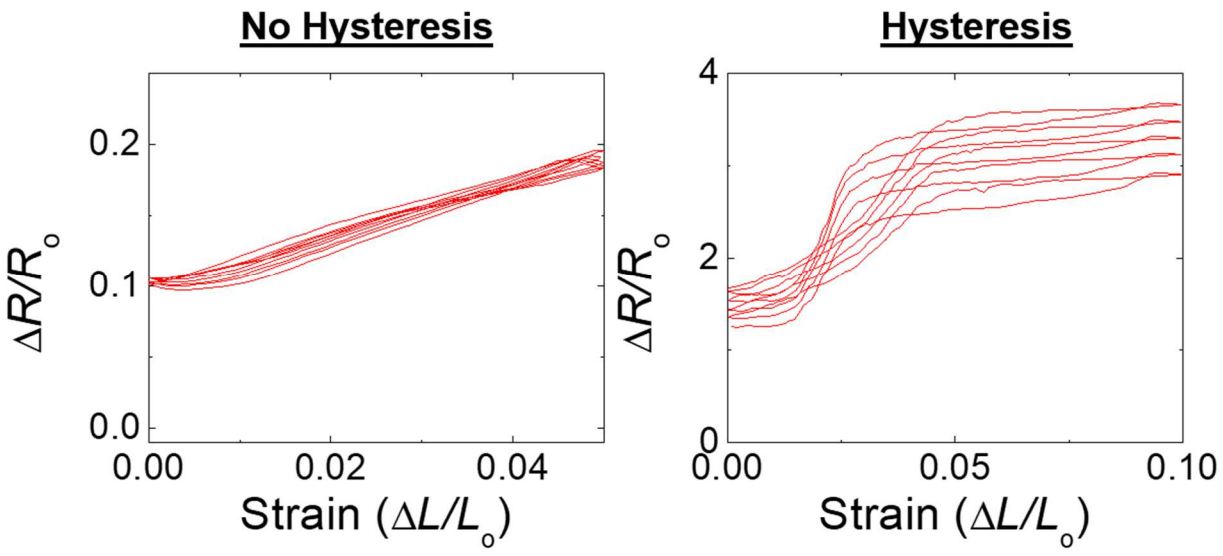

Figure B.0.5. Hysteresis characterization of rectangular Gr/Pd pattern. The piezoresistive response of the Gr/Pd/PEDOT:PSS structured blend with a 1 Mpa PDMS encapsulant and a 0.15 Mpa PDMS substrate under different uniaxial strains.

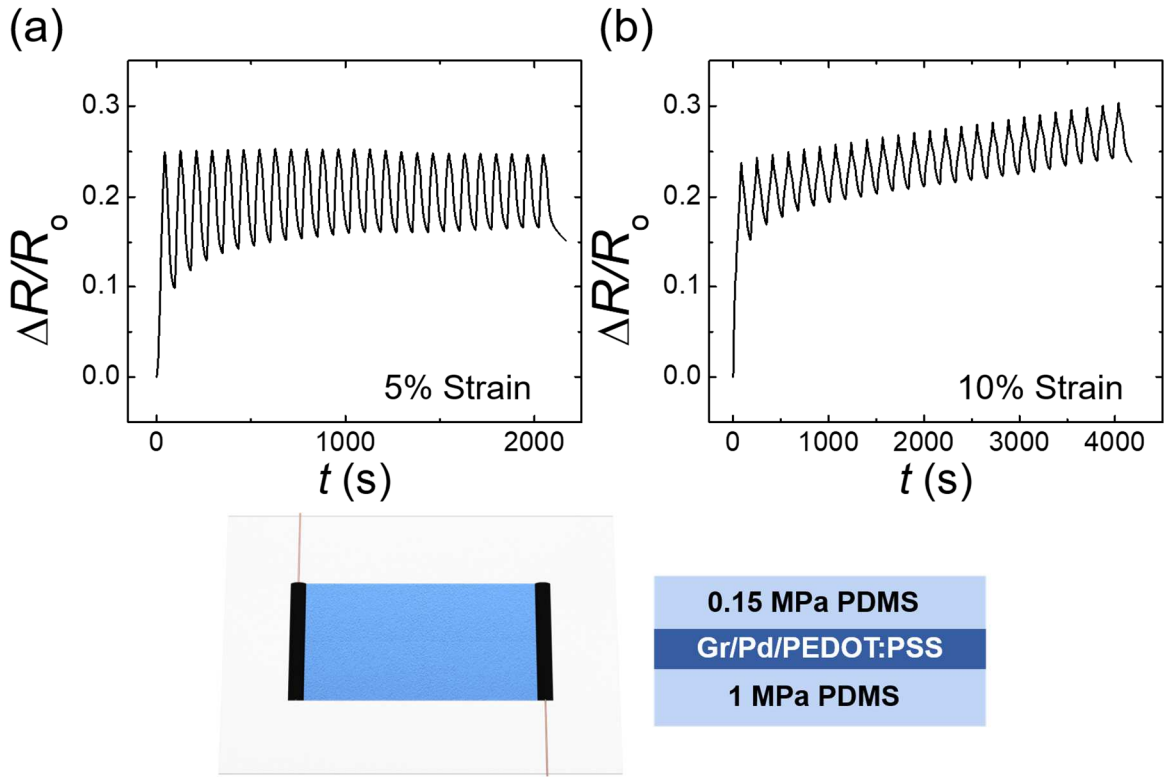

Figure B.0.6. Piezoresistive characterization of the Gr/Pd/PEDOT:PSS device under cyclic strain. Normalized change in resistance of the Gr/Pd/PEDOT:PSS device with a 1 Mpa PDMS substrate under 25 cycles of (a) 5% and (b) 10% strain.

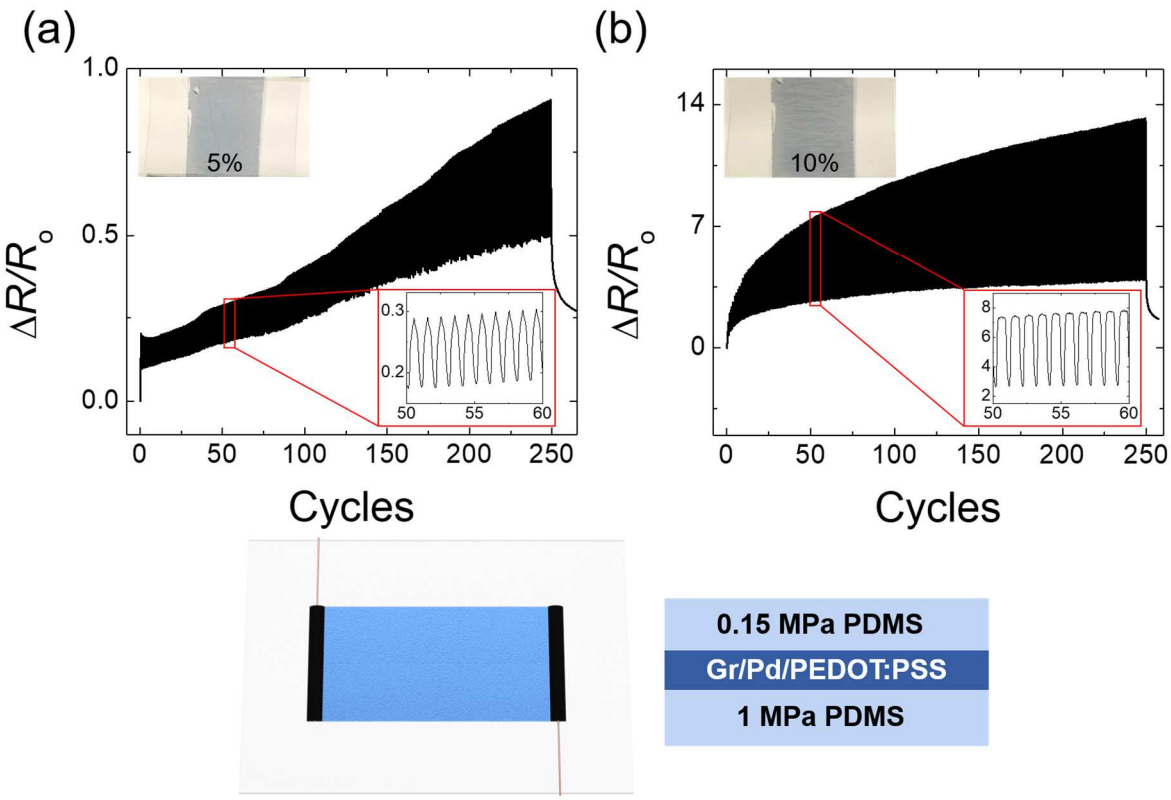

Figure B.0.7. Piezoresistive characterization of the Gr/Pd/PEDOT:PSS device under cyclic strain. Normalized change in resistance of the Gr/Pd/PEDOT:PSS device with 0.15 Mpa PDMS substrate and a 0.15 Mpa PDMS encapsulant under 250 cycles of (a) 5% and (b) 10% strain.

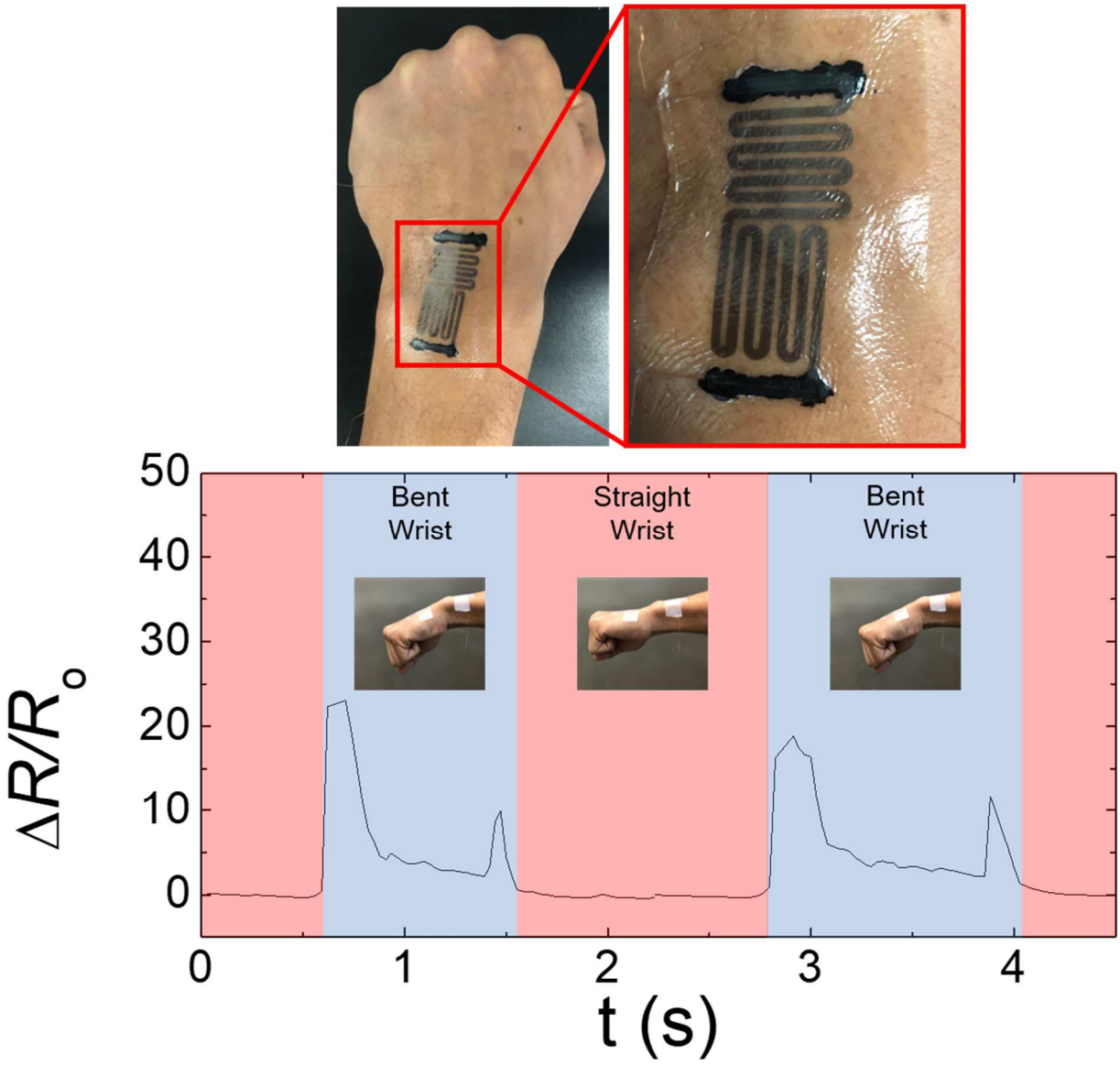

Figure B.0.8. On-body testing of the Gr/Pd/PEDOT:PSS material with a 1 Mpa PDMS encapsulant and a 0.15 Mpa PDMS substrate, patterned into a serpentine strain gauge design. Photograph of the wearable Gr/Pd/PEDOT:PSS sensor with a 1 MPa PDMS encapsulant and a 0.15 MPa PDMS substrate on the wrist of a human subject. Piezoresistive response of the patterned Gr/Pd/PEDOT:PSS sensor to wrist bends.

Table B.0.1. Table comparing the resolution (lowest strain reported), maximum strain, and maximum gauge factor of the Gr/Pd/PEDOT:PSS structured blend to other devices found in the literature.

Citation	Material	Lowest Strain Detection Reported	Max Strain Reported	Max Gauge Factor Reported
This Work	Gr/Pd/PEDOT:PSS	0.001%	86%	1000
4	Single-walled CNTs	0.0125%	0.13%	7
9	Patterned metal Au strain gauge (600 nm thick)	0.5%	40%	1.2
10	Gold film (50 nm thick)	3%	8%	N/A
11	Multi-walled CNTs/epoxy composite	0.01%	1%	14
12	Multi-layered graphene (10 layers)	0.015%	7.1 %	14
13	Graphene platelets	0.08%	0.37 %	325
20	Nanoscale cracked Pt film (20 nm thick)	0.05%	2%	2000
21	Nanoscale cracked Pt film (20 nm thick)	0.5%	2%	16000
22	n-polysilicon MEMS sensor	0.0125	0.35	21
26	Conductive polyester yarns	50%	2000 %	100

Appendix C Supporting Information for Chapter 4

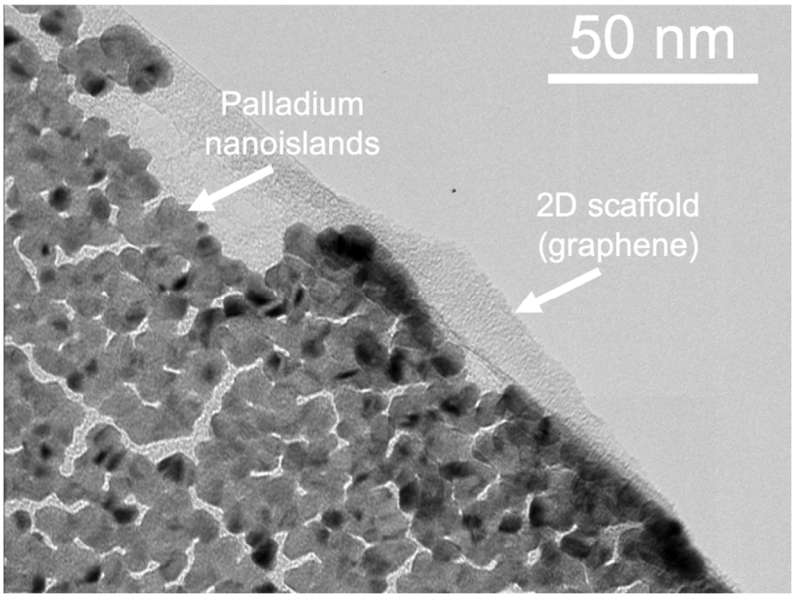

Figure C.0.1 TEM image of Gr/Pd. Transmission electron microscopy (TEM) image of palladium of a nominal thickness of 6 nm on top of single layer graphene.

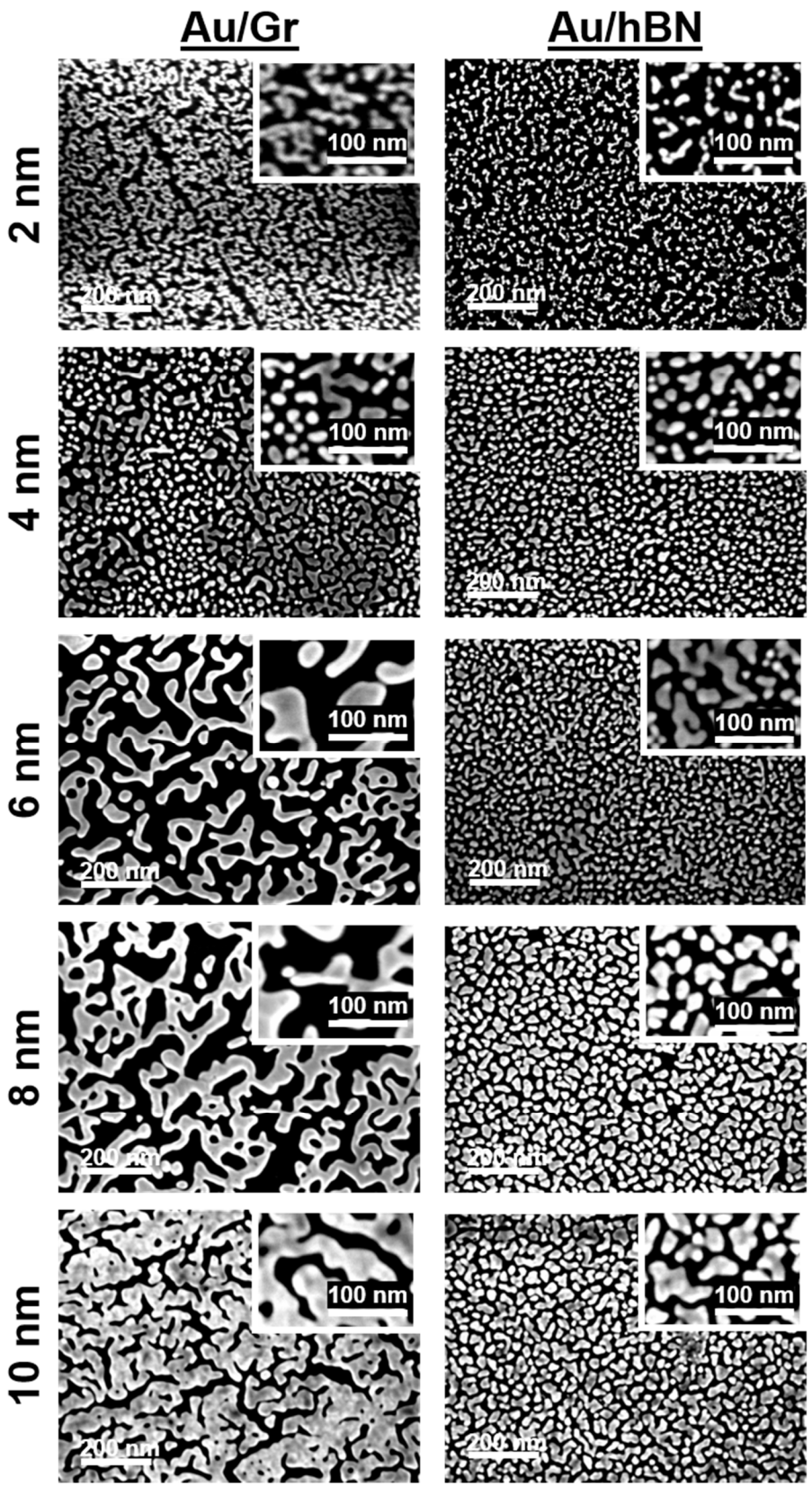

Figure C.0.2 SEM image of 2D/Au. Scanning electron microscopy (SEM) images of different nominal thicknesses of gold supported by either graphene (Gr) or hexagonal boron nitride (hBN).

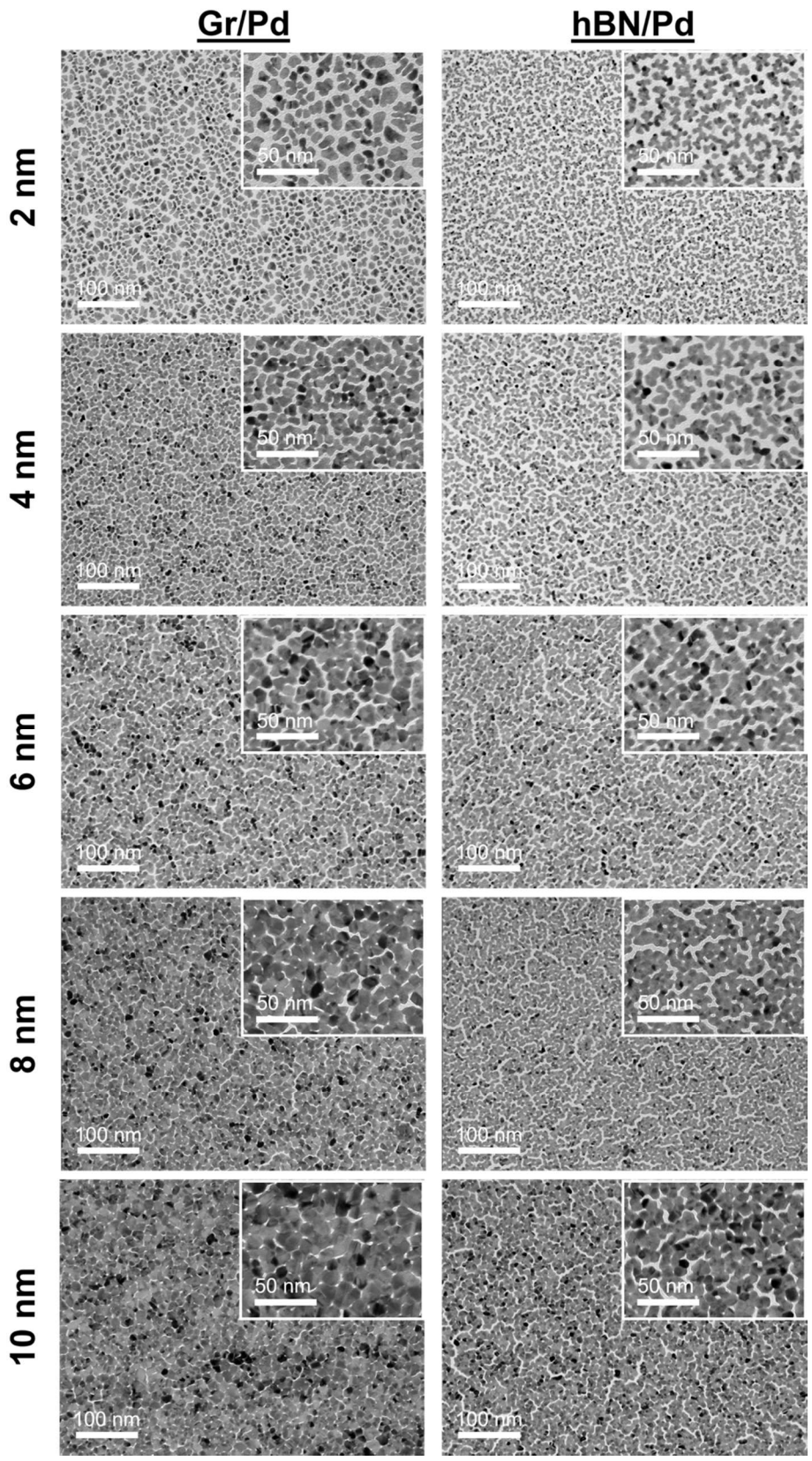

Figure C.0.3 TEM image of 2D/Pd. Transmission electron microscopy (TEM) images of different nominal thicknesses of palladium supported by either graphene (Gr) or hexagonal boron nitride (hBN).

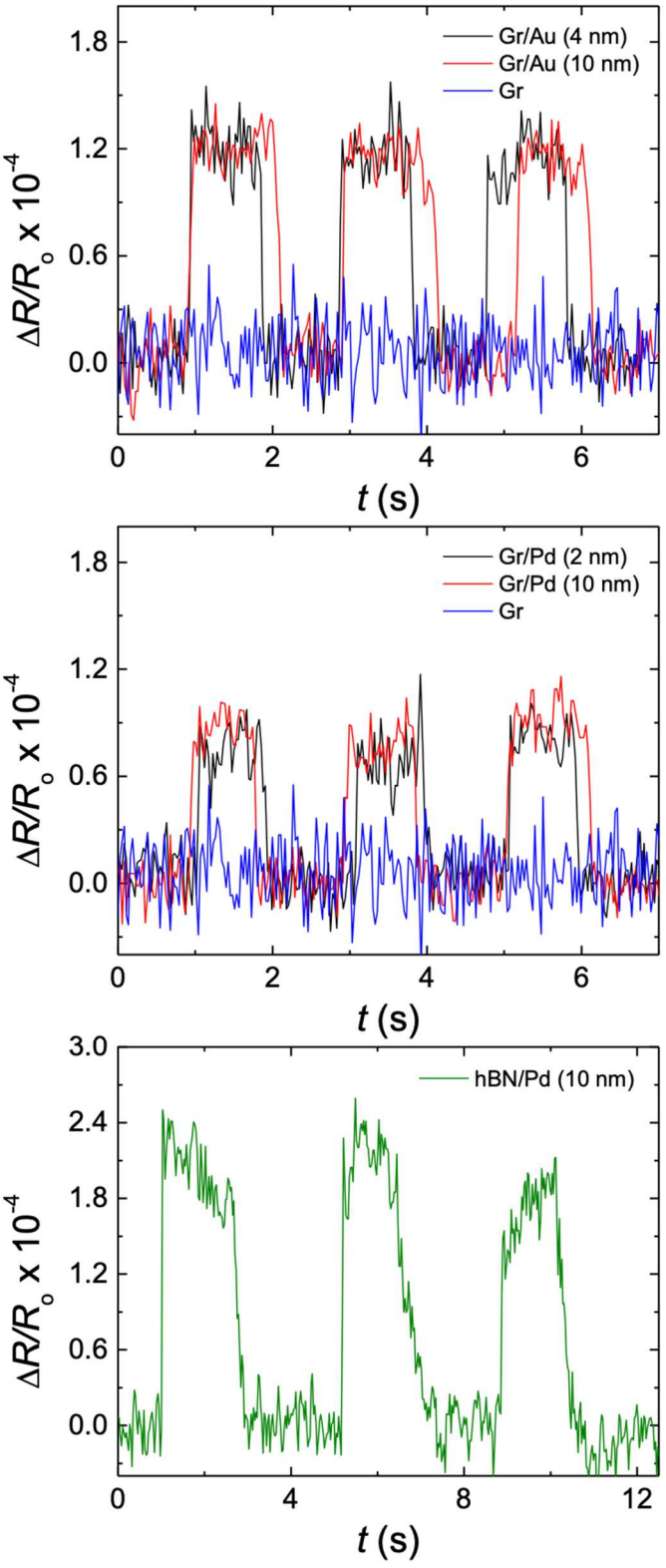

Figure C.0.4 Piezoresistive response of Gr/M and hBN/Pd samples under 1 ppm strain. Plots compare signal to noise of a disconnected metal film on graphene to a percolated subcontiguous film on graphene and hBN.

C.1. Strain-Induced Changes in the 2D Density of States (DOS)

While a thorough exploration of the theoretical origins of the piezoresistance seen in these composite materials is beyond the scope of this work, it is worth briefly discussing the mechanisms we believe are at play, which arise from the mismatch in quantization of energy levels in different regions of the metallic network. The low nominal thicknesses of the metallic films are well within the regime where metals show quantization of energy levels,[1] and, for illustrative purposes, we assume individual nanoislands show behavior reminiscent of thin films. We believe this to be a reasonable assumption given that their lateral dimensions are generally significantly larger than their nominal thicknesses. We can use the prototypic 1D quantum well as a starting point to guide the discussion, for which the spacing between allowed energy levels demonstrates a $1/a^2$ dependence, where a is the width of the well. This model finds its real-world analogue in uniform thin films, where each of these quantized energy levels (confined along the z-direction) correspond to a subband edge, which (if the electrons population near the subband edge can be approximated as a Fermi gas) displays parabolic dispersion along the in-plane (x- and y-) directions. Correspondingly, this results in a DOS(E) which is a sum of step functions, where each step occurs at the energy pertaining to the next quantized energy level.[2,3] It may start becoming clear how, in a percolated network primarily composed of thin-film-like regions of variable thickness, there are many scattering opportunities as the charge is transferred from one region to the next.

Consider two thin, semi-infinite films which are of different thicknesses and lie in the same plane, such that they share an edge where charge is transferred between the two films as it propagates along the plane (in contrast to transverse to it, as is usually considered in typical

heterostructures). The steps in the DOS(E) are shifted to higher energies for the thinner film than the thicker one. If charge is to transfer from the thicker region to the thinner one, there will be some energy ranges where there are more occupied states in the thicker region than are available in the thinner one. This will be true even if we ignore the occupancy of states in the thinner region, because the steps in the DOS(E) are shifted to higher energies in the thinner region as compared to the thicker one. So, if electron energies are conserved, this will result in backscattering at the interface, as there is a fundamental deficiency of available states to accommodate those incoming electrons. This pertains to the real systems at hand in that, under some applied tensile strain, it can be reasonably expected that stress is concentrated in the thinner regions of the percolated network, further decreasing their critical dimension and forcing the subband edges to higher energies, exacerbating the effect described above and further frustrating charge transfer from adjacent thicker regions. The reasoning here bears resemblance to the theory of quantized conductance, developed by Landauer *et al*.[4–6] According to this theory, discrete conductance channels originate from the subbands of 1D conductors, and discrete steps in the conductance correspond to the populating of these subbands. We suggest analogous channels are at play in our percolated networks, where access to these channels is regulated by an applied strain instead of applied bias.

We have arrived at this description from an extremely simple thought experiment which only considers the variations in the DOS(E) of dissimilar thin films.Considering added complications such as additional conserved quantities (e.g. k-vector components), the necked regions between nano-islands (which will behave more like 1D conductors than thin-films), increased surface area/scattering centers, etc. only adds additional mechanisms by which scattering would be promoted as tensile stress is applied. Thus, we postulate the decrease of the

critical dimensions of dissimilar regions in the percolated network under an applied tensile stress as a likely mechanism driving the overall increase in electrical resistance of our systems.

C.2. References

(1) Chiang, T. C. Quantum Physics of Thin Metal Films. *AAPPS Bull.* **2008**, *18* (2).

(2) Kittel, C. *Introduction to Solid State Physics, 8th Edition*, 8th ed.; Wiley & Sons, New York, NY, 2004.

(3) Hook, J. R.; Hall, H. E. *Solid State Physics, 2nd Edition*, 2nd ed.; Wiley & Sons, New York, NY, 1995.

(4) Landauer, R. Spatial Variation of Currents and Fields Due to Localized Scatterers in Metallic Conduction. *IBM J. Res. Dev.* **1957**, *1* (3), 223–231.

(5) Wharam, D. A.; Thornton, T. J.; Newbury, R.; Pepper, M.; Ahmed, H.; Frost, J. E. F.; Hasko, D. G.; Peacock, D. C.; Ritchie, D. A.; Jones, G. A. C. One-Dimensional Transport and the Quantisation of the Ballistic Resistance. *J. Phys. C Solid State Phys.* **1988**.

(6) Van Wees, B. J.; Van Houten, H.; Beenakker, C. W. J.; Williamson, J. G.; Kouwenhoven, L. P.; Van Der Marel, D.; Foxon, C. T. Quantized Conductance of Point Contacts in a Two-Dimensional Electron Gas. *Phys. Rev. Lett.* **1988**, *60* (9), 848–850.